

https://dspace.org/

Magnetic characterization study of gadolinium chelate modified multi-walled carbon nanotubes, graphene oxide and reduced graphene oxide: a comparative study

Mosse, Ibwanga Saverios

2020

https://hdl.handle.net/10539/31053

Downloaded from a DSpace repository. https://dspace.org/



Magnetic Characterization Study of Gadolinium Chelate modified Multi-Walled Carbon nanotubes, Graphene oxide and Reduced Graphene Oxide: A Comparative Study

Ibwanga Saverios Mosse

July 2020

Thesis submitted to the Faculty of Science, University of the Witwatersrand, Johannesburg, in fulfilment of the academic requirements for the

Degree of Doctor in Philosophy

Declaration

The measurements reported in this thesis were carried out at the University of the Witwatersrand, Johannesburg, South Africa.

The data analysis and understanding of results is my own work and was carried under the guidance of Professor Somnath Bhattacharyya.

The work of other scientists is duly acknowledged when used in this thesis.

This thesis has not been submitted before for any degree or examination at any other University.



Ibwanga Saverios Mosse

July 2020

Abstract

The carbon nanotubes are characterized by interesting physical properties, which resulting from the strong carbon – carbon covalent sp^2 bond. Their properties derived from the 1D structure. The surface modification of carbon nanotubes can stretched their application in many sectors. However, the functionalization of carbon nanotubes involving oxidative reflux is known, and popularly used for the introduction of chemical functionality along the surface and ends of carbon nanotubes. The volatile method invariably results in an unpredictable degree of chemical functionalization of carbon nanotube surfaces, variable lattice order, and potentially introduces chemically different nanoscale environments.

This study focuses on a predictable approach towards the functionalization of multi-walled carbon nanotubes (MWCNTs); aimed at manipulating the degree and chemical nature of functionalization by controlling oxidative reaction temperatures, with a view to incorporate a magnetic complex on the nanotube surface via ternary complex formation. Our findings indicate functionalization occurs at temperatures as low as 55 °C. However, the chemical nature of the attached functional groups varies with increasing temperature – understanding the latter is essential for the attachment of metal complexes to carbon nanotubes. Investigation of the functionalized MWCNTs using spectroscopic techniques elucidates the prevailing chemical nature of the nanotube surface that suggests carboxylate functionality, is replaced at higher temperatures, by the formation of hydroxyl moieties. This observation is substantiated through deconvolution of D and G phonon modes of recorded Raman spectra, corroborated by Zeta potential studies and analysis of acid-base titration data. Attachment of the Gadolinium complex of dietheylenetriaminepentaaccetic acid, [$GdDTPAH_2$], to a functionalized-MWCNT is confirmed by chemical analysis using Inductively Coupled Plasma Atomic Emission Spectroscopy (ICP-OES), which shows the percentage of gadolinium varying in the range of 5 % to 6 % in the samples. The acquisition of magnetic data reveals the antiferromagnetic interaction and possibly an anisotropic exchange bias. The magnetic properties show a distinct temperature dependence, this includes a

change in slope of the saturation moment, which increases to a point of non-saturation as the temperature decreases. This is an indication that there is a competing magnetic phase different to the ferromagnetism. It is also revealed that high surface modification of multi-walled carbon nanotubes using Gd-DTPA, increases excitation level of gadolinium electron in the material.

In addition, Carbonyl group have been introduced onto graphene single layer surface via Modified Hummers method. Sodium nitrate and potassium permanganate used as oxidant reactants. L-ascorbic acid used to produce reduced graphene oxide. Lower concentration of carboxylic group on reduced graphene oxide influenced the magnetic and electronic properties of the sample. Magnetic environment affect electronic transport properties of the reduced and graphene oxide. The magnetic data indicates paramagnetic behavior with impurities showing slight slope in the range of zero field. Consequently, it is also displayed the surface modification of graphene oxide and reduced graphene oxide using magnetic molecule Gd-DTPA accompanied with increases excitation of gadolinium electron in their orbital. Those complexes can be used to increase or decrease the relaxation times of carbon-13 nuclei in NMR spectrometry.

Acknowledgements

I am the highest graduate person in my family. Considering my background, it would have been impossible for me achieving this success without the support of the following people.

First and foremost, I would like to express my deepest gratitude to Prof. Dr. Somnath Bhattacharyya for giving me the opportunity to pursue PhD under his guidance. I am indebted for the rest of my life to him. I can't express my joyfulness when Prof. Somnath first accepted me as a doctoral candidate and gave me access the best nanoscale transport in the whole continent of Africa. He gave the students the complete freedom of exploring the new ideas and was quickly helpful in getting my sample characterization done. Under his supervision, I was able to learn problem solving through both scientific and philosophical approaches. His continuous support both technical and financial has made my PhD studies successful.

I would like to thank Prof. Dr. Alvaro de Sousa for his continuous support in planning the CNT functionalization and Gd loading experiments and monitoring my progress for time to time. Dr. Christopher Coleman was instrumental in analyzing all my sample data and correlating it with science. His knowledge in condensed matter physics is immeasurable and I am very much thankful to him for thoughtful provoking critics. Dr. Siphe Ncube helped with instrumental set-up. Venkateswara Rao Sodisetti in helping me with some Raman peak fitting. Thanks to you.

There are many well versed scientists who helped me in characterizing my samples on an immediate request for this project that I would like to express my gratitude. Dr. Rudolph Erasmus for Raman Spectroscopy characterization, Dr. Emmanuel Flahaut for HRTEM and SQUID magnetometry measurements, TOF-SIMS was done by TESCAN ORSAY Holding, a.s, again this was made possible by Prof. Somnath Bhattacharyya, Prof. Daniel Wamwangi for magnetic measurements at low temperatures.

I am grateful to Professor Naidoo Deena (Head School) and Professor Jonathan Kearthland for their administrative assistance during this project and also to Faculty of Science, Wits university. I am thankful to Postgraduate Merit Award committee of Wits University for assisting me with tuition fee financial support. Finally. I am thankful to my parents, my wife Bopita and my children Daniel, Believe, Grace and Alice Mosse.

Table of contents

Declaration.....**i**

Abstract.....**ii**

Acknowledgements.....**iv**

Table of contents.....**v**

List of figures.....**ix**

List of Table.....**xvi**

Abbreviations.....**xvii**

Chapter 1

Introduction.....**1**

1.0. Background on carbon nanotubes.....3

1.1. Carbon and its allotropes.....5

1.2. Properties of carbon nanotubes.....9

1.3. Synthesis method of CNTs.....10

1.4. Different method of functionalization.....12

1.5. Chelate system form with functionalized MWCNTs.....14

1.6. Graphene and Method of synthesis.....15

1.7. Chemical modification of graphene.....16

1.8. Aims and objectives.....17

1.9. Thesis outline.....18

Chapter 2

Literature review.....**19**

2.1. Background of spintronics.....19

2.1.1. Giant magneto-resistance effect.....20

2.1.2. Magnetic Tunnel Junction effect 21
2.1.3. Spintronic Devices, carbon nanotube and graphene in spintronic 24
2.2. Multi-walled carbon nanotubes and graphene. 27
2.3. Magnetic susceptibility and type of magnetism.....29
2.4. Gadolinium and Diethylene Triamine Pentaacetic Acid 36
2.4.1. Gadolinium 36
2.4.2. Diethylene Triamine Pentaacetic Acid 36
2.5. Fabrication techniques of devices 37
2.5.1. Di-electrophoresis 38
2.5.2. Electron Beam Lithography 40

Chapter 3

Experimental Section 43
3.1. Equipment 43
3.2. Chemical Synthesis of materials under-study 44
3.2.1. Gd-DTPA chelate complex 44
Reagents and materials 44
Preparation of the Gadolinium chelates 45
3.2.2. Functionalization of MWCNTs 46
Drying of f-MWCNTs 46
Purification of f-MWCNTs 48
3.2.3. Linkage of magnetic complex onto f-MWCNTs 49
3.2.4. Synthesis of graphene oxide 51
3.2.5. Linkage of Metal complex onto Graphene oxide 51
3.2.6. Synthesis of Reduced graphene oxide and Gd-DTPA loading onto rGO.....52
3.3. Characterization techniques 53
3.3.1. Scanning Electron Microscopy 53

3.3.2. TESCAN microscope....54
3.3.3. Fourier Transform Infra-Red spectrometer....56
3.3.4. Raman Spectroscopy....57
3.3.5. Zeta potential....58
3.4. Device fabrication....58
3.4.1 Di-Electrophoresis....59
3.4.2. Semiconductor device testing Machine....60
3.4.3. Cryogenic high field measurement system....61

Chapter 4

Results and Discussions on the Multi-walled Carbon nanotubes....63

4.1. Functionalized Multi-walled Carbon Nanotubes....63
4.1.1. FT-IR spectroscopy....63
4.1.2. Raman spectroscopy....65
4.1.3. Zeta Potential Analysis of f-MWCNTs....78
4.1.4. Titration of functionalized Multi-walled carbon nanotubes....79
4.1.5. Scanning Electron Microscopy....82
4.1.6. I-V Characteristic of f-MWCNTs....83
4.2. Gadolinium-DTPA loaded onto surface of f-MWCNTs....85
4.2.1. FT-IR spectroscopy....85
4.2.2. TOF-SIM spectrometry....86
4.2.3. Raman spectroscopy....90
4.2.4. Inductively Coupled Plasma-Optical Emission Spectrometry....99
4.2.5. High Resolution Transmission Electron Microscopy....101
4.2.6. Magnetization characteristics of Gd functionalized CNTs....104

Chapter 5

Graphene oxide and reduce graphene oxide 112

5.1. Graphene oxide 112

5.1.1. FT-IR spectroscopy 112

5.1.2. Titration of Graphene Oxide 114

5.2. Gd-DTPA loaded onto surface of Graphene oxide 115

5.2.1. FT-IR spectroscopy 115

5.2.2. Raman spectroscopy 117

5.3. Reduced Graphene oxide 120

5.3.1. FT-IR and UV-visible spectroscopy 120

5.3.2. Acid-Base Titration of Reduced Graphene Oxide 122

5.4. Gd-DTPA loaded into surface of Reduced Graphene Oxide 123

5.4.1. FT-IR spectroscopy 123

5.4.2. Raman spectroscopy 125

5.5. Magnetic measurement of GO-Gd-DTPA and rGO-Gd-DTPA 128

Chapter 6

Conclusion and Recommendations 130

References 134

Appendix 146

Publications 157

List of figures

Figure 1. 1: Crystal structure of certain allotropes of carbon: Carbon nanotubes (a), Fullerene (b), graphite, (c), graphene (d), Diamond (e).....7
Figure 1. 2: (a) Two dimensional hexagonal lattice, (b) Different types of CNTs. 8
Figure 1. 3: (a) The MWCNTs that resulted from the first growths using the arc discharge method. (b) The first SWNTs from the arc discharge growth method by Iijima et al.. (c) The SWNTs from the arc discharge growth by Bethune et al.....11
Figure 1. 4: (a) Schematic diagram of the CVD oven in the Hone lab as well as two digital pictures of the setup. (b) The results of SWNTs coming from patterned catalyst islands that were grown by the CVD method 12
Figure 1. 5: Schematic diagram of different chemical method of surface functionalization of MCNT.....13
Figure 1. 6: Typical example of DTPA linked with functionalized carbon nanotubes.....14
Figure 1. 7: Illustration of preparation of graphene oxide GO from graphite material.....16

Figure 2. 1: Schematic representation of the GMR effect showing the resistance of the multilayers against the field (a), magnetization shapes (b), and plotting of magnetization as function of field (c). 21
Figure 2. 2: schematic diagram of tunneling magnetoresistance effect. 23
Figure 2. 3: Configuration of magnetic tunnel junction device TMR (a) and giant magneto-resistance GMR (b). Indication of spin of electron direction relates the resistance of the spintronic device. 24
Figure 2. 4: SEM micrograph of the sample (a), device configuration (b), spin-valve feature of the device (c), and trace measurements recorded at 20 $mT.s^{-1}$.....26
Figure 2. 5: (a) schematic diagram of the single molecule magnet, (b) attachment of single molecule magnet on the graphene sheet, (c) architecture of device with source and drain electrodes and, (d) SEM micrograph of the device. 27
Figure 2. 6: (a). I-V_{SD} curve measured for SWCNTs device at gate voltage range from –6V to 6V (b) I-V_G curve measured for MWCNTs device.....28
Figure 2. 7: Schematic diagram of materials in the presence and absence of applied magnetic Field.....30

Figure 2. 8: Illutration of resulting susceptibility curves plotted as function of temperature. 32
Figure 2. 9: Illustration of the blocked states (left) and superparamagnetic state.....34
Figure 2. 10: Chemical structure of Diethylene Triamine Pentaacetic acid DTPA molecule. 37
Figure 2. 11: (a) Non-suspended carbon nanotubes device, (b) Associated spectrum of Intensity (I) against voltage. 38
Figure 2. 12: Schematic diagram showing the electrodes and associated spectrum as appears on the oscilloscope.....38
Figure 2. 13: (a) Magnified image of the pattern and (b) overview of the operation mode showing a drop of isopropanol dispersed carbon nanotubes aligned on the electrode.40
Figure 2. 14: Different steps achieved for a device fabrication by ebeam Lithography. 41
Figure 2. 15: Two typical example of the device fabricated by ebeam suspended nanotubes (left) and associated with conductance vs back gate voltage (right). 42
Figure 2. 16: Deposition vacuum chamber as set setup at the Nano-scale transport laboratory. School of Physics, Wits University. 42

Figure 3. 1: chemical structure of diethylenetriamine pentaacetic acid gadolinium (lll) dihydrogen salt hydrate. 46
Figure 3. 2: Schematic diagram of functionalization process of multi-walled carbon nanotube at different temperatures using mixture of nitric and sulfuric acid. 48
Figure 3. 3: Set-up of the Purification of the samples in the fume hood, showing Schlenk line.....49
Figure 3. 4: Schematic diagram of the loading of Gd-DTPA onto of the f-MWCNTs. 50
Figure 3. 5: Schematic diagram of the loading of magnetic molecular Gd-DTPA onto surface of the graphene oxide (GO). 52
Figure 3. 6: SEM machine connected with electron beam lithography at the NSTP Laboratory, Wits University. 54
Figure 3. 7: Schematic diagram of TOF-SIMS instrument. 55
Figure 3. 8: LYRA3 FIB SEM associated with TOF-SIMS compartment 56
Figure 3. 9: Bruker Tensor 27 FT-IR spectrometer used in this project. 57
Figure 3. 10: Photograph of Zeta potential analyzer (Zeta sizer Nano series model) used.58
Figure 3. 11: Di-electrophoresis station at NSTP Laboratory, Wits University. 59

Figure 3. 12: Janis micro manipulated semiconductor analyzer testing machine. 60

Figure 4. 1: FT-IR spectra of pristine and functionalized multi-walled carbon nanotubes at different temperature and reaction time. 65

Figure 4. 2: Raman patterns of pristine multi-walled carbon nanotubes in comparison of f-MWCNTs taken at from 900-3200 cm^{-1}. The spectral patterns displayed two broad features in first order 1000 – 2000 cm^{-1}. And asymmetric feature in the second order spectra (2000 – 3400 cm^{-1}) 67

Figure 4. 3: Deconvolution model applied on Raman spectrum of pristine. First order shown between the values of 845 cm^{-1} - 1900 cm^{-1} and second order in the range of 2000 to 3300 cm^{-1}. 69

Figure 4. 4: Curve fitting of f-MWCNT(55) material. Showing two main region of the Raman spectrum. First order shown between the values of 845 cm^{-1} - 1900 cm^{-1} and second order in the range of 2000 to 3300 cm^{-1}.....70

Figure 4. 5: Curve fitting of f-MWCNT(60) material. Showing two main region of the Raman spectrum. First order shown between the values of 845 cm^{-1} - 1900 cm^{-1} and second order in the range of 2000 to 3300 cm^{-1}.....72

Figure 4. 6: Curve fitting of f-MWCNT(70) material. Showing two main region of the Raman spectrum. First order shown between the values of 845 cm^{-1} - 1900 cm^{-1} and second order in the range of 2000 to 3300 cm^{-1}.....73

Figure 4. 7: Curve fitting of f-MWCNT(100) material. Showing two main region of the Raman spectrum. First order shown between the values of 845 cm^{-1} - 1900 cm^{-1} and second order in the range of 2000 to 3300 cm^{-1}.....74

Figure 4. 8: Intensity ratio I_D/I_G as Function of reaction temperature. This was taken before chemical reaction (Pristine) and after chemical functionalization of the material under study revealed by the Raman spectroscopy. 75

Figure 4. 9: Histogram plotted of intensity of D, 2D, G band as function of reaction temperature. f-MWCNTs are compared in term of the intensity trend of D, 2D, G bands. The strong change in the *D* and *G* bands is responsible of the chemical functionalization of the carbon nanotubes. 76

Figure 4. 10: Plot of the chemical functionalization degree (CFD) obtained by Raman spectroscopy [Raman CFD = Sum [rel. area (S, Dl, Dr, Gv, Gl, Gr)] / Sum [rel. area

(D, Gl) x 100, in comparison with the functionalization degree determined by acid-base titration. 77
Figure 4. 11: Histogram gives percentage of intensity of the D, G, 2G and S bands in first and second order. The model provided a quantification of the band broadening which shows that *D* band has been typically associated with disorder on the graphitic material. 78
Figure 4. 12: Histogram of the concentration of mmol COOH/mg f-MWCNTs as function of Temperature. 81
Figure 4. 13: Morphologies of the pristine CNTs and functionalized multi-walled carbon nanotubes 55 °C and 60 °C taken at same magnification. 83
Figure 4. 14: (a) I-V measurement of Pristine and f-MWCNTs. (b) Average Relative Resistance as function of reaction temperature. 84
Figure 4. 15: FTIR spectra of pristine and Gd-DTPA loaded into functionalized multi-walled carbon nanotubes. 86
Figure 4. 16: Showing morphologies images taken on the surface of Gd-DTPA-f-MWCNTs materials. The focused Ion bean scanning electron images (a). Distribution map of Gadolinium ion $^{158}Ga^{+}$ (b). This result show that the change in the morphology can be affected by reaction temperature of during the covalent functionalization of the multi-walled carbon nanotubes. 87
Figure 4. 17: Showing a positive secondary ion mass spectra of Gd-DTPA-f-MWCNTs materials in high mass range. Indicating the presence of fragmentation pattern of gadolinium isotopes and $(^{158}Gd^{16}O)^{+}$ ion in the material under study. 89
Figure 4. 18: Comparison of light and black area Raman spectra of magnetic molecular Gd-DTPA chemically reacted with functionalized multi-walled carbon nanotube in the period of 24 hours. The intense peak between 1000 cm^{-1} and 2000 cm^{-1} attributed in *D* and *G* bands. 90
Figure 4. 19: Deconvolution of Raman spectra of Gd-DTPA-f-MWCNT(55) using a 514 nm excitation laser. It was taken in the range from 800 cm^{-1} to 1900 cm^{-1} of the Raman spectrum. 91
Figure 4. 20: Comparison of light and black area Raman spectra of magnetic molecular Gd-DTPA chemically reacted with f-MWCNT(60) in the period of 24 hours. The intense peak between 1000 cm^{-1} and 2000 cm^{-1} attributed in *D* and *G* bands. 93

Figure 4. 21: Deconvolution of Raman spectra of Gd-DTPA-f-MWCNT(60) using a 514 nm excitation laser. It was taken in the range from 800 cm^{-1} to 1900 cm^{-1} of the Raman spectrum.....94
Figure 4. 22: Comparison of light and black area Raman spectra of magnetic molecular Gd-DTPA chemically reacted with f-MWCNT(70) in the period of 24 hours. The intense peak between 1000 cm^{-1} and 2000 cm^{-1} attributed in *D* and *G* bands. Range between 2000 cm^{-1} to 3300 cm^{-1} assigned to 2D band. 95
Figure 4. 23: Deconvolution of Raman spectra of Gd-DTPA-f-MWCNT(70) using a 514 nm excitation laser. It was taken in the range from 800 cm^{-1} to 1900 cm^{-1} of the Raman spectrum.....96
Figure 4. 24: Curve-fitting Raman spectra of Gd-DTPA-f-MWCNT(55) using a 514 nm excitation laser. Less significant change observed in the intensity ratio of *D* and *G* bands. Deconvolution was taken in the range from 800 cm^{-1} to 1900 cm^{-1} of the Raman spectrum.....97
Figure 4. 25: Comparison of light and black area Raman spectra of magnetic molecular Gd-DTPA chemically reacted with f-MWCNT(100) in the period of 24 hours. The intense peak between 1000 cm^{-1} and 2000 cm^{-1} attributed in *D* and *G* bands. Range between 2000 cm^{-1} to 3300 cm^{-1} assigned to 2D band. 99
Figure 4. 26: Plotted of Dependence of temperature as function of gadolinium percentage and Carboxylic group per f-MWCNTs against gadolinium percentage. 101
Figure 4. 27: Morphologies images from High-Resolution Transmission electron microscopy of pristine and Gadolinium-DTPA loaded onto multi-walled carbon nanotubes. 103
Figure 4. 28: Illustrates Hysteretic behavior of the samples show signatures of a mixed magnetic phase with competition between ferromagnetism and antiferromagnetic ordering. This is evident from the clear hysteresis (ferromagnetic part), as well as the non-saturation as temperature is reduced (evidence for antiferromagnetic).....105
Figure 4. 29: Demonstration of the coersive field of the Gd-functionalized multi walled nanotubes shows a temperature dependence, where it increases as temperature decreases until reaching low temperatures where the magnetic moment diverges after which H_c decreases. A further observation is the slight asymmetry in the cohersive field, an indication of exchange bias, thus further supporting the mixed or competing magnetic nature of this material.....106

Figure 4. 30: FC and ZFC susceptibility plot of Gd-DTPA-f-MWCNTs showing the temperature dependence of the magnetic moment, the lack of blocking temperature rule out superparamagnetism. The inset shows a plot of the temperature dependence of the inverse susceptibility, the Curie-Weiss law fitted to linear region yields a negative curie-Weiss temperature indicating the presence of antiferromagnetic interaction. 107
Figure 4. 31: Plot of the first derivative of the magnetic moment as a function of applied field. This plotting procedure allow for the disentanglement of the mixed phase contribution to the magnetic properties, there are two pronounced features as would be expected for a mixed system, this is evident by the sharp central peak at zero field and then the two broader peaks at finite values of applied field. The central peak is diminished as temperature decreases, indicated suppression of the misaligned anti-ferromagnetic character and growth of the ferromagnetic domains. 108
Figure 4. 32: Comparison of magnetic hysteresis for the samples synthesized at various temperature range. The intrinsic diamagnetic response of the nanotubes is reduced with increasing temperature, indicating disruption of the conduction pi-electron network as more Gd-DTPA is attached to the nanotubes. The inset shows the temperature dependence of the slope of the large field part, the increase in slope indicate the samples move away from diamagnetic to a more ferromagnetic system with increasing temperature. 110
Figure 4. 33: Magnetic hysteresis across the samples synthesized at various reaction temperatures indicates that as the reaction temperature increases, the system moves away from a diamagnetic character typical for intrinsic nanotubes. This is evident by the slope, also we see that the low field region has a pronounced variation in the cohersive field. 110
Figure 4. 34: Variation between cohersive field and reaction temperature. As reaction temperature increases the distribution of the Gd-DTPA ligands increases and leads to a disruption of the ferromagnetic character, this trend reaches a minimum for the 70 C sample, upon reactions at higher temperatures the hysteresis increases significantly indicating perhaps that additional loading results on the presence of hydroxyl group, also in large coupling between spin centres, resulting in large ferro magnetic response.....111

Figure 5. 1: FT-IR spectra of single layer graphene oxide and graphite powder. 113
Figure 5. 2: Average spectra from Zeta potential analysis of graphene oxide (GO) sample 114
Figure 5. 3: FT-IR spectra of graphene oxide (GO), GO-Gd-DTPA and Gd-DTPA taken in the range from 600 cm^{-1} to 1200 cm^{-1} wavenumber. 116
Figure 5. 4: Typical Raman spectra for a single-layer graphene oxide in comparison with GO-Gd-DTPA material using a 514 nm excitation laser. Raman spectra taken in the range from 50 cm^{-1} to 3500 cm^{-1} 117
Figure 5. 5: Deconvolution of Raman spectra for a single-layer graphene oxide in comparison with GO-Gd-DTPA material using a 514 nm excitation laser. It was taken in the range from 800 cm^{-1} to 1900 cm^{-1} 118
Figure 5. 6: Plotted FT-IR spectra of single layer graphene oxide and graphite powder. 120
Figure 5. 7: UV-vis spectra of GO aqueous dispersions before and after being reduced for 6 hours and 12 hours. 121
Figure 5. 8: FT-IR spectra of rGO-Gd-DTPA and rGO with data baseline correction..... 124
Figure 5. 9: Typical Raman spectra for a single-layer reduced graphene oxide and rGO-Gd-DTPA sample. Raman spectra taken in the range from 500 - 3250 cm^{-1}. 125
Figure 5. 10: Deconvolution of Raman spectra for a reduced graphene oxide in comparison with rGO-Gd-DTPA material using a 514 nm excitation laser. It was taken in the range from 800 cm^{-1} to 1900 cm^{-1}. 127
Figure 5. 11: The variation of magnetic moment as function of magnetic field taken in the range of -15000 to +15000. Magnetic behavior between forward and reverse sweep of GO-Gd-DTPA (left) and rGO-Gd-DTPA (right) samples taken at room temperature. 128
Figure 5. 12: Hysteretic behavior between forward and reverse sweep taken from GO-Gd-DTPA and rGO-Gd-DTPA at room temperature. The concentration of the carboxylic group increase the slope of the graph. Even though the sample present paramagnetic behavior at room temperature. 129

List of Table

Table 3. 1: Preparation condition of functionalization of multi-walled carbon nanotubes. 47

Table 4. 1: Zeta potential and conductivity result of f-MWCNTs and pristine……...79

Table 4. 2: Titration results of pristine and f-MWCNTs……80

Table 4. 3: Percentage of Gadolinium in the each samples…….....100

Abbreviations

AFM	: Atomic Force Microscopy.
Ar-NH_2	: Aromatic amine
AFM	: Antiferromagnetic.
CFD	: Chemical functionalization degree
CMOS	: Complementary metal–oxide–semiconductor.
CNT	: Carbon nanotubes.
CVD	: Chemical vapor deposition.
DARP	: Defense advanced research project agency
DWNT	: Double walled carbon nanotube.
DEP	: Di-electrophoresis.
DI	: Deionized water.
DMF	: N,N-Dimethylformamide.
DRAM	: Dynamic Random-Access Memory.
DTPA	: Diethylene triamine Penta acetic acid.
Dy	: Dysprosium.
eV	: electron-volt.
EBL	: Electron beam lithography.
EF	: Fermi energy.
f-MWCNTs	: Functionalized multi-walled carbon nanotubes.
FC	: Field cooled.
FIB	: Focused ion beam
FESEM	: Field emission scanning electron microscopy.
FWHM	: Full width half maximum.
FM	: Ferromagnet.
FTIR	: Fourier Transform Infrared Spectroscopy.
Gd	: Gadolinium.
$GdCl_3$	: Gadolinium trichloride.
Gd – DTPA	: Gadopentetic acid.

Gd-Fctn-MWNT : Gadolinium functionalized multi-walled carbon nanotubes.

Gd-DTPA-f-MWCNT: Gadolinium Diethylene Triamine Penta acetic acid loaded functionalized multi-walled carbon nanotubes.

GMR : Giant magnetoresistance.

GO : Graphene oxide.

HCl : Hydrochloric acid.

HRTEM : High Resolution Transmission Electron Microscopy.

HDD : Hard Disk Drive.

HPLC : High-performance liquid chromatography.

IBM : International Business Machines Corporation.

IC : Integrated Circuit.

ICP/OES : Inductively Coupled Plasma Optical Emission Spectrometry.

IPA : Isopropanol.

KBr : Potassium Bromide.

L-AA : L-ascorbic acid.

MRI : Magnetic resonance imaging.

MRAM : Magnetoresistive Random-Access Memory.

MTJ : Molecular tunnel junction.

MWCNT : Multi-walled carbon nanotubes.

NaOH : Sodium hydroxyl.

NFM : Non-Ferromagnetic.

NMR : Nuclear Magnetic Resonance

NMP : N-Methyl 1-2-pyrrolidone.

NSTP-Lab : Nano-scale Transport Physics Laboratory

RAM : Random access memory

Oe : Oersted.

PMMA : Poly(methyl methacrylate).

rGO : Reduced graphene Oxide.

RF : Radiofrequency.

RKKY : Ruderman, Kittel, Kasuya and Yoshida.

SAF	: Synthetic antiferromagnetic.
SEM	: Scanning Electron Microscopy.
SMM	: Single Molecular Magnet.
SQUID	: Superconducting Quantum Interference Device.
STM	: Scanning Tunneling Microscopy.
STS	: Scanning Tunneling Spectroscopy.
SWCNT	: Single walled carbon nanotubes.
TEM	: Transmission Electron Microscopy.
TMR	: Tunnel magnetoresistance
VTI	: Variable Temperature Insert.
VSM	: Vibrating Sample Magnetic
ZFC	: Zero Field Cooled.
μB	: Bohr Magneton.
μ_{eff}	: Effective magnetic moment.
$TbPc_2$	: bis (Phtalocyaninoto) terbium (III).
UV-vis	: Ultra-violet visible spectroscopy.

Chapter 1

Introduction

Carbon nanotubes (CNTs) have gained since 1991 until now a great waves of consideration from the scientific network, mostly because of their precious physical properties. The vast majority of interest is concentrated on the practical uses of CNTs. Even though, they utilized them in different applications. Generally, the materials are used for magnetic storage information; the fundamental parameter is the turn of spin of the electron, as this turn of spin can be suspected of as the central cause of magnetic moment [1]. Most of the electronic device works on the charge property of the electron. The spin of the electron especially those are coming from orbital magnetic moment can also be use in the charge transfer process to facilitate contrast to conventional electronic devices [2, 3] . Moreover, it is regularly important to modify the CNTs to enhanced magnetic interaction of the material. This can be done in different ways. One of these ways might be to fill them with outside materials, with the goal that the properties of the host CNTs would be changed because of their interaction with the filling material. This makes CNTs indispensable in various sectors such as electronics, spintronic and/or energy [4].

Nanotechnology has also turned to biomedical applications in recent year, [5]. The remarkable properties of nanoscale structures (mechanical, magnetic, optical, thermal, chemical, surface reactivity) have enabled nano particles to be used in health, including imaging and/or therapy. Indeed, gadolinium is known as the best contrast agent for this purpose. When Gadolinium linked with organic macromolecule to form magnetic chelate and further attached with CNTs. They can accumulate at tumor sites due to the EPR (Enhanced Permeability and Retention Effect) and pass many biological barriers [6, 7]. The nanoparticles therefore offer new possibilities for treating and detecting diseases with sizes similar to biological macromolecules [8]. For the time being, intratumoral injection is the most clinically used technique for maximizing nanoparticles in tissues to the maximum while

limiting their spread in the body [9]. Actually, researchers focused to develop theranostic nanoparticles to have both therapeutic and therapeutic properties Diagnostics [10]. Therefore, these surface modifications of CNTs allow therapeutic agents or nanoparticles to add complementary properties [11, 12]. Trivalent gadolinium cation can be picked up by macrocycles in order to appropriate imaging techniques [13]. This is called a theranostic nanohybrid, i.e. combining both therapeutic and diagnostic properties.

Multiple routes were proposed for attaching the magnetic impurity on the surface of MWCNTs. For instance, Gd-DTPA chelate made from precursors $GdCl_3$ and DTPA was mechanically added on the CNT surface by compressing both MWNCTs and Gd-DTPA together where the chelate would get deposited on to the inherent defect of CNT [14]. Hence, chemical method via covalent bonding of magnetic impurity chelate on to the surface of CNTs found be efficient in forming a single nanocomposite compound.

In this thesis, gadolinium diethylenetriamine pentaacetic (Gd-DTPA) magnetic chelate will be used to chemically modify CNTs. The used of Polyamino-carboxylate (DTPA) enables to form stable complex with radioisotopes and gives high performance in term of sensibility in the MRI. The functionalized CNTs with carbonyl group prepared in the different reaction temperature, giving ability to be able control the chemical loading of the carbon nanotubes. This can bring to the carbon nanotubes novel magnetic properties, which can be useful in several application. In addition, nanoscale magnetic material attracts currently attention of the scientific community because of their demand and various application in different field, including spintronic and quantum information processes. Single magnetic molecule can be considered as materials with the magnetic anisotropy energy. In fact, this exploit spin and charge property of electrons. The single graphene sheets after being chemically modified. It can be categorized as good candidate in this purpose. As part of this work, graphene oxide and reduced graphene oxide were modified with Gd-DTPA magnetic chelate to investigate spin glass behaviors in the materials understudy. For this thesis, special attention brought in the magnetic and nano transport properties of the materials understudy for nanoscale device fabrication.

1.0. Background on carbon nanotubes

The production of one dimensional semiconducting materials known as nanowires has released the significant opportunity to the development of the several miniaturized devices. Carbon nanotube holds incredible mechanical, electrical, optical and thermal properties indeed can definitely be used in a different industry [15, 16, 17]. Carbon nanotubes have an aspect ratio of length to diameter of up to 10^8 (greater than 10 centimeters in length to 1 nanometer in diameter) [18, 19]. Thus far, they are still among those who having the stiffest and lightest recognized materials with the tensile strength measured up to 63 gigapascals [20] due to the sp^2 hybridized bonding structure. Moreover, CNTs have begun showing up in materials ranging from tennis rackets to paint in order to improve their strength while not adding significantly to their weight.

Although the electrical properties of carbon nanotubes are basically no less spectacular than the mechanical ones, and certain silicon chip companies such as Intel and IBM have revealed a deep interest in substituting parts of computer chips with SWNTs. Based on theory, CNTs are characterized by their diameter which is often smallest, few centimeters long and very thin materials. Which can be arranged in two categories, single walled carbon nanotubes SWCNTs have a 0.3 nm (nano-meter) with length about 10 centimeters [21] and multi-walled carbon nanotubes MWCNTs which can be range between 2-100 nanometers. These MWCNTs are often used to enhance mechanical and electrical properties of composite materials and for field emission devices while SWCNTs are more allocated for transistors devices fabrication due to their smaller size dimension and appreciable electrical properties. A single metallic carbon nanotube can be able to carry a current density up to ~ 10^9 A/cm^2 [22]. Therefore, semiconducting carbon nanotube, they have high on/off ratios of ~ 10^6 current ratios at the bias voltage region [18, 22]. Single walled carbon nanotubes, hold exceptional mechanical and electronic properties stemming, from the zero band gap, semiconductor graphene structure.

Double-walled carbon nanotubes DWCNT have a 0.35 – 4 nm and presenting appreciable lifetime, current densities for the field emission and good band gaps. However, these intermediary properties, which are between SWCNT and MWCNTs,

is essentially used in field effect transistors [23]. Theoretically, DWCNT behaves as a metal which offers a good point for DWCNT being useful for many applications [24].

Subsequently, carbon nanotubes have also been studied extensively as chemical and gas sensors [25, 26] due to be having entire carbon atom on the outside of the tube, which leads to be having a very high surface area. It is preferably used more of carbon nanotubes rolled-up sheets of graphene, which gives the physical and electrical properties of graphene more interesting for future work.

Those graphitic materials differ in their electronic properties, the specific surface-volume ratio and the electronic properties fluctuates from the ones of their bulk counterpart, which can be because of quantum confinement. In addition, they are ideal used for field effect transistor, due their extreme high carry mobility and ballistic transport properties. Nevertheless, they can be very useful in numerous semiconductor industries for electronic devices fabrication for example, gas sensing at which has gained a good performance [27]. In one way, these devices are operated at the temperature range of about hundreds degree. Other way, need to have an appreciable magnetic moment, which can be useful for any other application. This induced to lower the power consumption and peculiar dimension of the devices. Consequently, they can lead to have the first idea about fabrication of new devices with modified carbon nanotubes and graphene with a good magnetic moment.

However, it is obvious that current passing through the nanowires devices heat the nanowire itself, by the Joule effect [28]. This resulted in focused ion beam lithography to be used to connect the metallic electrodes to the nanowires [29, 30]. It is subsequently clearly that to avoid the heat transfer by conduction between nanowire and substrate, suspended single nanowires can be produced. Moreover, among the disadvantage of this technique, carbon contamination is essentially taken place in the metal/semiconductor surface contacts [31]. By searching of the technique to overcome the metal/semiconductor surface contact and optimized contamination problem, electron beam lithography can be considering as remedy of this situation because is more feasible in a medium scale production workflow.

Recently, many works have been done on single layer graphene sheet due to its extraordinary electrical properties, optical, and mechanical properties. This year, graphene functionalized with carboxylic group and anchored Co_2O_3 nanoparticles was synthesized to make graphene-magnetic nanoparticle [32]. Which are gaining great intension because of their multifunctional and novel properties [33, 34]. These materials showed the magnetostatic dipole interaction for the particles beyond one nanometer [35]. This composite holds wide variety of applications in many field such as catalysis, optoelectronic materials, MRI, drugs delivery etc. [36].

In other hand, gadolinium metal necessary used as reagent contract in MRI. It can present great effect on electronic and magnetic properties when is being attached onto multi-walled carbon nanotubes, as well as single layer graphene oxide. This work modified three materials such as multi-walled carbon nanotubes (MWCNTs), graphene oxide (GO) and reduced graphene oxide (rGO) with magnetic chelate molecular namely Gadolinium Diethylenetriaminepentaaceticacid (Gd-DTPA).Which follows by comparative study on the electronic and magnetic properties of the materials understudy.

1.1. Carbon and its allotropes

Carbon belongs to fourth family and is sixth element in the periodic table with four valence electrons, two in *s*-orbitals and two others in *p*-orbitals. It is chemically similar to silicon and germanium due to outer shell electron's number. In term of the energy difference inside the valence band, atomic orbital is very small, and is allowed open-hand development to hybridization. Therefore, there are four types of known allotropes of carbon, which can be arranged as follows: Carbon nanotubes CNTs (which gives birth to single and multi-walled), fullerenes, graphite (graphene) and diamond [21]. This does not exclude the amorphous known under generic names coal, charcoal and lamp black. The following parameters can differentiate the amorphous and other allotropes of carbon, the physical appearance, mechanical and electrical properties.

CNTs are characterized by their diameter, few centimeters long and very thin materials. CNTs are rolled up graphene sheets in a cylindrical form with diameters of few nanometers and lengths ranging from few microns to centimeters. CNTs can be further classified into Single Walled Carbon Nanotubes (SWCNTs) made of single rolled up graphene sheet and Multi Walled Carbon Nanotubes (MWCNTs) made of multiple rolled up graphene sheets stacked one on another. The tube layers of the MWCNTs are weakly hold by Van der Waal forces.

This force linking two nanotubes together in a crystal is estimated at 0.8 eV per nm of contact, which is huge if we consider that a nanotube is commonly measuring a few micrometers [34, 35]. It is therefore important to break these bundles and individualize the CNTs. Even though theirs solubility in certain solvents are very difficult because of the hydrophobicity of carbon nanotubes.

These MWCNTs are often used to enhance mechanical and electrical properties of composite materials and for field emission devices while SWCNTs are more allocated for transistors devices fabrication due to their smaller size dimension and appreciable electrical properties. Figure 1.1 gives illustration of the picture of allotropes carbon.

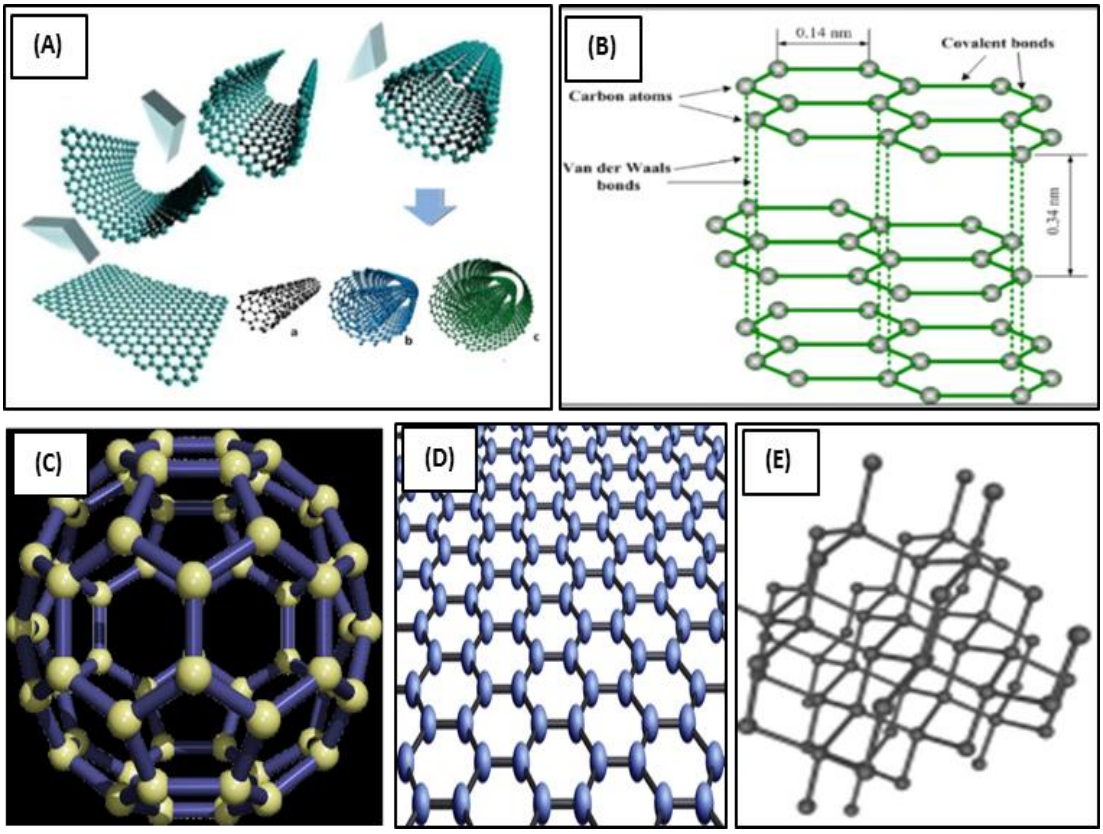

Figure 1. 1: Crystal structure of certain allotropes of carbon: Carbon nanotubes (A), graphite (B), Fullerene (C), graphene (D), Diamond (E) [37, 38, 39, 40].

The structure of a CNT can be describe from a single layer of graphite which is basically namely as graphene. A narrow strip is cut out from the sheet in a specific direction and, then rolled into a seamless cylinder as represented by the Figure 1.2.

This pull off carbon nanotube depends often on the direction that the sheet is cut, and will influence the CNT to be having a different structure affecting generally its electronic properties and other properties. The circumference of CNT can be expressed by considering the following equation:

$$c = n\vec{a}_1 + m\vec{a}_2 \qquad [1.1]$$

where:

$\vec{a}_1$ and $\vec{a}_2$ are unit vectors of the hexagonal planar lattice,

m and *n* are the integers numbers which gives the information about the chirality, sometime are called Chirality indices.

CNTs with equal value of *n* and *m* can be assigned to armchair, those contain whom are having the value of *n* is equal to zero referred to zigzag and the remaining CNTs have been called chiral tubes.

In term of diameter of a CNT, the proposed formula can be used to calculate CNTs diameters from the chirality indices, which can be written as:

$$d = \frac{\sqrt{3a_{C-C}}\sqrt{m^2 + nm + n^2}}{\pi} \qquad [1.2]$$

where:

a_{C-C} is given by the value of 1**,**42 Å, the distance between closest carbon atom [41].

Figure 1.2 explains CNTs formation with different shape, two fundamental vectors specified by the a_1 and a_2. The vectors came from the origin, which can be illustrate along a direction OT and OA gives a chiral CNT, rolling into a cylinder shape via point O and A. where θ is the chiral angle. Single Grey part defines the unit cell, zigzag and armchair are represented by two solid line with circumference of the CNT is assume given by the vector C. Moreover, certain experimental work based on the carbon nanotubes has been reported that, it can be possible to produce graphene ribbon from CNTs structure. [21, 42].

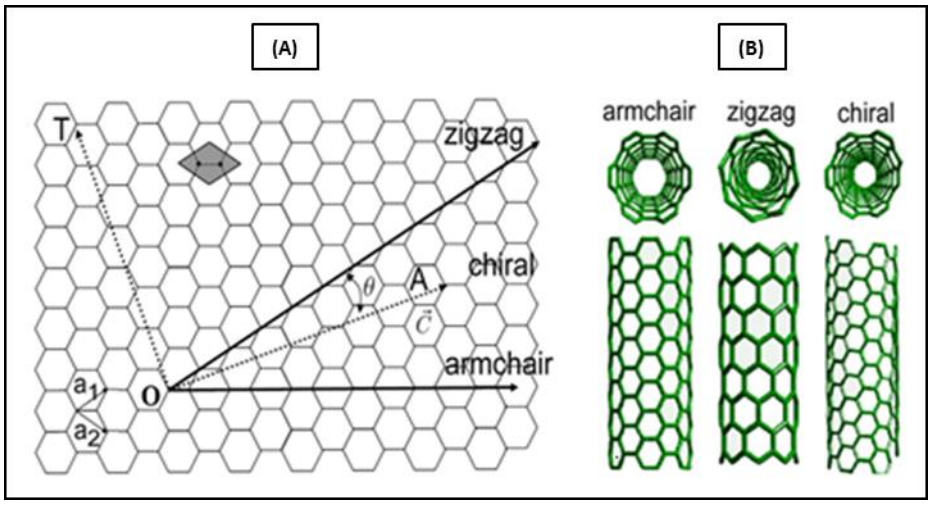

Figure 1. 2: Two dimensional hexagonal lattice (A), Different types of CNTs (B) [43].

1.2. Properties of carbon nanotubes

Generally, the SWCNTs can be consider with rolled-up shape sheet and are originated from graphene, while the MWCNTs are made up with two or more concentric SWCNTs. These CNTs are usually synthesizing by different techniques, having similar electronic properties, thermally stable and good structures, which can be consider that created from graphene. The π bonds that originate from the p_z orbitals that extend perpendicular to the graphene plane can be resulting to delocalized electrons and give rise to resonance, having the energies bands close to the Fermi level although only electrons near the Fermi level usually have energies more or less close to those of unoccupied states; these bands dominate the electrical characteristic.

Furthermore, this lead to categorized CNTs into metallic or semi-metallic material. MWCNTs appeared more metallic than individual just as a system of SWNTs at low temperatures [44]. However, at higher temperatures there is no transformation to metallic temperature. This is steady with a model of conduction that expresses the transport of electrons is by means of the external shells. As the inner shells, the transfer is reduced the impacts of quasi-1D-suppression of backscattering.

The high frequency properties of CNTs have smaller resistivity than copper, as they are not negatively impacted by surface scattering [45]. It is evident that bulk resistivity of copper is about 1.7 Ω m. However, as the copper feature size shrinks below 100 nm, surface scattering increases this resistivity [45]. There is a theoretical model shown that bundles of SWNTs could overtake Cu, provided SWNTs have resistance, inductance, and capacitance values at large frequencies that are reliable with predictions for ballistic conductors with quantized energy states [46]. In relation with magnetic properties of carbon nanotubes. In total absence of the impurities, the carbon based on nano materials rely to be magnetic [47]. The magnetic properties of CNTs are governed by the chirality, the arrangement and concentration of the vacancy.

1.3. Synthesis method of CNTs

Many techniques are currently developed for synthesis of CNTs, due to their useful application for computer industry like Intel or IBM used them as major composite materials for interconnection in their computers ship. However, DC arc discharge or carbon arc method is among the known the first method used to create CNTs [48].
A similar method was employed by D.S. Bethune *et al*. [49] to specifically favor production of CNTs. Figure 1.3 gives the morphology detail and image taken by that method. In fact, 20 years ago, Richard Smalley *et al*. [50] first used laser ablation method affording approximately 70 % conversion of carbon material into single-walled carbon in 1996. Self-organized into ropes or bundles containing more or less hundreds of SWNTs [51]. Consequently, those synthesis methods encounter certain issues related to pure isolation of carbon nanotubes form its matrix for electrical study.

Moreover, chemical vapor deposition (CVD) was still used. But it has been improving with matter of time and resulting to the clean isolated single walled carbon nanotubes with a larger length compare to other methods. Figure 1.4 shows schematic diagram of the CVD oven in the Hone lab during the experiment as well as two digital pictures of the laboratory setup. And the results obtained of SWNTs coming from patterned catalyst islands that were grown by the CVD method.

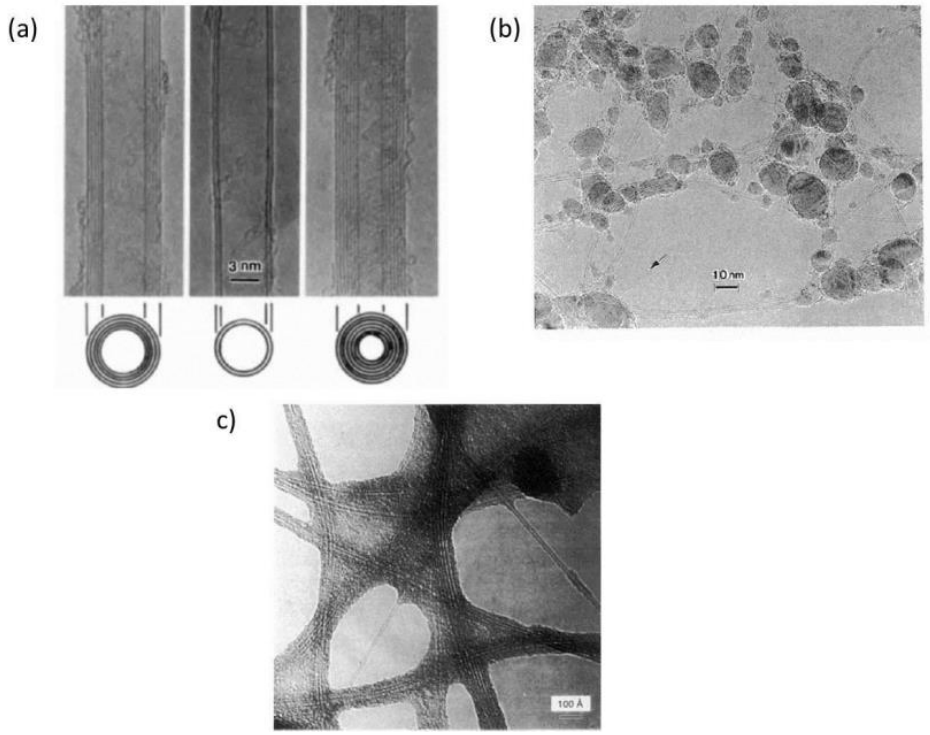

Figure 1. 3: (a) The MWCNTs that resulted from the first growths using the arc discharge method [52]. (b) The first SWNTs from the arc discharge growth method by Iijima *et al.* [53]. (c) The SWNTs from the arc discharge growth by Bethune *et al.* [49].

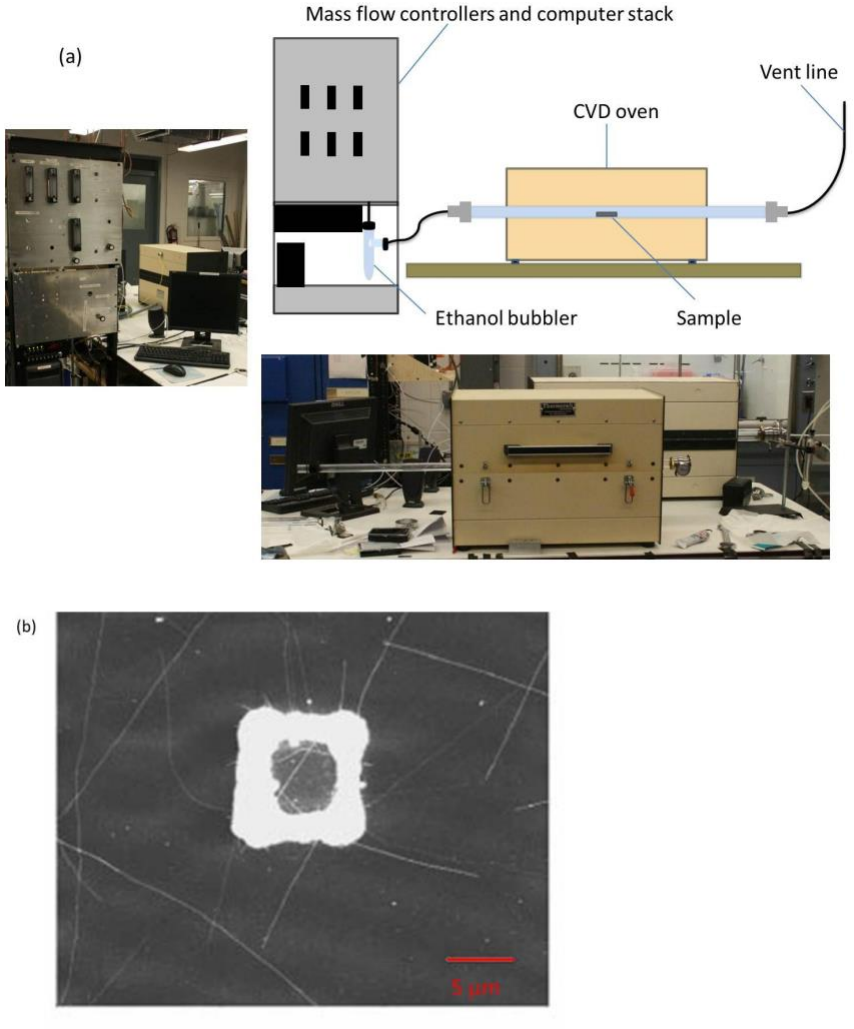

Figure 1. 4: (a) Schematic diagram of the CVD oven in the Hone lab as well as two digital pictures of the setup. (b) The results of SWNTs coming from patterned catalyst islands that were grown by the CVD method [54].

1.4. Different method of functionalization

Generally, chemical functionalization of the multi-walled carbon nanotube can change the electrical, structure and magnetic properties of MWCNTs due to creation bond or breaking during the chemical reaction processes. This change can be improved or defected properties of CNTs. Nevertheless, carbon nanotubes could be modified either inner or outer of the tubes. Endohedral (functionalization from inside): CNTs are suspended in a colloidal solution that contains desired nanoparticles. Later the nanoparticles would enter the inner tube of CNTs through capillary action. Finally, the suspension would be evaporated resulting the CNTs with filled nanoparticles. Note that

the nanoparticles should be of less size than the diameter of the tube. Exohedral (Functionalization on the Outer side): This can be achieved by treating CNTs with acid mixture where defects are introduced on to the outer surface of the tube.

Several methods can be used to functionalize carbon nanotubes with the organic group. Figure 1.5 illustrates different chemical method of surface functionalization of the carbon nanotubes.

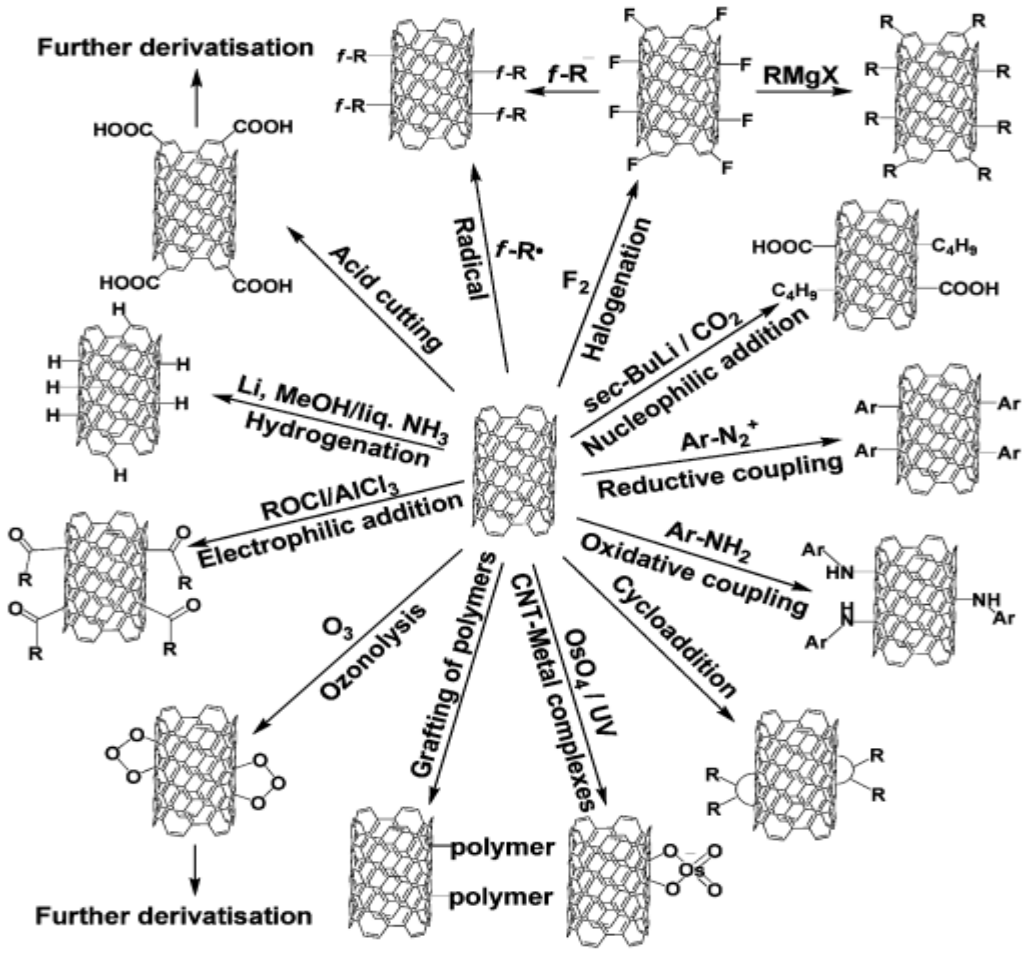

Figure 1. 5: Schematic diagram of different chemical method of surface functionalization of MCNT [55].

However, it is very difficult to modify graphene with type of chemical reaction mentioned above even though they are allotropes of carbon. The graphene can be modify via chemical reaction involving many chemical reactants. The graphene oxide (GO) which the structure contents sp^3 bond carbon atoms are composed of different organic functional group such as carboxylic, epoxy, hydroxyl.

1.5. Chelate system form with functionalized MWCNTs

Many organic group can be attached to MWCNTs such as amine, hydroxyl, carbonyl, or sulfonyl. This attachment depends on the vision of application of the material. For example, enhanced water solubility, dispersion and toxicity of the carbon nanotubes or transport of the macromolecular into the cell. The carbonyl group has well chemically bonded with MWCNT due to C-C bond. Although pristine MWCNT is chemically inert and insoluble in water.

It is possible to attach by aggregation or affinity the macromolecule. However, by modifying MWCNT it can, formed chelate via covalent bond linking carbon nanotube and chelate molecular, whether by aggregation or by affinity to the multi-walled carbon nanotubes. Therefore, this modification allows the multi-walled carbon nanotubes being coupling with protein, oligonucleotide, peptide or any other macro molecule.

Certainly, the oxidation of MWCNT conducts to introduce -COOH and -OH group into the MWCNT and is often obtain by using acid, ozone or plasma. Indeed, this carbonyl group is useful site of any modification of the surface of the MWCNT. The covalent linking metal via chemical reaction is the most utilized method to attached chelate to the functionalized CNT. In fact, chemical processes, involving several chemical solvents, essentially do this. Therefore, the unzip multi-walled carbon nanotubes as graphene might naturally give different interested properties, whereby graphene can be firstly functionalized and attached macromolecule on it. Figure 1.6 gives the typical example of covalent linking DTPA on the carbonyl group of the functionalized carbon nanotubes.

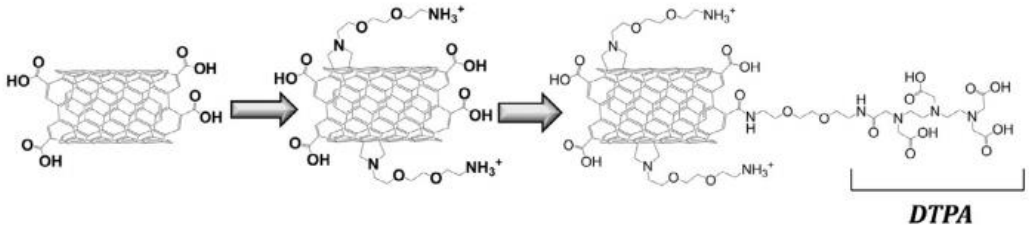

Figure 1. 6: Typical example of DTPA linked with functionalized carbon nanotubes [56].

1.6. Graphene and Method of synthesis

Graphene is considered as sensational material of the twenty-first century. Which has a one-atom-thick 1D planar sheet of sp^2 bonded carbon atoms. The electronic properties attracted attention of many researchers in the materials science field [57, 58]. These days, Graphene can be produce using several method such as micro-mechanical exfoliation of pyrolytic graphite [59], epitaxial growth [60, 61, 62] and chemical vapor deposition (CVD) [63, 64]. Chemical method that is known as Hummers method can be consider among of the excellent way of graphene production.

This method is economical and pointed interest towards graphene synthesis. However, graphite can be qualified as major composite for graphene production. Hummers method consists to convert graphite to graphene which is firstly to oxidize the precursor of the graphite, to obtain graphene oxide (GO) and reduction of GO to pure graphene. Actually, graphene has gained an excessive attention of the scientist because of is extraordinary properties and useful application in many sector. It can be used in electric devices, functional film, and energy storage devices etc. [56, 65].

This project will be going in parallel with graphene oxide synthesis to improve hummer's method, modification of conversional process and the optimization of the process as will be shown in the details Chapter 3 section 2. Figure 1.7 shows the hummers method modified taken form H. Yu *et al.* [66].

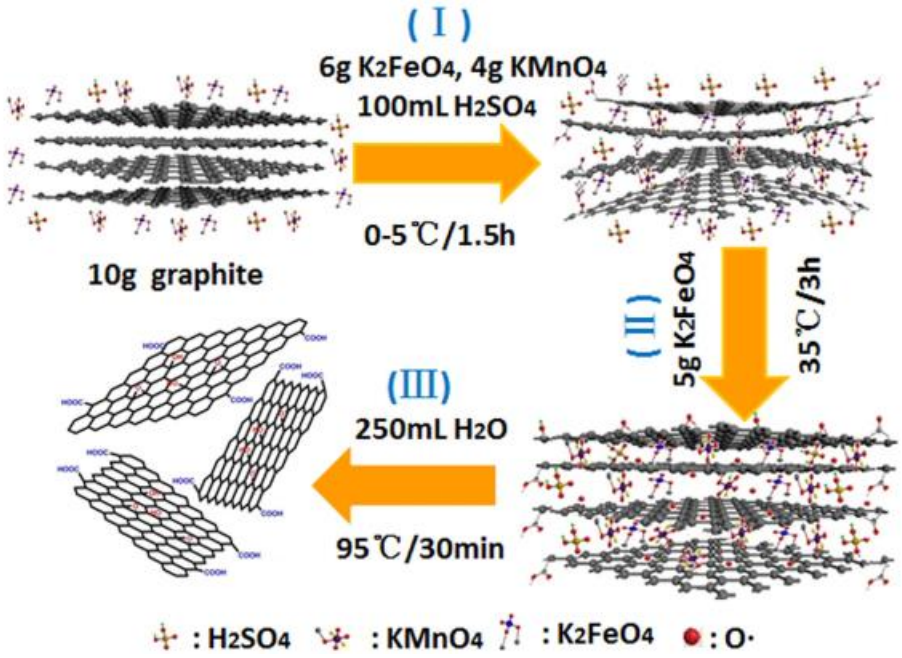

Figure 1. 7: Illustration of preparation of graphene oxide GO from graphite material [66].

Certainly, this hummers method lead to graphene oxide (GO) which can be used for drug delivery system. It is also a symbolic of host–invitee interactions in supramolecular chemistry, where the *host* and the *guest* molecules or ions are linked non-covalently generally by means of hydrogen bonds, ionic bonds, Van der Waals interactions and hydrophobic bonds [67].

1.7. Chemical modification of graphene

The chemical synthesis of magnetic metal complex nanoparticles has been the subject of extraordinary research because of their technological applications in differing fields, for example, magnetic storage, magnetic recording, also, magnetic sensors [57, 58] and in various field like medical science such as MRI and drug delivery. However, graphene converted into graphene oxide (GO) which the structure contents sp^3 bond carbon atoms are composed of different organic functional group such as carboxylic, epoxy, hydroxyl. These organic groups played a role in attachment of macromolecule on the surface of graphene sheet.

Many works have been done by incorporating metal oxide onto graphene. Last year, graphene functionalized with carboxylic group and anchored Co_2O_3 nanoparticles was synthesized to make graphene-magnetic nanoparticle [32]. Which are gaining great intension because of their multifunctional and novel properties [33, 34]. These materials showed the magnetostatic dipole interaction for the particles beyond one nanometer [35]. Gadolinium oxide nanoparticles have been used modified graphene oxide to improve the T1 and T2 contrasts of MR images [68].

1.8. Aims and objectives

The aim of this research project is to investigate the magnetic properties of the modified multi-walled carbon nanotubes and graphene materials followed by the device fabrication. To meet the above aim, the following objectives will be investigated:

- Functionalized carbon nanotubes with carbonyl group using sulfuric and nitric acids.
- Functionalized graphene with carbonyl group via modification of Hummers method
- Covalent linking of gadolinium chelate incorporation in the functionalized multi-walled carbon nanotubes, graphene oxide and reduced graphene oxide. The gadolinium will firstly be bonded with DTPA and further loading of the complex onto surface of the CNTs, graphene oxide and reduced graphene oxide.
- Investigation of the structural properties the materials under study and complex molecular synthesized.
- Investigation of electrical properties, electronic structure, morphology of the following organic novel materials; covalent linking Gd-DTPA chelate with Functionalized multi-walled carbon nanotube and graphene oxide and reduced graphene oxide.
- Study of the magnetic behaviors of this synthesized novel material understudy at very low temperature 5 K, high field about 12 T, magnetoresistance, temperature dependent resistance, and I-V characteristics.

1.9. Thesis outline

Chapter 1 gives the introduction of this work, briefing on carbon and its allotropes, different method of functionalization of carbon nanotubes, graphene associated with method of synthesis of graphene. Followed by chemical modification of graphene with super macro molecule. The aims and objectives of the study are outlined in this chapter 1.

Literature review on the multi-walled carbon nanotubes and graphene which are related on electronic and magnetic properties, associated with the synthesis of the materials under study. Including theory of the spintronic, magnetism and fabrication techniques of the devices. The theory on Gadolinium element and Diethylene triamine penta acetic acid are also discussed in this chapter 2.

Chapter 3 focuses on the experimental details of the sample preparation, characterization techniques used and details on device fabrication at Nanoscale transport physics laboratory, School of Physics., Wits University.

Chapter 4 is dedicated to the overall result obtained by different characterization techniques such as FT-IR, Raman spectroscopy, FE-SEM, Zeta potential, Acid-base titration, ICP and magnetic measurement of carbon nanotubes materials under study.

Magneto-transport data obtained from graphene oxide and reduced graphene oxide, including FT-IR, Raman, acid-base titration and ICP/OES analysis together with corresponding results will be discussed in this chap 5.

Finally, chapter 6 gives a summary of the work with conclusion and recommendations. Appendices described the fitting procedures applied to the data acquired by some characterization techniques and displayed zeta potential raw spectra.

Chapter 2

Literature review

This chapter will be explaining the main concepts behind carbon nanotubes and graphene, which are the core materials in this project. Furthermore, it gives the basics of spintronic, including their devices fabrication. It is also shows the results obtained on the investigation of physical properties of the graphene oxide, reduced graphene oxide and carbon nanotubes reported by different research work and their applications.

2.1. Background of spintronics

Spintronic is a new field of science and technology exploiting both intrinsic spin and charge of the electron in a device. In a simply word, spintronic means ‘‘spin transport electronic’’ which was firstly presented in 1996 assign to a program of US. Called Defense advanced research project agency (DARPA) [69].

Conventional electronic devices made by silicon chips. It uses charge of the electron for the transport purpose in semi-conductor materials. The important point of spintronic is to provide low power, high speed and high-density logic and memory electronic devices. Generally, spintronic devices are operating in three steps; firstly, the information is kept (written) into spins. These spins orientation can be up or down direction. Secondly, they have been attached to mobile electrons; carry the information along a wire. The last step, the information is going to be read at the terminal. In fact, it takes long time of approximately 10^{-6} s for spin orientation of conduction electron to survive. This makes spintronic devices very interesting compared to conventional electronic device.

Electronic devices such as; Spin-valve, Spin current amplified, Spin capacitors, Spin-based integrated circuit, Spin LEDS and Spin lasers. Those electronic devices functioned under a sufficient interaction between transport electrons and local

magnetic moments resulting from two magnetic layers. Moreover, two main effects can be monitored in this purpose. Giant Magneto-Resistance (GMR) and Magnetic Tunnel Junction (MTJ) effect as discussed in detail in the next section.

2.1.1. Giant magneto-resistance effect

Historically, Peter Grünberg of Forschungszentrum Jülich (Germany) and Albert Fert of the University of Paris - Sud (France) first discovered this effect in 1988. While they were working independently [70]. Grünberg examined a Fe/Cr/Fe trilayer system, and Fert considered in Fe/Cr multilayer system. After some years, Nobel Prize (2007) in material science (physics) was granted to Grünberg and Fert for their hard work of discovery of giant magneto-resistance GMR, which is considered as the birth of spintronics [70].

GMR is the change in electrical resistance when a magnetic field is applied. It is a quantum mechanical effect in thin films structures, made out of alternating ferromagnetic and nonmagnetic layers. Figure 2.1 gives schematic diagram of this effect. It necessary shows that, the spin orientation depends on the applied magnetic field. The inserts of Figure 2.1 (a) shows the change in the resistance of the magnetic multilayer as function of applied magnetic field. While the Figure 2.1 (b) describes magnetization of the multilayer with varying magnetic fields: the magnetizations are aligned antiparallel at zero field; follows by the magnetizations are aligned parallel when the external magnetic field H is larger than the saturation field H_S. Figure 2.1 (c) illustrates the plot of magnetization against the field denoted by H of the multilayer material.

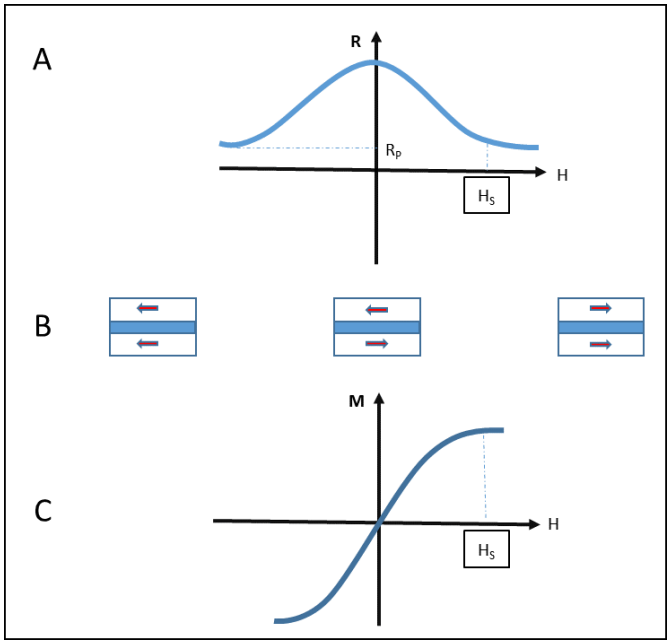

Figure 2. 1: Schematic representation of the GMR effect showing; (A) the resistance of the multilayers against the field. (B) Conditions of the GMR effect. (C) Plotting of magnetization as function of field.

However, it can be used the argument of the Mott model which was proposed to explain the increase in resistivity and/or resistance of a ferromagnetic metal over its Curie temperature [71]. The electrons in a magnetic metal travel in two free channels coinciding the spin orientation up and down; henceforth the conduction happens in parallel inside two spin channels. In addition, the electron scattering for the spin up and/or spin down is free with the goal that the density of states (DOS) at the Fermi level is not the equivalent. This effect is exploited in the production hard disk drive in the manufacture company.

2.1.2. Magnetic Tunnel Junction effect

M. Jullière (College of Rennes, France) initially discovered the magnetic Tunnel Junction effect in 1975 in the investigation of Fe/GeO/Co junctions at 4.2 K [72]. Maekawa and Gäfvert first detailed room temperature tunneling effect in 1982 with an arrangement of Ni/NiO/FM system, where FM is Fe, Co or Ni [73]. Tunneling magnetoresistance (TMR) is characterized as an adjustment in the electrical resistance of a magnetic tunnel junction (MTJ) due to an outer magnetic field.

A MTJ comprises of two ferromagnetic metals which are the terminals electrodes isolated by a non-magnetic layer namely tunnel barrier.

The Electrons can tunnel through the tunnel barrier if this has very thin layers (nm). This tunneling phenomenon of the electron is related to the wave nature of the electron. However, this ephemeral transmission of electron through the tunnel barrier leads to the exponential reliance of the dependence of the tunneling current with the barrier thickness. That can be assigned with Simmon's expression [74] given by:

$$I(V) = f\left(t_b\right)\left[\left(\bar{\phi} - \frac{V}{2}\right).e^{-\left(1.025\sqrt{\bar{\phi}-\frac{V}{2}}\right).t_b} - \left(\bar{\phi} + \frac{V}{2}\right).e^{-\left(1.025\sqrt{\bar{\phi}+\frac{V}{2}}\right).t_b}\right] \qquad [2.1]$$

where,

I is the tunneling current, $\bar{\phi}$ and V are the average tunnel barrier height and bias voltage across the junction in volts, respectively. t_b is the barrier thickness measured in angstroms.

The external magnetic field governed the direction of the two magnetizations of the ferromagnetic. When the magnetizations are in a parallel orientation, more flow of electrons will be tunneling through the insulate layer. Less tunneling current if they are in opposite (antiparallel) orientation. Consequently, this junction switched between two states of electrical resistance, one with low and one with very high resistance. Figure 2.2 gives two current model for parallel and anti-parallel orientation of the magnetization. While red arrows indicates flow of the electron passing through the tunnel barrier.

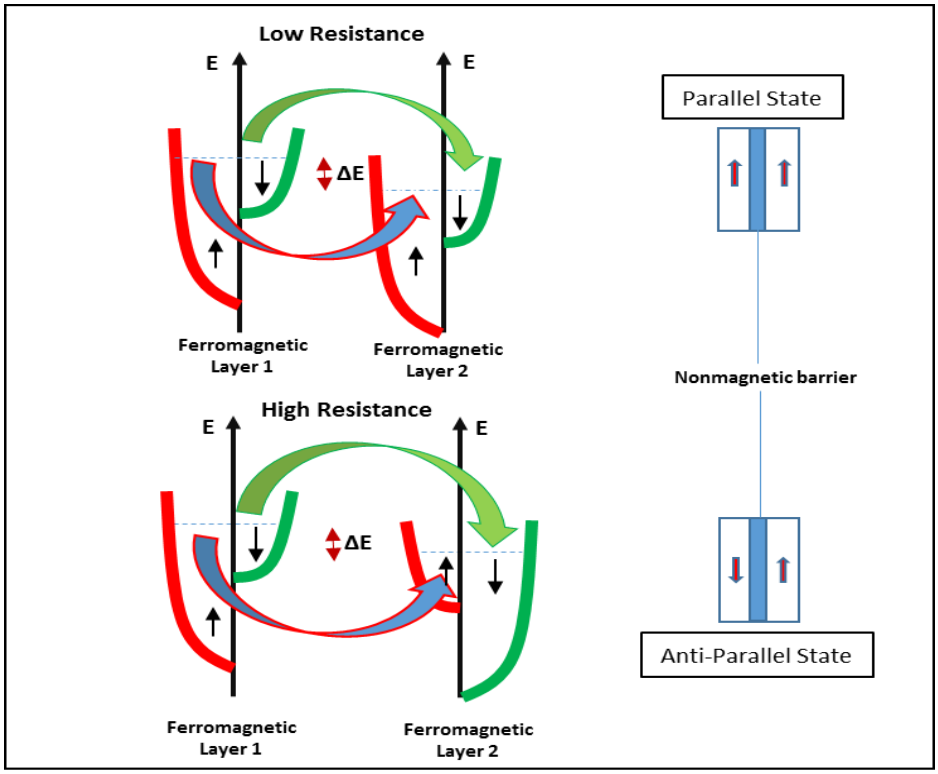

Figure 2. 2: Schematic diagram of tunneling magnetoresistance effect.

Tunnel magnetoresistance has been explained by using the Bardeen's approach of tunneling [75], as being determined by overlap of wave functions entering the tunnel barrier with the terminals electrodes with a little transmission probability. Tunnel magnetoresistance ratio (TMR ratio) is determined the difference in term of the conductance of the parallel and anti-parallel orientation is given by Julliere's model by:

$$TMR_{Ratio} = \frac{G_P - G_{AP}}{G_{AP}} = \frac{2G_P G_{AP}}{1 - G_P G_{AP}} \qquad [2.2]$$

The term G_P and G_{AP} denote the conductance of both parallel and anti-parallel states.

2.1.3. Spintronic Devices, carbon nanotube and graphene in spintronic

Giant magneto-resistance (GMR) and magnetic tunnel Junction (MTJ) have identical sandwich-like structure, which incorporates two ferromagnetic layers isolated in the middle by a non-magnetic layer. This non-magnetic layer is necessary a metal layer for example chromium, copper, ruthenium, etc. in GMR devices and, the insulator layer like amorphous Al_2O_3, crystalline MgO in MTJ device [76]. The device resistance depends on the two ferromagnetic layers. When they have the parallel magnetization direction, the device resistance is low while the opposite direction, it will show high resistance as indicated in the Figure 2.3. Those two fixed ferromagnetic layers have whether high or low field/current. It refers to use synthetic antiferromagnetic (SAF) structure to get high switching field/current. That has pinning layers, and two ferromagnetic layers separated by a thin 0.8 nm ruthenium in the middle [77].

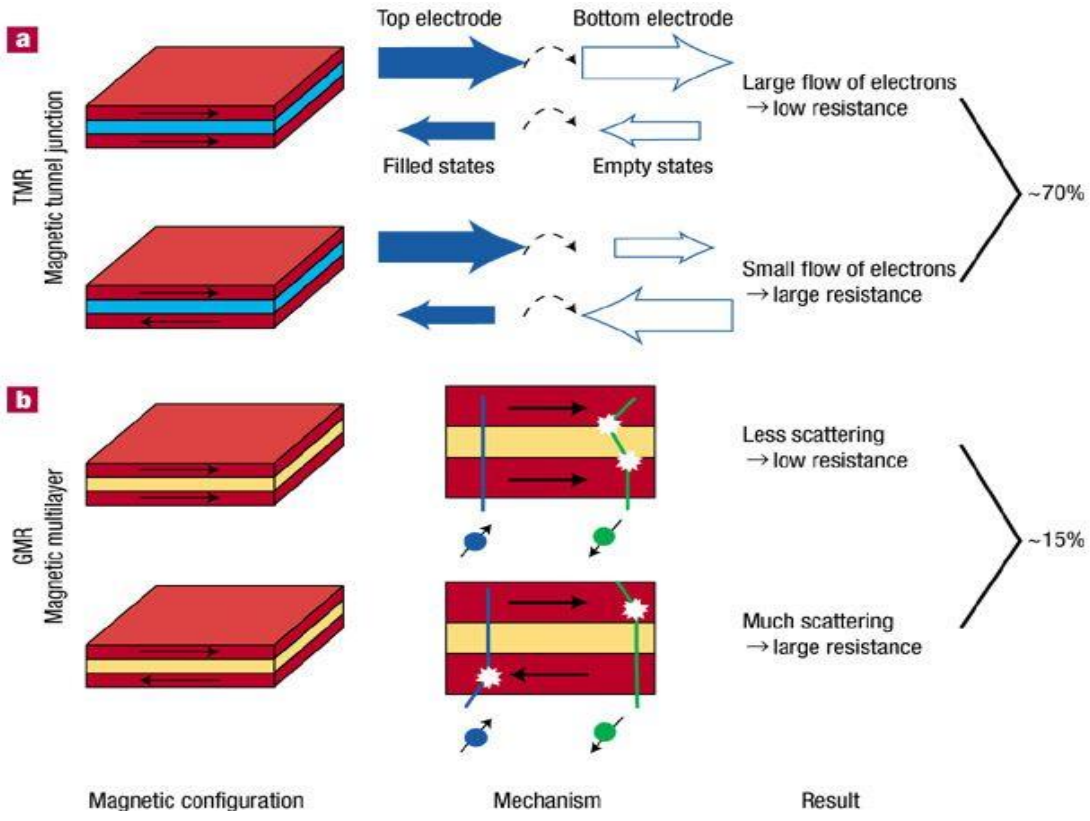

Figure 2. 3: Configuration of magnetic tunnel junction device TMR (a) and giant magneto-resistance GMR (b). Indication of spin of electron direction relates the resistance of the spintronic device [77].

The amplitude of current that can switch magnetization was theoretically predicted by some researchers [78], and demonstrates experimentally the current induced magnetization switching in Co/Cu multilayers structure [79]. In spintronic devices, an applied magnetic field is often used to switch the free layer magnetic and current line to generate the magnetic field. The amplitude of the current needs to generate enough magnetic field. It cannot be reduced with the device scaling. Spintronic based device has a potential benefit of functionalities such as low power dissipation, non-volatility, faster computing and higher density integration compared to conventional transistor based device.

Few year ago, carbon nanotubes have been employed as electrodes for molecular device, which can exhibit better performance than those traditional metal electrodes. That can be due to the low density states of single walled carbon nanotubes [80, 81, 82]. Sudipto *et al.* [83] created a monolayer of the magnetic organic molecule, from spin-polarized tunneling current, the results show that the higher current arises when the magnetization vector of the tip and molecules were parallel. In such spin-valve system, alignment of the molecule magnets, this can act as a valve for tunneling of spin-polarized electrons.

However, functionalized Carbon nanotubes have been modified, which can be used to enhance magnetic and transport properties of the material for spintronic based device fabrication. Recently, CNTs with side attached single-molecule magnets $TbPc_2$ was used for this purpose. It shows giant magnetoresistance (spin valve effect) up to 1000 %. Including the Coulomb blockage in the nanotubes with side attached molecular magnets [84]. Some researcher reported [85] on the strong magnetic coupling between a metallic ion and a radical spin of $TbPc_2$. Multi-terminal device made by carbon nanotubes laterally coupled to the single molecule magnet (SMM). The magnetization of a single Tb after current passing through on device. This gives extra resonances in the hysteresis loop due to a strong coupling of Tb and his radical. The inserts of Figure 2.4 gives a SEM micrograph of the sample (a), device configuration (b), spin-valve feature of the device (c), and trace measurements recorded at 20 $mT.s^{-1}$.

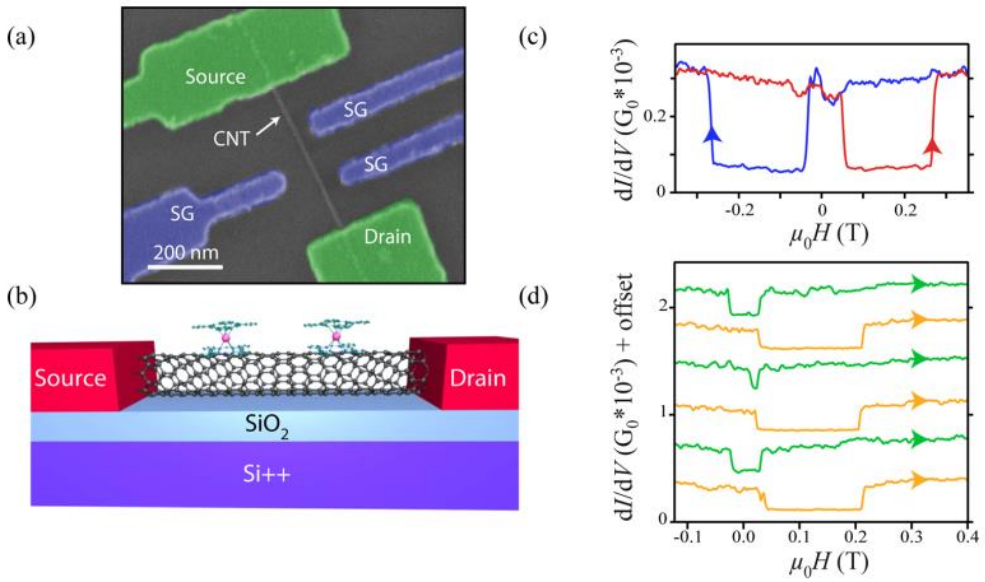

Figure 2. 4: SEM micrograph of the sample (a), device configuration (b), spin-valve feature of the device (c), and (d) trace measurements recorded at 20 mT.s^{-1} [85].

Previous experiments on $TbPc_2$ coupled to a non-suspended CNT [86] have shown that the spin relaxation was mainly enabled by bulk phonons in the environment of the individual single molecule magnets. This can only be couple to one-dimensional phonon, associated with the nanomechanical motion of the CNTs. However, this works shows strong spin-phonon coupling between a single molecule magnet and carbon nanotubes. The results predict that a coupling of this magnitude induces strong non-linearities in the mechanical motion of the CNTs [87]. That can be used to enhance the sensibility of CNTs-bases magnetometers [88, 89]. Very recently, it has been reported that functionalization method of the nanocomposite enhanced the strength of magnetic interaction, which leads to large effective moment of 15.79 μB. A spin-valve behaviors up to 8 % observed in aligned Gd-DTPA-f-MWNTs devices [14].

Few years ago, graphene layer shown its interesting properties in the spintronic application, including spin injection onto graphene, defect-induced magnetism in graphene. Moreover, investigation of spin-orbit coupling and spin relaxation mechanism in graphene could give rise to high-curie-temperature and can extend magnetic storage information for different application [90]. The theory predict spin lifetime in pristine graphene is about one micro second while experimental values

range from ten Pico to few Nano second [91, 92]. However, modification of the graphene surface layer with molecular nanomagnets reveals a significant change in term of electrical and magnetic property of the material. A. Candini *et al.* [93] reported that, in the low-temperature measurement, the magneto-conductivity signal is more than 20 % found for the spin reversal, which reveals uniaxial magnetic anisotropy of the $TbPc_2$ quantum magnets. Nanodevice made by integration of graphene, working in coulomb blockage regime, and terbium (III) central atom as shown in the Figure 2.5 below.

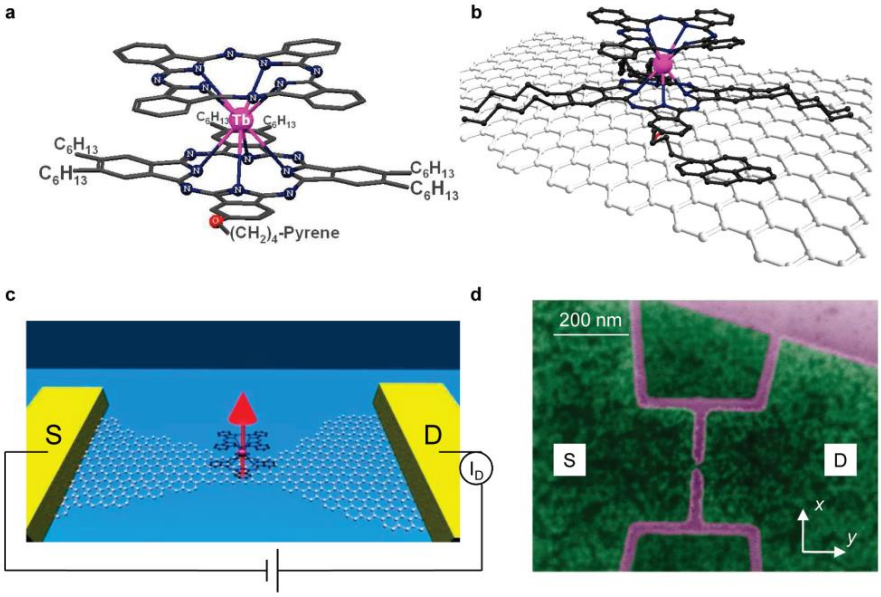

Figure 2. 5: (a) schematic diagram of the single molecule magnet, (b) attachment of single molecule magnet on the graphene sheet, (c) architecture of device with source and drain electrodes and, (d) SEM micrograph of the device [93].

2.2. Multi-walled carbon nanotubes and graphene.

The modification of the carbon nanotube or graphene can lead to a new class of molecule. This offers the spin degree that can be used to control the charge transport in conducting system. Many work have been studied related to single, double and multi-walled carbon nanotube. Most of studies were focused on the conductivity and magnetic properties of the carbon nanotubes. W. Shi *et al.* [94] reported the superconductivity of double walled carbon nanotubes, resistance was inversely proportional to temperature, and superconducting at the temperature below 6.8 K. Recently, certain project was based on the multi walled carbon nanotubes, shows the

improvement on magnetic properties when MWCNTs is attached (chelate) with gadolinium which gives large moment of 15.79 μs and non-super paramagnetic behavior governed by sufficient spin interaction [14]. A group of researcher, Martel *et al.* [95] used single and multi-walled carbon nanotubes to fabricate field effect transistors devices. Their findings report that, at room temperature, transport through nanotubes is dominated by the holes and gate voltage has shown a good conductance with SWCNTs while MWCNTs revealed no gate effect [95].

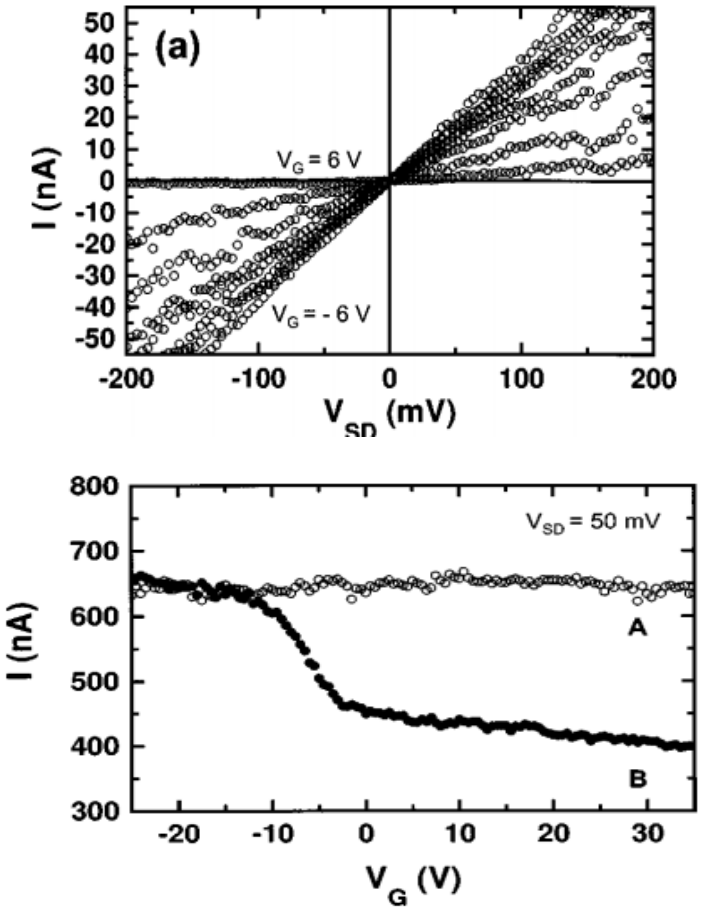

Figure 2. 6: (a). I-V_{SD} curve measured for SWCNTs device at gate voltage range from – 6V to 6V (b) I-V_G curve measured for MWCNTs device [95].

Many works have done to reinforce the dispersion of the functionalized multi-walled carbon nanotubes. Florian *et al.* [96] investigated CNT/epoxy nanocomposites and result show that large improvement on interfacial interaction between functionalized nanotube and matrix. Detachment of MWCNTs from epoxy increase interfacial shear strength from 35 to 376 MPa. [97]. In 2005, Multi-walled carbon nanotubes found a large utilization in the medicine sector. Mostly used them for drug delivery. In

addition, a work was studied the toxicity of the pristine and oxidized multi-walled carbon nanotubes. The results conclude that oxidized MWCNTs are more toxic than the pristine MWCNTs [98]. Moreover, the oxidized MWCNTs can also be used for transport purpose of biomolecule. This can easily penetrate the biological membrane of the cells. It can further reduced toxicity after being functionalized with carbonyl group [99].

Graphite is made by graphene sheets. This can be modified to extend their application. Recently, graphite has been used for graphite oxide production by improving the Hummers method. The composite $NaNO_3$ was used as oxidant reactant where $KMnO_4$ was replaced by K_2FeO_4. This shows good prospects of production and application of the graphite oxide and its derivations [66]. J. Chen *et al.* [100], synthesized graphene oxide GO by modifying the conventional method. $NaNO_3$ was not used in this process and GO synthesis has been used for waste waters post treatment purification. Nearly ten years ago [101, 102] other work focused on reducing graphene oxide using vitamin C (L-ascorbic acid). That has been used as stable suspensions of the reduced graphene oxide to obtain graphene material which has been prepared in water, with *N*, *N*-Dimethylformamide (DMF), and *N*-methyl1-2-pyrrolidone (NMP).

2.3. Magnetic susceptibility and type of magnetism

Magnetic moment is related to the magnetic susceptibility, which measure the degree of magnetization of a complex or compound when placed in an applied magnetic field. Magnetic susceptibility can also be defined as the measure of the property of the substance, showing how simple the substance can be magnetized. It originally coming from the interaction of the electron (paired or unpaired) with the nuclei when peripheral magnetic field *B* is applied. The number of unpaired electrons can be simply determined by the magnetic moment of the substance. In the complex, the magnetic moment can be estimated from the contributions of unpaired electron and their orbital. Magnetic susceptibility is expressed in term of intensity ratio of the magnetization of the materials all over applied field of the substance. It is given by the following equation;

$$\chi \simeq \frac{M}{H} \simeq \frac{\mu.M}{B} \qquad [2.3]$$

where,

$$H = \frac{B}{\mu} \qquad [2.4]$$

The symbol, χ gives the magnetic susceptibility per volume or mass of the materials used. Since, M is representing the magnetic moment per volume or mass of the materials and, H is applied magnetic field. Magnetic flux density B, is flux of the lines of force per unit of area. And μ is the magnetic permeability.

When magnetic susceptibility (χ) is negative, the material is diamagnetism, while is positive the material can be either paramagnetism or ferrimagnetism as given in Figure 2.7, including the magnetization curves of the materiel in the presence of applied magnetic field. The spins alignment observe in three different magnetic materials in the presence and absence of applied magnetic field as well.

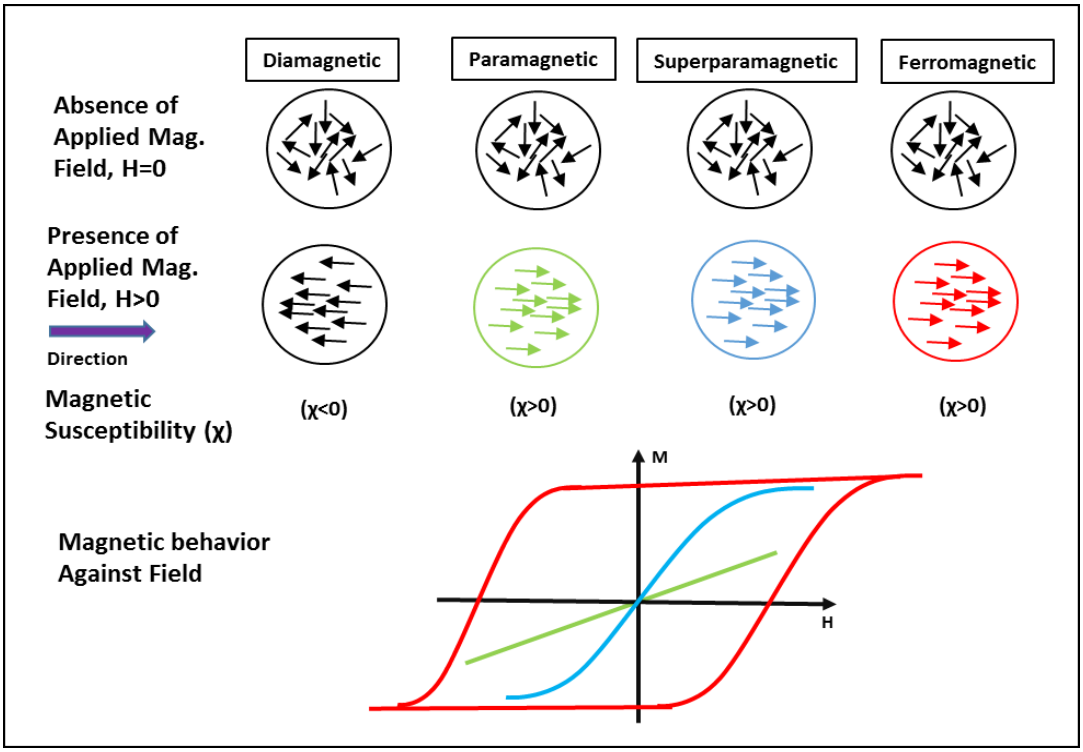

Figure 2. 7: Schematic diagram of materials in the presence and absence of applied magnetic Field.

The inverse of magnetic susceptibility is utililized to obtain the exchange interaction in the materials. This gives the long range ordering (spin) in the magnetic materials. By plotting inverse of magnetic susceptibily as function of temperature (K), the pure paramagnet with no net interaction will intercept at 0 K. For a ferromagnetic interaction the T_c is positive given by an intercep in temperature axis. For an antiferromagnetic the exchange interaction is negative given by a negative T_c (θ_P).

Relationship associates magnetic susceptibility and absolute temperature which follows by paramagnets, ferromagnets and antiferromganets material. It is usually given by Curie-Weiss law:

$$\chi = \frac{C}{T - T_C} \qquad [2.5]$$

where,

C: Constant of each materials known as Curie constant (in Kelvins, K)

T_c: Curie temperature (in K)

T: Absolute temperature, measured in Kelvins, K.

In paramagnetism, the materials are weakly attracted by peripheral applied magnetic field. The imcompletely filled atomic orbital, which have unpaired spins of the electron in the substance, are responsible of this effect. The spin of electrons are randomly oriented in the absence of applied magnetic field. Whereas the spin orientation aligned correctly in the same the direction with the applied magnetic field, occasioning in net magnetic moment as illustrates in the Figure 2.7. It is possible to observe paramagnetism behavior in the ferromagnetism materials. That can be observed above the Curie Temperature, T_c, and in antiferromagnets above the Néel temperature, $T_{N,}$ as shown in the Figure 2.8. The susceptibility curves plot against temperature.

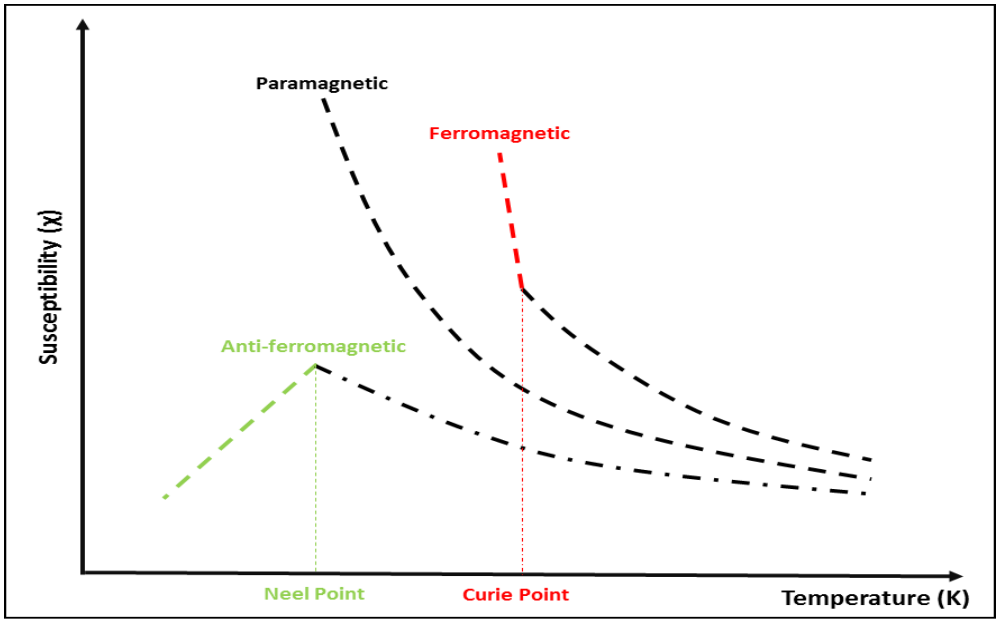

Figure 2. 8: Illutration of resulting susceptibility curves plotted as function of temperature.

This is due to the thermal energy easy overpowers the interaction energy between the spin at these temperature and phonon contrubition to the magnetic phase transition. For the paramagnets materiels, Curie-Weis law is given by:

$$\chi = \frac{C}{T} \qquad [2.6]$$

where Curie constant C, depends on the number of individual ion and effective magnetic moment, μ_{eff}. At the condition where the paramagnetic substance is non-interacting magnetic moment with angular momentum *J*. Then the Curie constant will be given by the equtation:

$$C = \frac{n}{3k_B}\mu_{eff}^2 \qquad [2.7]$$

where,

$$\mu_{eff} = g\, J \mu_B \left[J\left(J+1\right)\right]^{1/2} \qquad [2.8]$$

At the condition when the orbital angular momentum contrubition are small to the magnetic moment. μ_{eff} is given by:

$$\mu_{eff} = \mu_B \left[N_u \left(N_u + 2 \right) \right]^{1/2} \qquad [2.9]$$

where the term *n*, represents the number of atoms per unit of volume, K_B Boltzmann constant, *g*-factor which is equal to two, N_{u}: number of the unpaired electrons and, μ_B is Bohr magneton it is a constant.

Superparamagnetism is a form of magnetism exhibited by small ferromagnetic or ferrimagnetic nanoparticles. On the sizes of less than a hundred nanometers, the nanoparticles are single-domain particles, allowing the magnetization of the nanoparticles to be approximated as one giant magnetic moment by summing the individual magnetic moments of each constituent atom. This approximation is called the "macro-spin approximation." When the nanoparticles are small enough, the energy barriers separated two orientations antiparallel to each another, for magnetization reversal, which are proportional to grain volume. These energy barriers are relatively low compared to thermal energy. Under the influence of temperature, as related to thermal energy, their magnetization can flip direction randomly over short periods of time. The typical time between two flips in direction is called the Néel relaxation time. It can be calculated by the equation:

$$\tau_N = \tau_0 e^{\left(\frac{KV}{k_B T} \right)} \qquad [2.10]$$

where τ_N represents the Néel relaxation time, KV denoted the energy barier, K_B is the Boltznman constant and, τ_0 gives the time which is characteristic of the materials, its typical value is to be in the range of 10^{-9} and 10^{-10} second.

The superparamagnetic state refers to how the average magnetization of the nanoparticles averages to zero when no external magnetic field is applied, and the measurement time for the magnetization of the nanoparticles is greater than the Neel relaxation time as shown in the Figure 2.9.

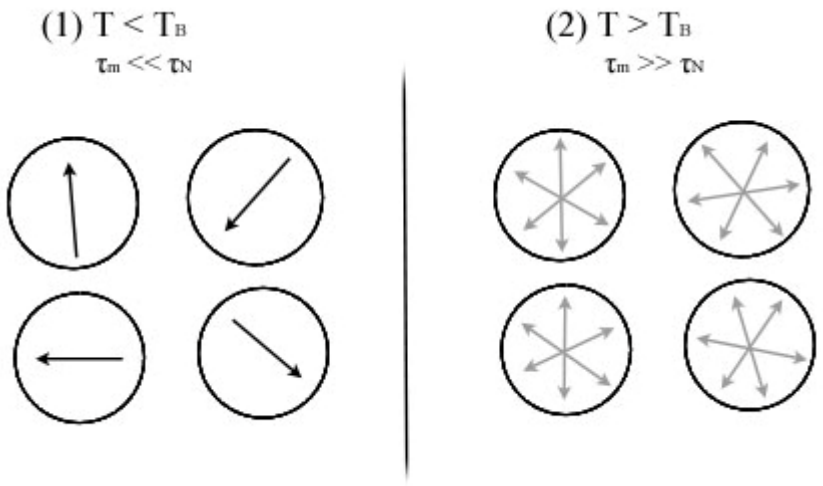

Figure 2. 9: Illustration of the blocked states (left) and superparamagnetic state

In the presence of external magnetic field, the nanoparticles are magnetized like paramagnets, but with much greater susceptibility. Ferromagnetic or ferromagnetic material can exhibit paramagnetic behaviour, the difference is that this usually occurs above the Curie temperature whereas in superparamagnets, this occurs below the Curie temperature.

It is necessary to consider a mechanism called Blocked state as illustrated in the Figure 2.9. This happen when the measured magnetization time is much lesser than Neel relaxation time. Although, the measured magnetization is just instantaneous magnetization at the beginning of the measurement because there was no flip

direction. In this state, the nanomaterials behave as normal paramagnetic but with a much higher susceptibility. Whereas the measured magnetization time is equal to Neel relation time. This situation can be defined blocking temperature as the temperature between blocked and superparamagnetic states. It is given by;

$$T_B = \frac{KV}{k_B \ln\left(\frac{\tau_m}{\tau_0}\right)} \qquad [2.11]$$

Where T_B is the blocking temperature, KV is stated as the energy barier, K_B is the Boltzman constant, τ_m is the measurement time, τ_0 is time which is characteristic of the materials, its typical value is to be in the range of 10^{-9} and 10^{-10} second.

Although certain materials are either strong or weakly attracted by the magnetic field. Other materails show opposite effect when the magneric field is applied on the materials. Diamagnetism refers to the type of magnetism whereby the materials oppose the direction of the applied magnetic field. This causing the repulsive force on the direction of a magnetic field due to neither the presence of unpaired of the electrons nor magnetic moment in the materials. The magnetic permeability of the diamagnetic materials is less than the value of permeability of vacuum, known as $4\pi.10^{-7}$ H/m. The magnetic susceptibility (χ) is negative for diamagnetic materials. In this case, the magnetic field in the materials is weakened by the induced magnetization. Illutration of the diamagnetic materials was shown in the Figure 2.7, giving the direction of the material and applied magnetic field.

2.4. Gadolinium and Diethylene Triamine Pentaacetic Acid

2.4.1. Gadolinium

The gadolinium, Gd, element belongs to the lanthanide group with atomic mass of 157.25 atomic unit (a. u). It comprises of 64 electrons distributed in four different orbitals. The last shell 4*f* contains a number of seven unpaired electrons, which plays a role of the stockage of the magnetic property of this element. The unpaired electrons with parallel spins orientation produce effective moment of 7.94 μB at the electronic ground state. It is found in the nature in oxidized form, typically as Gd^{3+}. Gadolinium is reported to be ferromagnetic below its Curie point (293.15 K) and paramagnetic above this temperature. In this work, some of advantages of using gadolinium Gd standing on two main points. It forms a stable complex with most of the organic macromolecule (ligand) and its low toxicity.

2.4.2. Diethylene Triamine Pentaacetic Acid

Diethylene Triamine Pentaacetic acid (DTPA) is a white solid powder with melting point of about 220 °C and molar mass of 393.35 atomic unit (a .u). It is always soluble (50 mg/mL) in water at 25 °C. DTPA is an aminopolycarboxylic acid comprising of diethylenetriamine along with five carboxymethyl groups. In fact, it used as chelating agent, based on higher affinity with metal cation. This can forms more stable complex compared to ethylenediaminetetraacetic acid EDTA.

In medicine, DTPA can be utilized to treat radiation poisoning, ability to form a complex with plutonium, americium and other actinides. The conjugate base of DTPA permitted Biologists to use it also as chelate for aquarium plant fertilizer. This is done by dissolving organic substances that being attached to the metal and prevent them forming large molecule through oxidation reaction. Figure 2.10 gives the chemical structure of DTPA.

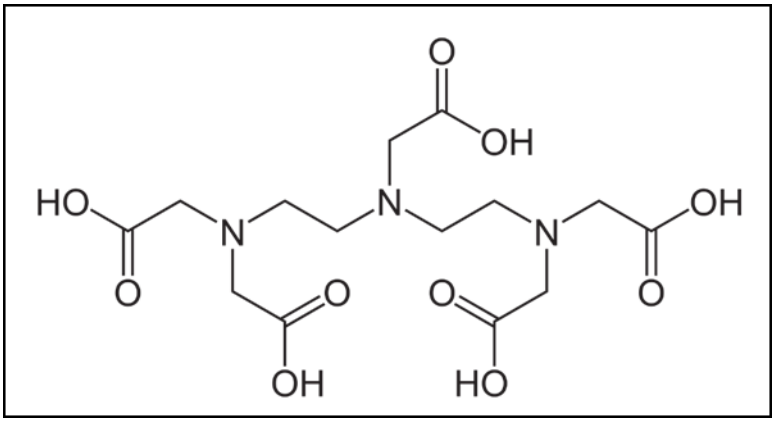

Figure 2. 10: Chemical structure of Diethylene Triamine Pentaacetic acid DTPA molecule.

2.5. Fabrication techniques of devices

The device fabrication depends on the techniques used. Certain nanoscale material for example CNTs are placed on top of the substrate while other at the bottom. They behave differently when applied at different substrate due the spin or electron interaction. The branch of physics that studies the intrinsic spin (known as single electron) and his manipulation associated with the magnetic moment is called spintronic. Nevertheless, deals only with the gathering carries charge or any movement related to the charges. However, the conversion of the charges to the spin levels in various materials serve as the key of understanding of the spin-orbital, spin polarization and the magnetization.

Carbon nanotubes can be seen as the platform of the spintronic and quantum computing application. Many spintronic devices are fabricated using either pristine or modified carbon nanotubes. MWCNTs can be attached with ferromagnetic materials to improve their properties. This kind of spintronic devices contains appreciable electronic and magnetic properties. Figure 2.11 (a) illustrate the non-suspended carbon nanotubes device with silicon dioxide substrate, spin arrangement and superconducting effect related to the spin which is fundamental key of understanding magnetic properties of the material, (b) associated spectrum plots of intensity (I) as function of voltage. Whereby straight line shows MCNTs behave as conductor while curve revealed semiconductors behavior for different probe separations.

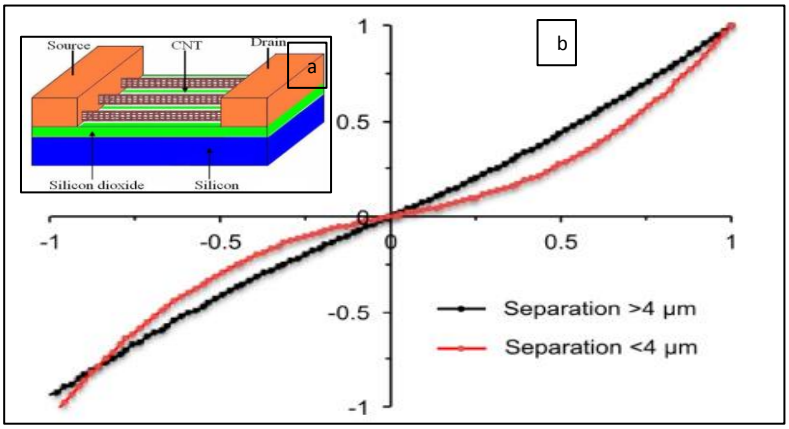

Figure 2. 11: (a) Non-suspended carbon nanotubes device [103], (b) Associated spectrum of Intensity (I) against voltage [104].

2.5.1. Di-electrophoresis

This can mainly be classifying as first method for device fabrication which is also used as a separation technique that is separation of nanotubes with different chirality. It has been shown that this method can be used for deposition and alignment of SWNT for many devices and can be used for the wafer scale fabrication of SWNT based integrated circuits [105]. Di-electrophoresis is the process whereby an electric dipole moment is induced in a particle in the presence of an electric field resulting in a di-electrophoretic force, which draws the particle into the region of highest field strength and aligns the particles in the electric field as shown in the Figure 2.12.

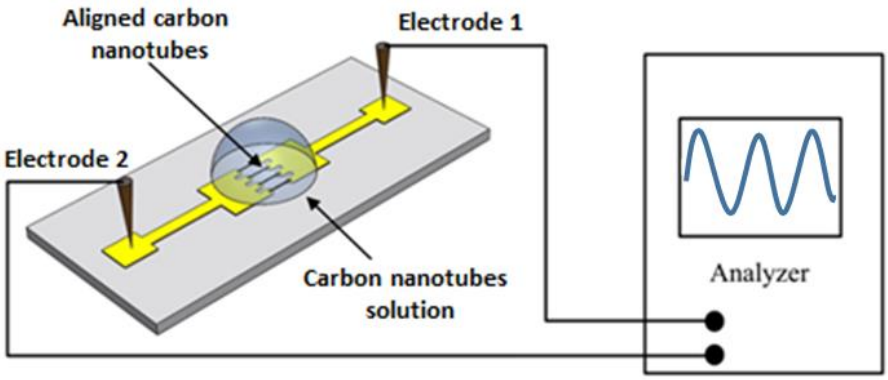

Figure 2. 12: Schematic diagram showing the electrodes and associated spectrum as appears on the oscilloscope.

Although the particles display dielectrophoresis activity in the presence of electric fields. However, the strength of the force depends strongly on the medium and particle's electrical properties, shape and size, as well as on the frequency of the electric field. This interactive force between the dipole and the non-uniform electric filed can be expressed as [106]:

$$F = \frac{\pi r^2 L}{6} \mathrm{Re}\left[f_{cm} \right] \nabla E_{rms}^2 \qquad [2.12]$$

where, the quantity $\frac{\pi r^2 L}{6}$ gives information about the volume of the nanotube called geometry factor which is associated with permittivity of the particular solvent medium. $\mathrm{Re}\left[f_{cm} \right]$ is the value related to Clausius-Mossotti factor. In addition, the quantity ∇E_{rms}^2 represents the gradient of the external electric field.

Nevertheless, fields of a particular frequency can manipulate particles with great selectivity. In CNT research, Di-electrophoresis was originally introduced as a tool to assemble and contact individual or bundled CNTs on predefined electrode structures [107]. The dielectrophoresis force is sensitive to the relative dielectric constant of particles and as semiconducting and metallic nanotubes have different dielectric constants, metallic tubes are preferentially aligned while the resulting modification in the electric field resists semiconducting tubes [108]. Figure 2.13 illustrates the situation whereby the smal drop of carbon nanotube CNT dispersed in isopropanol layed on the Si/SiO_2 substrate, allow the aligment of a carbon nanotube due to non-unioform electric field.

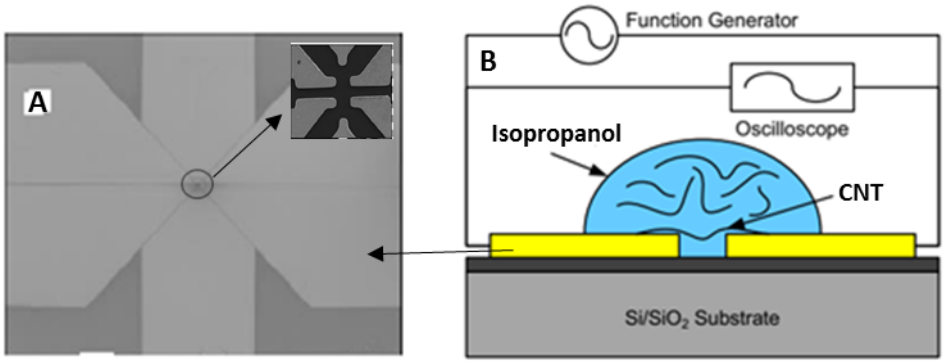

Figure 2. 13: (A) Magnified image of the pattern and (B) overview of the operation mode showing a drop of isopropanol dispersed carbon nanotubes aligned on the electrode.

2.5.2. Electron Beam Lithography

One of the usual instrument define to control the structures from nanometer level to micrometer range is electron beam lithography (EBL). In this technique, a focused electron beam is used to expose a polymer called PMMA which is sensitive to electrons. Generally, planar shape substrate is first spin coated with a PMMA dissolved in a solvent. Lastly is baked to remove by evaporation the solvent which solidifies the resist PMMA. The thickness of the film is principally controlled by the rotational speed during coating and the viscosity of the PMMA. Next step is to expose the film whereby PMMA faced a beam of electrons with an energy of 10 kV range. The steps can be arranged as follows likely demonstrated in the Figure 2.14 below.

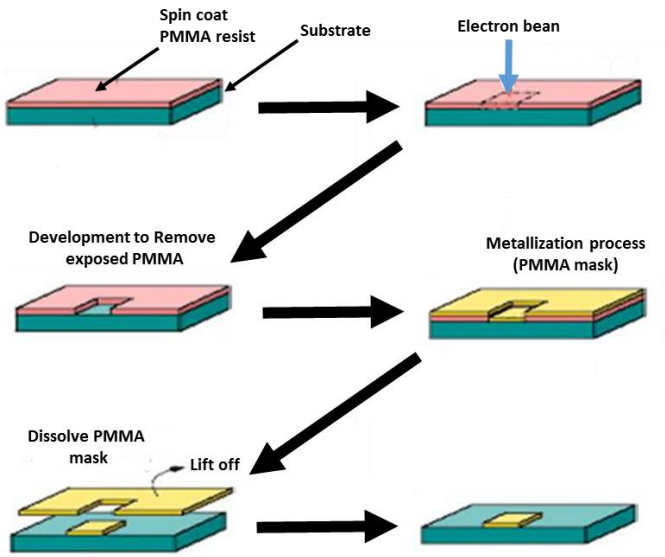

Figure 2. 14: Different steps achieved for a device fabrication by ebeam Lithography.

Due to the corresponding short electron wavelengths approximately picometer, the resolution of EBL is not limited by diff raction in contrast to photolithography where photons with a wavelength of hundreds of nanometers are used to expose the resist PMMA. As a positive resist is exposed to an electron beam, its polymer chains are cut into smaller segments while the polymers in a negative resist instead are crosslinked into longer chains. The PMMA part is exposed in a region larger than the beam size by the incident electrons, due to forward scattering and the generation of secondary electrons in the top PMMA. However, electrons that backscatter from the substrate also expose even larger region.

Forward and backward scattering and limitations in resist resolution results in a minimum feature size of around 10 nm and a minimum spacing between features of a few 10 s of nm. After exposure, the PMMA is developed in a solvent, which dissolves shorter polymer segments faster than long ones. For a positive resist PMMA, this leaves exposed parts of the substrate surface unprotected while other parts are covered with remaining resist PMMA. The remaining PMMA film can be used as a mask for etching of the underlying material, or for a lift-off process for deposited material as shown above in the Figure 2.14. According to the molecular weight, we distinguish two types of PMMA. That can be used to make a soft mask and another for hard mask, 950 and 350, respectively. It always prefer to use the soft

mask followed by the hard mask for the quality purpose of the devices. The Figure 2.15 gives typical example of the nanotube device fabrication.

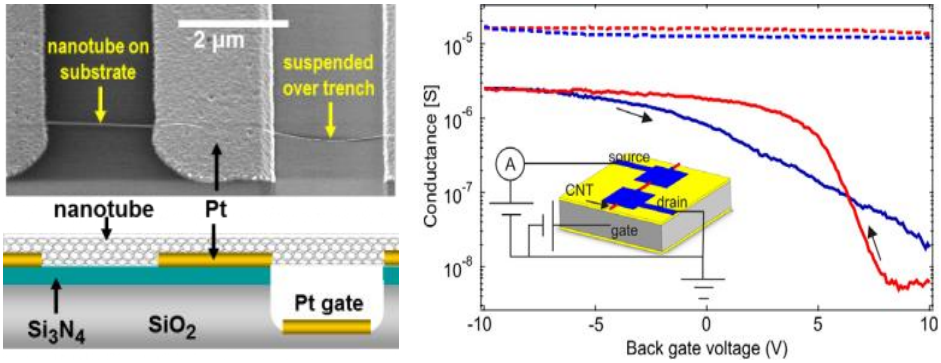

Figure 2. 15: Two typical example of the device fabricated by ebeam suspended nanotubes (left) [109] and associated with conductance vs back gate voltage (right) [110].

In effect, ebeam lithography is attached as one compartment in the Deposition vacuum chamber. This system consists to evaporate at high voltage the crucible deposit on the substrate, whereby the pattern has been made. The thickness deposits on the substrate depends on the setting of the thickness monitor. Figure 2.16 gives the image of deposition vacuum chamber with identified compartments.



Figure 2. 16: Deposition vacuum chamber as set setup at the Nano-scale transport laboratory. School of Physics, Wits University.

Chapter 3

Experimental Section

This chapter deals with the modification of carbon nanotubes, graphene oxide and how reduced graphene oxide have been done at the Nano-Scale Transport Physics Laboratory (NSTP-Lab). The first step is the chemical synthesis of Gd-DTPA and second is functionalization of MWCNTs utilizing H_2SO_4 and HNO_3 (1:3). Followed by attachment Gd-DTPA into functionalized multi-walled carbon nanotubes f-MWCNTs. The Preparation of graphite, convert them into graphene oxide and reduced graphene oxide will be known in detail in this chapter. Thereafter, this chapter will give details on the model of instruments used for different techniques such as Infra-red Fourier transform spectroscopy (FT-IR) to identify the absorption band of the chemical function, Raman spectroscopy and other techniques used for characterization of the materials under study. Finally, this chapter will deal with the projection of the material under study for device fabrication using ebeam lithography and Di-electrophoresis.

3.1. Equipment

In this project, various techniques were used such as Raman spectrometer, Fourier Transform Infra-Red, model BRUKER TENSOR 27. Inductively Coupled Plasma – Optical emission spectroscopy (ICP/OES), Zeta potential with the model Zeta Sizer nano series machine, High-Resolution transmission electron microscopy (HRTEM) to understand the morphology and structural of the materials understudy.

TESCAN microscopy to investigate the composite in the material under study. Scanning electron microscopy JEOL 7001F SEM model for morphology purpose. Electron-beam lithography compartment attached to JEOL 7001F SEM model, OLYMPUS SZX7. Di-electrophoresis (DEP), JANIS Micro-manipulated Semiconductor Device Analyzer B1500A model and High field cryogenic system were used for multi-walled carbon nanotubes devices fabrication and electronic transport characterization of the materials under study.

For the chemistry part, a designed batch reactor utilized as main equipment to obtain final products. BRANSON 1800 Sonicate machine always used disperse carbon nanotubes. Ohaus-Starter-3100 pH meter to determine neutral pH of the diluted water solution. A glass decanter for separating deposed carbon nanotube and water.

The roughing pumps mark EDWARDS used to dry the samples under vacuum by flashing nitrogen gas. Filtration unit to separate the solution. A SIGMA 2-16P Centrifuge machine used for separation purpose of the material under study. Finally, the reactions were performed under ESCO laboratory Fume hood for safety reason.

3.2. Chemical Synthesis of materials under-study

Different samples were synthesized in this project which are: magnetic sample Gd-DTPA, functionalized multi-walled carbon nanotubes, Gd-DTPA loaded into functionalized MWCNTs, graphene oxide (GO), reduced graphene oxide (rGO) and finally attached Gd-DTPA onto graphene surface of graphene oxide and reduced graphene oxide sample.

3.2.1. Gd-DTPA chelate complex

The magnetic chelate complex was synthesized using different reagents and materials. After being synthesized, the sample was purified before any characterization.

Reagents and materials

Gadolinium (III) oxide (Gd_2O_3) powder with 99.9 % trace metals, white appearance powder used was supplied by Sigma-Aldrich Company. Diethylene triamine penta acetic acid (H_5DTPA) powder 99 % pure obtained from Sigma-Aldrich Chemical Company. They were used immediately without any purification test. Isopropanol

(HPLC grade, 99,9 %) was purchased from Sigma-Adrich. Distilled water and Di-ionized water prepared at school of chemistry, Wits University.

Certain materials were used such as Hot plate mark Labotec, Silicon oil bath, Thermometer to control the chemical reaction temperature, stirred bar, ball /conical flask, condenser, and Analytical scale balance mark Pionner allows to weight reagents.

Preparation of the Gadolinium chelates

Prior to Gd-DTPA chelate synthesis, stoichiometric analysis of the chemical reaction indicates that one mole of Gd should be reacted with two moles of DTPA in forming two moles of Gd-DTPA metal complex. Hence, the amount of 14.0 mmols of Gadolinium oxide (Gd_2O_3) will react with 28.0 mmols DTPA to produce 28.0 mmols of Gd-DTPA metal complex according to the chemical reaction:

$$Gd_2O_3 + 2\ H_5(C_{14}H_{18}N_3O_{10}) \rightleftharpoons 2\ H_2[Gd(C_{14}H_{18}N_3O_{10})] + 3H_2O.$$

Gd_2O_3 of 5.0032 g was dissolved in 60 ml of deionized water that gave a white color solution. 11.0520 g of Diethylene triamine pentaacetic acid (H_5DTPA) was added to the Gd_2O_3 solution and further the mixture solution is been subjected to constant magnetic stirring at 150 rpm at 90 °C using hot plate magnetic stirrer for a period of 20 hours. Maximum dissolution of both the compounds Gd_2O_3 and DTPA was observed in the first 3 hours of the reaction when the white color solution got turned into a colorless solution. After 20 hours reaction, the solution was cooled down at room temperature. Filtration was carried out to remove any unreacted Gd_2O_3 or DTPA molecules. The filtrated solution was evaporated under fume hood for six days, where the solvent is evaporated, and white precipitates have been collected. These precipitates $H_2[Gd(C_{14}H_{18}N_3O_{10})].3(H_2O)$ white crystals are further dried under vacuum line to remove any excess water molecule present. The final white crystals are grounded to a fine powder and further been used for attaching on to CNT

surface. The inserts of Figure 3.1 illustrates the chemical structure of Gd-DTPA magnetic molecule.

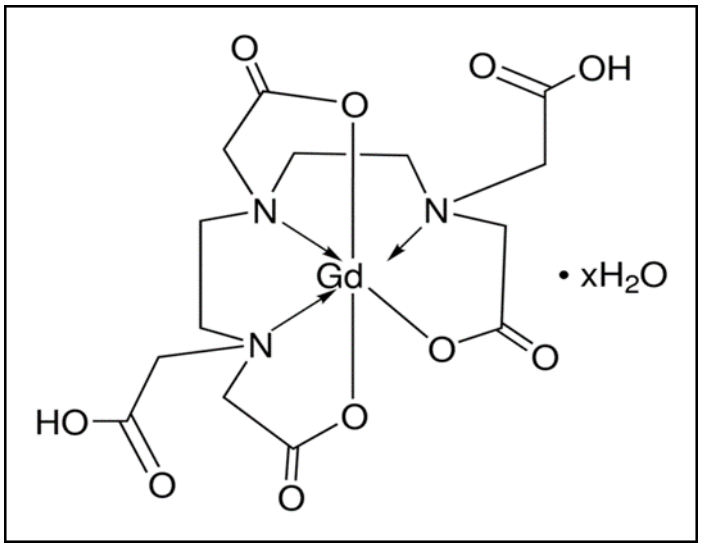

Figure 3. 1: chemical structure of diethylenetriamine pentaacetic acid gadolinium (lll) dihydrogen salt hydrate.

3.2.2. Functionalization of MWCNTs

The functionalized multi-walled carbon nanotubes were synthesized using different steps. Preparation step comprises acid treatment prior to purification of the f-MWCNTs. The samples were prepared at different temperature and refluxing reaction time as given in detail in the next section.

Drying of f-MWCNTs

This process consists to add the organic function on the multi-walled carbon nanotubes. The nitric acid and sulfuric acid mixed with a volume ratio 1:3 **[56]** , [96]. The amount of 800 mg of MWCNTs with diameter 20 - 30 nm has been added into 132 ml mixture of the acids, reflux at the range of temperature about 55 - 100 °C using silicon liquid bath. The reaction takes place within time about of 1 - 24 hours depend how good the results. In this work, four samples have been prepared at

different reaction time and temperature. Table 3.1 gives further information about the preparation condition of each samples. The last sample [f-MWCNT(100)] refluxed in a short period of one hour because CNTs got burn after a long refluxing period of 24 hours.

Table 3. 1: Preparation condition of functionalization of multi-walled carbon nanotubes.

Sample Name	Reaction Temperature (°C)	Reaction Time (Hours)	Weight Yield (%)
f-MWCNT(55)	55 ± 1.0	24	79.2 ± 0.5
f-MWCNT(60)	60 ± 1.0	24	73.4 ± 0.5
f-MWCNT(70)	70 ± 1.0	24	71.1 ± 0.5
f-MWCNT(100)	100 ± 1.0	01	63.3 ± 0.5

Although the separation process cannot be excused in this step. The mechanical method has been performed. Centrifugation followed by filtration using filter paper of about 0.22 µm. This is challenging step, used to be very crucial due to the significant losing amount the final product via water dilution.

It should be important to mention that the separation process has been done firstly by centrifuging, solution diluted with water due to acid corrosive. Therefore, solution can be centrifuged double or triple times to avoid degradation of the functionalized carbon nanotubes. Centrifuge condition of period of 40 min and 10000 rpm. Decantation of the pH neutral solution is performed after a period of 24 hours. Lastly, filtration was done under vacuum pump, final product collected and dried under vacuum with nitrogen gas at controlled pressure. Yield of the reaction has been calculated which conducted to an appreciable result of above 60 % of the final product were collected.

Figure 3.2 illustrate the schematic diagram of the functionalization process from pristine to modified multi-walled carbon nanotubes. This reaction can be represented as follow

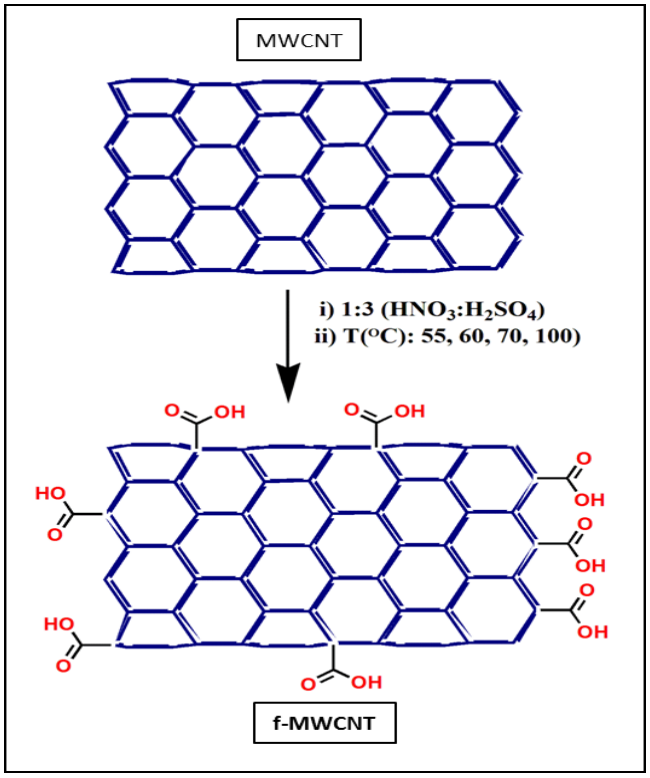

Figure 3. 2: Schematic diagram of functionalization process of multi-walled carbon nanotube at different temperatures using mixture of nitric and sulfuric acid.

Purification of f-MWCNTs

The functionalized multi-walled carbon nanotubes were purified under high vacuum line in the fume hood. Further was done by flashing the inert gas (N_2) to make sure of elimination of molecule of water in the material under study. A set-up below shows how the configuration of the high vacuum line connect to nitrogen gas trap in the Nano-scale transport physics lab, School of Physics, Wits University.

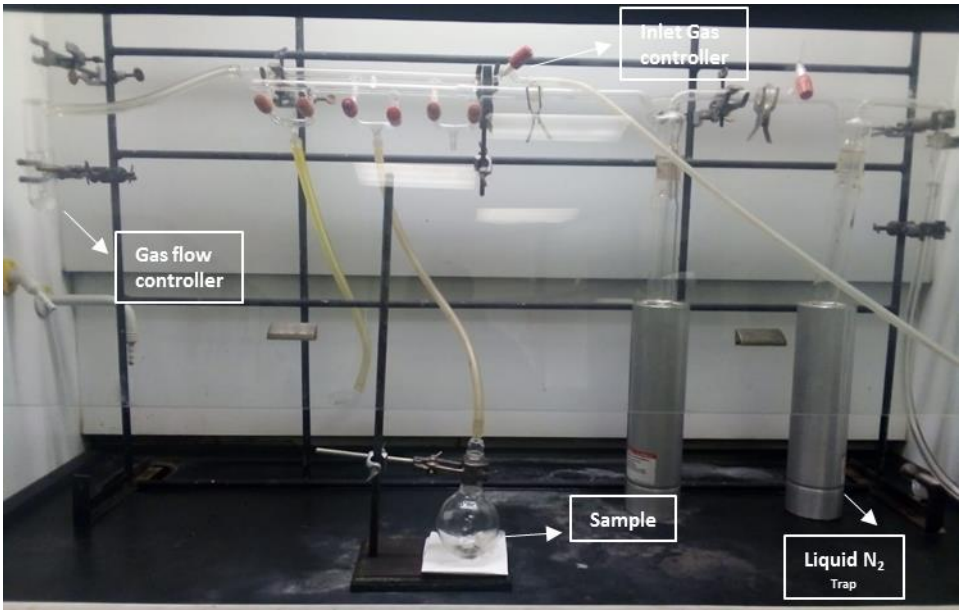

Figure 3. 3: Set-up of the Purification of the samples in the fume hood, showing Schlenk line.

In this set-up (Figure 3.3), the manipulation the valves are necessary steps need be to take care. Nitrogen gas valve should be always closed when high vacuum pump valve is opened. Gas flow rate is controlled and monitor by the compartment namely gas flow controller to avoid the disaster during the purification process. In this project, materials under study were purified in the similar way as indicates above.

3.2.3. Linkage of magnetic complex onto f-MWCNTs

Mixed each functionalized multi-walled carbon nanotubes with Gd-DTPA chelates added a volume of de-ionized (DI) water. Sonicated at 30 °C for a short period to allow good dispersion of CNTs. Stirred the suspension at the temperature at 30 °C for 24 hours. Residue wash with de-ionized water to remove impurities. This washing process was done using filtration unit connected to high vacuum pump. Dry the residue under vacuum in Nitrogen gas environment. Figure 3.3 illustrate the chemical reaction process of the gadolinium complex molecular onto the f-MWCNTs.

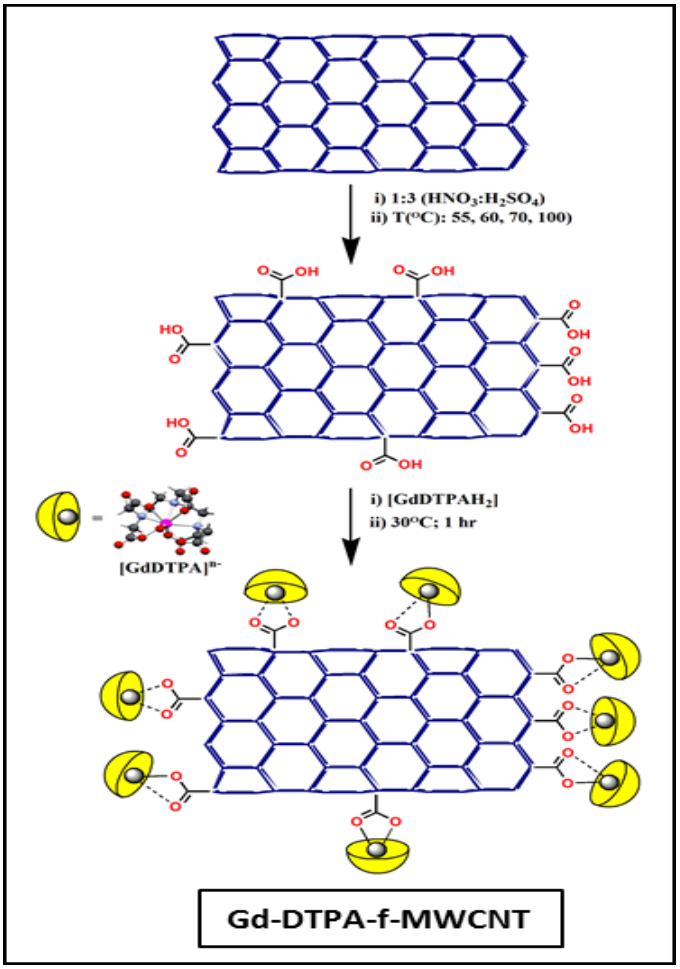

Figure 3. 4: Schematic diagram of the loading of Gd-DTPA onto of the f-MWCNTs.

The final product obtained by weight 100 mg of f-MWCNTs and 275.62 mg of Gd-DTPA mixed with 50 ml of DI water. Sonicated at 30 °C for 5 min. Suspension stirred at the temperature of 30 °C for 24 hours in a closed system. Decanted the solvent and washed the residue with a volume of 200 ml de-ionized water. Products obtained were ready to be send for structural characterization measurement. It should note that chemical reaction of pristine CNTs and Gd-DTPA was not successful due to strong carbon-carbon covalent bond on the pristine carbon nanotubes.

3.2.4. Synthesis of graphene oxide

Graphene oxide was prepared from graphite powder using modified Hummer's method [67]. The reaction was done by taking 5 g graphite and 2.5 g $NaNO_3$ added to 115 ml concentrated sulfuric acid (H_2SO_4 98 %). The mixture stirred for 30 min at room temperature. Thereafter, keeping temperature at approximately 5 °C using the ice bath. Higher temperature above 25 °C could lead to explosion.

Then 15 g potassium permanganate ($KMnO_4$) was added gradually and stirred at same time by maintaining the temperature of the mixture about 15 °C. Stirred the mixture at 35 °C for 30 min. Removed it from water bath and added 230 ml DI water progressively by keeping on stirring the mixture at room temperature. After 30 min, orange-brown color appear and raise the temperature at 98 °C for 15 min. Furthermore, 400 ml DI water and magnetic stirred the mixture for 2 hours.

Finally a solution of 50 ml hydrogen peroxide H_2O_2 30 % was gradually added to obtain a light yellow suspension. Graphene oxide solution obtained was washed with HCl 1 M to remove metal ions and DI water several time. Further, dried to obtain powder graphene oxide.

3.2.5. Linkage of Metal complex onto Graphene oxide

100 mg graphene oxide added 100 ml of DI water sonicate for 10 min for good dispersion. 4493 mg Gd-DTPA complex chelate added into the solution. The mixture stirred for 24 hours at temperature of 30 °C using bath reactor. Decantation followed by filtration of the solution. The final dried powder obtained ready for different characterization techniques. Figure 3.5 shows illustration of this chemical reaction.

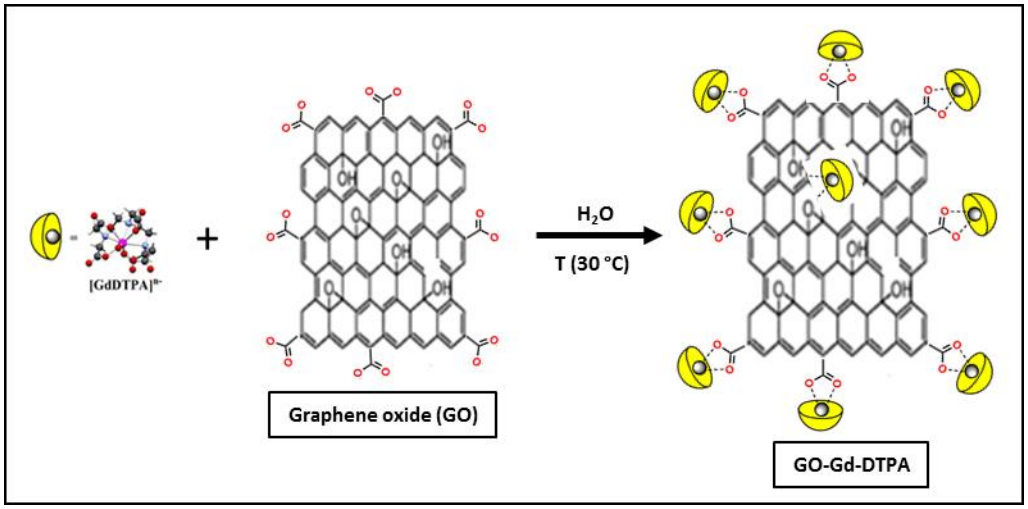

Figure 3. 5: Schematic diagram of the loading of magnetic molecular Gd-DTPA onto surface of the graphene oxide (GO).

3.2.6. Synthesis of Reduced graphene oxide and Gd-DTPA loading onto rGO

The low solubility of the synthetically reduced graphene oxide (rGO) sheets in water and most natural solvents. It is related to low percentage of organic function in this material. The substance used to convert GO was hydrazine or hydrazine hydrate. Although, hydrazine or hydrazine hydrate are profoundly harmful and explosive [111]. The safety measures must be taken when huge amounts of hydrazine or on the other hand hydrazine hydrate are utilized. Thus, another methodology for adequately changing over GO into stable reduced graphene sheets under gentle conditions should be explored [112, 113]. In this work, we used ascorbic acid to convert graphene oxide into reduced graphene oxide due to the reason mentioned above. L-Ascorbic acid (L-AA), having a mild reductive ability and nontoxic property, is naturally employed as a reducing agent in living things, [114, 115] and has also been used as a primary reductant in the laboratory [116, 117].

Ascorbic acid (L-AA) was used to convert chemically graphene oxide into reduced graphene sheet. Because of its good mild reductive ability and non-toxique property compared to Hydrazine (N_2H_4). The reduction of the GO using L-AA was realized in water at room temperature. 0.52 g of GO dispersed in 60 ml of DI water. Sonicates the solution during 10 min at the temperature of 23 °C. Added 5.2 g of L-AA in the aqueous dispersion solution of the GO. Vigorous stirring at the temperature of 23 °C

at different time of 6, 9 and 12 hours. Reduced graphene oxide solution obtained were filtrated and dried under high vacuum line. The reduction progress was monitored by UV-vis spectroscopy.

Only the rGO samples which was obtained after 12 hours reduced time was used to react with the load Gd-DTPA. In the typical experiment, Gd-DTPA was loaded onto rGO (12 hours) by taking 25 mg reduced graphene oxide added 10 ml of DI water sonicate for 20 min for good dispersion. 10.7 mg Gd-DTPA complex chelate added into the solution. The mixture stirred for 24 hours at temperature of 32 °C using bath reactor. Filtrate the solution and wash with DI water. The final dried powder obtained ready for different characterization techniques.

3.3. Characterization techniques

After sample preparation, the final dried products were submitted to different techniques for characterization. Scanning Electron Microscopy and High Resolution Transmission Electron Microscopy were done to monitor the morphology of the material under study. Fourier Transform Infra-Red was performed to obtain absorption band. Follows by Raman spectroscopy to identify changes in the material. Zeta Potential Analysis was used to check whether functionalization of the CNTs was successful. TESCAN microscopy to investigate the composite in the material under study. Inductively Coupled Plasma Optical-Emission Spectrometry (ICP-OES) was utilized to get the percentage of gadolinium on the pristine and each of Gd-DTPA-f-MWCNTs samples.

3.3.1. Scanning Electron Microscopy

Field Emission Scanning Electron Microscope (FE-SEM) was used to observe the morphology of the materials understudy at different magnification. The JEOL SEM 7001F shown in Figure 3.6 used for imaging of fabricated devices. It goes together with a gas infusion structure with platinum, tungsten and Teos (Tetraethyl orthosilicate) sources. This is just like a nanomanipulator machine utilizing four distinct buttons who can be controlled in the *x, y* and *z* way. The SEM can likewise

be utilized for E-beam lithography designing utilizing RAITH programming for creation of devices. For accurate manipulation of this system. It is appreciable to pump down to a vacuum of 5.0 x 10^{-9} Pa. The increasing accelerating voltage can go up to 30 kV. There is a chamber extension used to screen the example stacking and the stage position. Figure 3.6 gives JEOL SEM 7001F machine, indicating the main component associated with it. The movement of loading and removing sample is visualized on the extension chamber screen 1.

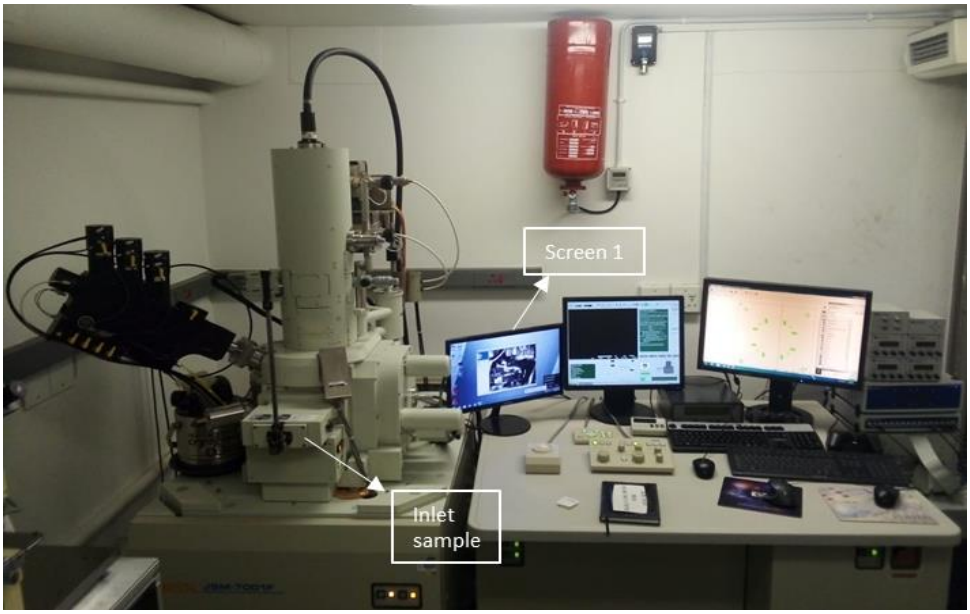

Figure 3. 6: SEM machine connected with electron beam lithography at the NSTP Laboratory, Wits University.

3.3.2. TESCAN microscope

This system combines the Time Of flight Secondary ion mass spectrometry TOF-SIMS and FIB-SEM. It used to determine the elemental composition and gives the molecular information in the material. Generally, the TOF-SIMS uses a focused pulsed particle beam (gallium or Cesium source gun) to remove the chemical species on the surface of the material. The removed particles are then accelerated in a flight tube where their mass is determine by the time at which they reach the detector. Although the mass determination in a TOF analyzer is based on the measurement of a flight time requiring a defined start time. Ion guns (Ga^{+}) for use in TOF analyzers

therefore must be pulsed. Figure 3.7 show a schematic diagram of the operation mode of the TOF-SIMS. The ion beam from the gun makes an angle of 55 degree with the electron beam, interact with targets and the intensity of the fragment is measured as function of mass ion-charge ratio (m/Q).

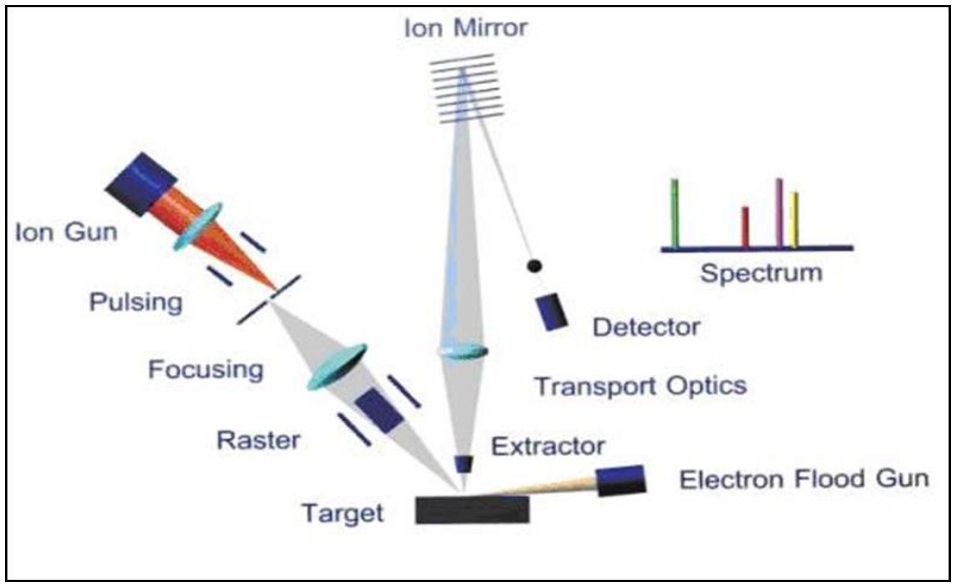

Figure 3. 7: Schematic diagram of TOF-SIMS instrument.

In this work, LYRA3 FIB-SEM model was used with TOFWERK detector to measure the time of flight of the fragmented ions. This system contains lateral resolution of < 50 nm and the depth resolution < 3 nm. It has the detection limit of < ppm for Gallium and 1.5 ppm for xenon. Regarding the mass resolution, this is system can reach an amount of 3500 atomic mass units (amu). Figure 3.8 illustration of LYRA3 FIB-SEM system as indicating the TOF-SIMS analyzer and the measurement set-up of the system.

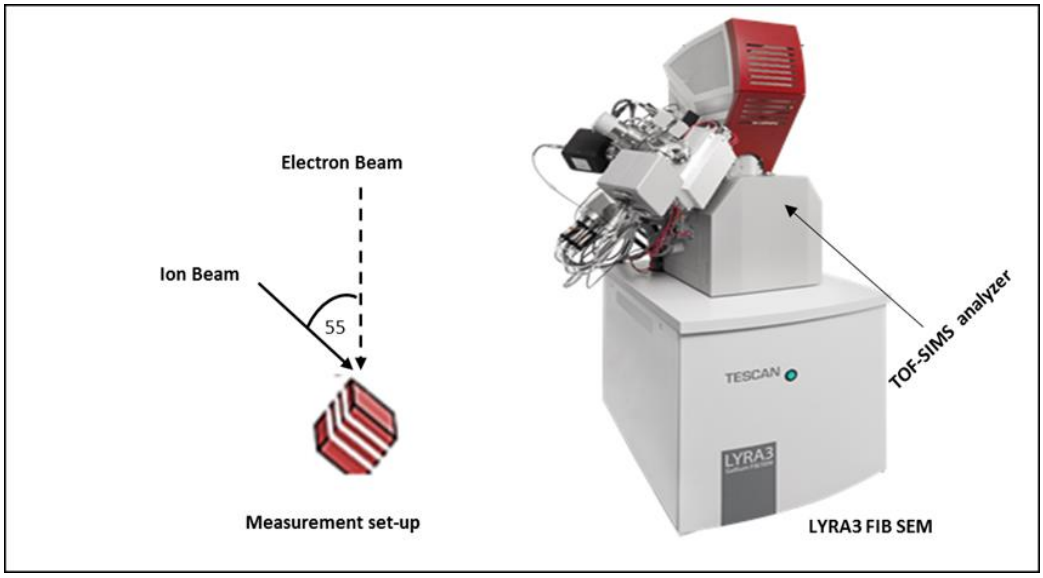

Figure 3. 8: LYRA3 FIB SEM associated with TOF-SIMS compartment.

The TOF-SIMS is applied in many industrial laboratories for elemental and molecular surface characterization. it presents some advantages such as; detection of the trace and light elements, the presence of isotopes in the material can be distinguish, both two positive and negative ion, lateral distribution of the species in the surface of the material and 3D chemical mapping with Depth profiling. This measurement was done with our Collaborators ‘‘***Central Demo Lab & Application. Material Science unit Facility Russia***’’.

3.3.3. Fourier Transform Infra-Red spectrometer

Fourier Transform Infrared (FT-IR) spectra of the samples were collected using (Bruker tensor 27 FT-IR & OPUS data collection program) spectrometer in the range from 400 cm^{-1} to 4000 cm^{-1}. It is equipped with a room temperature detector. The background was generally collected in air before running of single channel. FT-IR spectra were collected with maximum resolution of 15 cm^{-1}. Figure 3.9 shows the FT-IR spectrometer used.



Figure 3. 9: Bruker Tensor 27 FT-IR spectrometer used in this project.

3.3.4. Raman Spectroscopy

This technique is based on Raman Effect, consists of measuring a frequency shift of the light scattered by a sample exposed to monochromatic illumination. It is appropriated to all type of samples regardless of its form (liquid, solid or gas). Raman spectroscopy is powerful technique which affords reliable information on the crystalline quality of the samples by giving the state of stress of the material, its purity as well as the presence of impurities or graphitic phases.

Raman spectra are generally studied in stokes and anti-stokes line region which are obtained by measuring the intensity of the Raman scattering as a function of the wavenumber. In the Raman spectrum, each band can be characterized by its intensity and full width at half maximum. The intensity depends in particular on the density of elements and the Raman scattering cross-section of the studied structure. The cross-sections vary between the different structures. The full width at half maximum or the broadening of the peak provides information on the disorder in the structure. The position of band called Raman Shift in the spectrum is related to the natural frequency of a mode of vibration E_{2g} and A_{1g}. The *G* band is credited to in-plane vibrations from E_{2g} modes and the *D* band to out-of-plane vibrations from A_{1g} modes. In this thesis, two Raman spectra were acquired to each sample to estimate experimental error. The analysis of our samples was performed at the Microscopy and Microanalysis Unit,

University of the Witwatersrand. Raman spectrometer model Jobin Yvon T64000 was used to obtain the structural information of the materials under study.

3.3.5. Zeta potential

The electrophoretic measurements were carry out with a zeta potential analyzer (Zeta sizer Nano series model). This measurement is based on the charge of the particle disperse in the solvent. The zeta potential of the prepared materials was obtained at pH 7 by dissolve in water. Graphene oxide and f-MWCNTs were negatively charged by deprotonation of the carboxylic acid produced during the oxidation reaction. Figure 3.10 shows the picture of Zeta potential analyzer used, indicating the inlet sample at the bottom of the picture.



Figure 3. 10: Photograph of Zeta potential analyzer (Zeta sizer Nano series model) used.

3.4. Device fabrication

The device fabrication was done using DEP to align CNTs samples. Electronic transport measurement was done on the cryogenic high Field measurement system on the Gd-DTPA-f-MWCNTs, Gd-DPTA-GO and Gd-DTPA-rGO (12 hours) magnetic samples. Magnetization and susceptibility studies of the composite were carried out at room temperature using an ultra-sensitive superconducting quantum interference device MPMS-SQUID magnetometer from Quantum Design, San

Diego. The susceptibility was measured at zero field cooled (ZFC) and field cooled (FC) conditions. In ZFC the sample is cooled without any applied magnetic field to the desired temperature. For FC curves, sample cooled with an applied magnetic field to the chosen temperature.

3.4.1 Di-Electrophoresis

DEP system shown in Figure 3.11 is used to align the carbon nanotubes samples. This was done by suppling a frequency of 1 MHz on the system. The average voltage through the oscilloscope set at 5 Vpp. The peak to peak voltage was set at 1 V/div and controlled by the oscilloscope. In this set-up, one metallic pin electrode connected to output of the function generator while another is in input (CH 2) of the digital oscilloscope.

Few milligram of f-MWCNTs samples dispersed in 2-propanol solvent. A small drop of bundles Gd-DTPA-f-MWCNTs layed between the pins metallic electrodes. This allows the carbon nanotubes samples to be align between the two pin electrodes. The good alignment of the CNTs can be monitor on the trace of the oscilloscope. Figure 3.11 gives the set-up of DEP alignment station used for the fabrication CNTs devices.

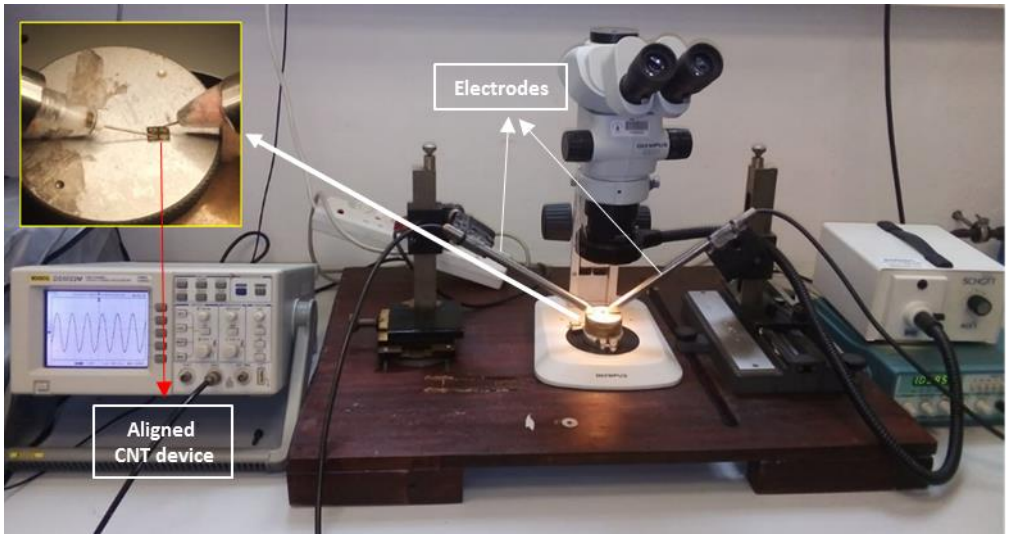

Figure 3. 11: Di-electrophoresis station at NSTP Laboratory, Wits University.

3.4.2. Semiconductor device testing Machine

The semiconductor device analyzer (Agilent technologies B1500A model) associated with PNA Network analyzer is used to test devices. It comprises of a two-terminal configuration with SMU connected to source and drain and one from ground. This system works at room temperature. While can be also cooled down to reach 77 K if liquid nitrogen is used. The testing of CNTs aligned device can be consider as last step before proceeding to wire bonding. The photograph of the Janis micro-manipulated probe station is shown in the Figure 3.12. Two probes in contact with the Silicon substrate represented at the bottom the picture.

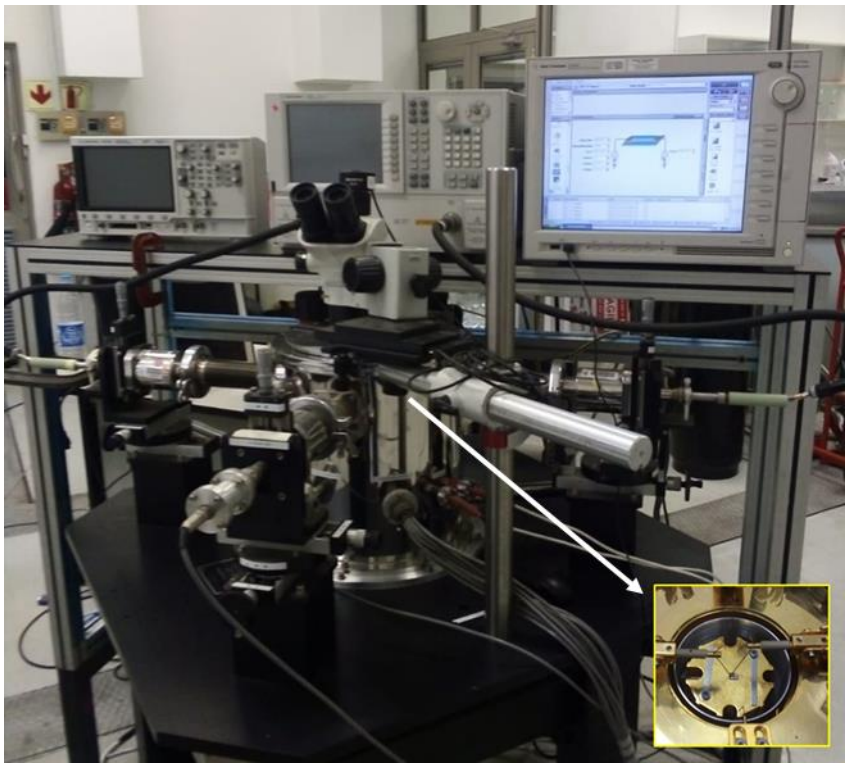

Figure 3. 12: Janis micro manipulated semiconductor analyzer testing machine.

3.4.3. Cryogenic high field measurement system

The cryogenic high field measurement system shown in Figure 3:13 is a state of the art facility used for low temperature electronic transport measurements as well as vibrating sample magnetometer (VSM) capability. It consists of a closed helium condensation cycle controlled by a compressor that is used to cool a variable temperature insert (VTI) to 40 K in the first stage then further cooling through a pot to 4 K.

The sample is systematically inserted into the VTI chamber using a special sample holder after a series of evacuation procedures to ensure that the cryogenic system is not contaminated. The sampler holder is a probe, two are available one that cools directly to 2 K when the VTI is at its base temperature and a second one that cools to 300 mK through a pot (reservoir) of He3 connected to the top of the sample holder which undergoes a cooling cycle through the sorption pumps.

The device is connected to the sample holder using wire bonding from the device's prefabricated electrodes to the sample holder contact pads. The sample holder consists of 6 contact pads with electrical connections to the long sample holder rod which is used to insert the sample into the VTI. The sample chamber is evacuated and flushed with helium gas before inserting the sample.

A manually operated gate valve separates the VTI and sample chamber. The VTI pressure is controlled by a needle valve and controlled to ensure stability of the temperature during measurement. For this system, the VTI pressure is set to seven mbar during normal operation.

Before operation, the system is warmed up to room temperature to prepare for evacuation. The VTI is evacuated for 24 hours with the needle valve opened to full capacity to remove any contaminations. Then the He insert is also evacuated for 12 hours. The dump (which is a cylinder that stores the He for closed loop circulation during operation) is emptied and refilled to the required level with He^{4+} gas and connected through the He^{4+} insert. Then the compressor is switched on to circulate the He to cool the VTI, and the rest of the system to the recommended temperatures. The VTI must cool to a temperature of approximately 170 K. When the first stage

and second stage reach 40 K and 4 K the Helium from the dump condenses into a pot and forces the VTI to cool further to a base temperature of 2 K.

The sample is connected to the measuring instruments through an electronic black box with different lines corresponding to how the device is wired. A Keithley 2400 is used as a source meter and a Keithly 2182A is used as a nano-voltmeter along with Stanford Research model SR830 DSP lock in amplifiers. Lakeshore temperature controllers are used to monitor the temperature in various parts of the instrument namely; VTI, sample stage, 1st stage, 2nd stage, inner magnet, outer magnet, He pot, magnet switch, sorption pumps. The magnet is controlled by a Cryogenic Ltd magnetic power supply.



Figure 3. 13: Image of the Cryogenic high field system at NSTP laboratory, School of Physics, Wits University.

Chapter 4

Results and Discussions on the Multi-walled Carbon nanotubes

This chapter will focused on the analysis and interpretation of data obtained from several techniques. The materials under study are divided into two categories: (1) Multi-walled carbon nanotubes, which contains functionalized multi-walled carbon nanotubes, (2) Stoichiometry loading Gd-DTPA magnetic molecular onto functionalized multi-walled carbon nanotubes f-MWCNTs. It will also highlight on different characterization techniques applied on the multi-walled carbon nanotubes and Gd-DPTA modified carbon nanotubes samples. Results obtained from these different measurements were performed at the room temperature with exception of the magnetic measurement.

4.1. Functionalized Multi-walled Carbon Nanotubes

This segment will discuss the characterization of the following techniques: Fourier Transform Infra-Red spectroscopy; Raman spectroscopy, Scanning Electron Microscopy, Zeta potential, Acid-base titration and *IV*-characterization using functionalized carbon nanotubes material under study.

4.1.1. FT-IR spectroscopy

The functionalization of MWCNTs was carried out at different conditions. 100 °C for 1 hour, 70 °C for 24 hours, 60 °C for 24 hours, and 55 °C for 24 hours. FT-IR data of these samples were measured at room temperature. The samples were crashed to thin powder and not prepared with KBr matrix pellets.

The results from FT-IR show that absorption bond of –COOH group is assigned at the peak seating in 1720 cm^{-1} wavenumber. Therefore, pristine MWCNT does not show any peak at this wavenumber, which is in agreement with the result reported by D. Bikiaris *et al.* [118]. A weak peak is observed in MWNTs spectra at 1153 cm^{-1} wavelength is related to lower percent of C-O bonds. Peaks at 2860 and 2960 cm^{-1} are due to C-H stretching bonds. The peaks observed in functionalized MWNTs spectra at 1100 and 1600 cm^{-1} related to C-O and –COO-, respectively. It mentioned that the peaks, which appeared in the region of 3100 – 3600 cm^{-1} assigned to O-H hydroxyl and carboxylic acid group. The f-MWCNT(100) sample indicates a largest band in this range compared to other functionalized carbon nanotubes. This can also played a role of site attachment of the magnetic molecular Gd-DTPA.

Moreover, hydroxyl and carboxylic peaks are due to chemical oxidation of nanotubes by H_2SO_4 + HNO_3 acid mixture. FT-IR spectra of different functionalized multi walled carbon nanotube obtained at different reaction time are shown in Figure.4.1. The large change can be observed in FT-IR spectra of functionalized multi-walled carbon nanotubes (f-MWCNTs), compared to pristine multi-walled carbon nanotubes. Which is resulting from new organic group that have been successfully introduced onto multi-walled carbon nanotubes.

The inserts of Figure 4.1 gives FT-IR spectra of functionalized MWCNTs at different temperature of 55 °C (24h), 60 °C (24h), 70 °C (24h) and 100 °C (1h) with different reaction time. The typical characteristic peaks of the new groups are indicated with their specific wavenumber on top-right side in the Figure 4.1. The confirmation of this modification onto the surface of carbon nanotubes was further characterized by Raman spectroscopy.

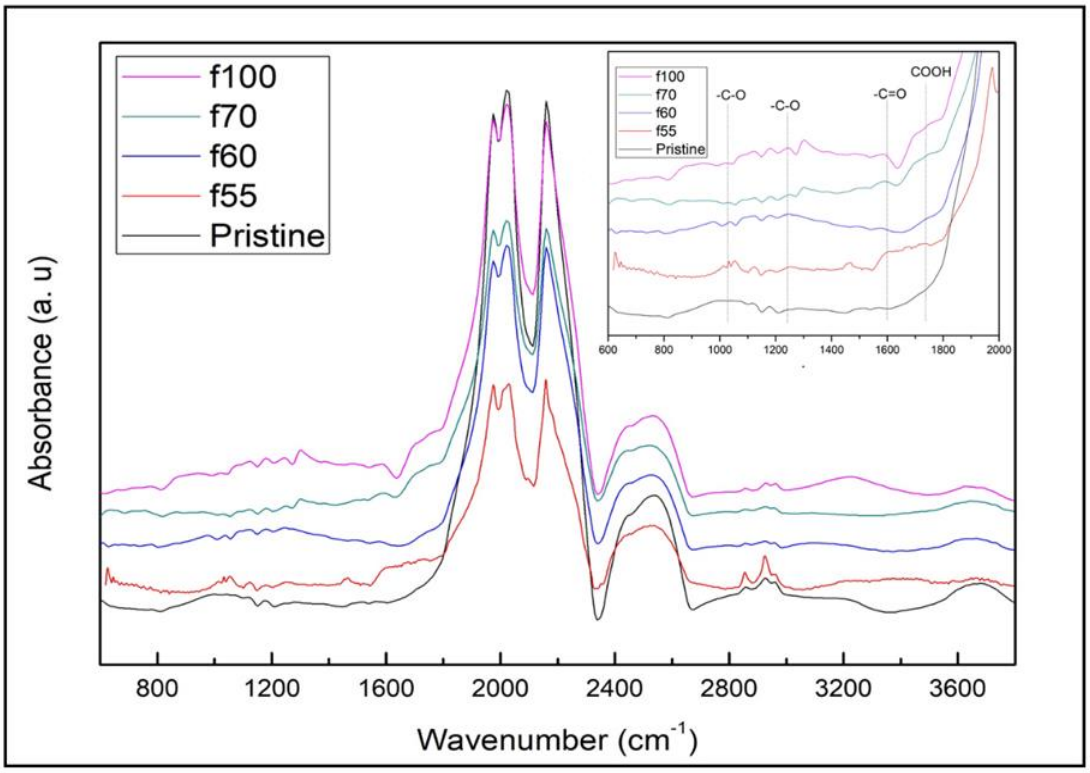

Figure 4. 1: FT-IR spectra of pristine and functionalized multi-walled carbon nanotubes at different temperature and reaction time.

4.1.2. Raman spectroscopy

Typical Raman spectra of pristine sample and f-MWCNTs samples was obtained using a 514 nm excitation laser. The technique used in order to evaluate quantitatively the functionalization degree of the samples. That is important to identify the disorder arising from covalent functionalization, related to the transformation of sp^2 aromatic carbon into sp^3 carbon. Furthermore, this determination of the level of disorder in sp^2 carbon can be always analyzed in term of the ratio of the I_D/I_G phonon peaks. The graphitic crystallite sized between Raman active defects (La) in the materials is directly calculated using the Tuinstra Koenig relation [119] where C(λ) is approximately equal to 4.4 nm, it is a constant that depends on the excitation energy for a particular wavenumber. The equation is given by:

$$\frac{I_D}{I_G} = \frac{C(\lambda)}{L_a} \qquad [4.1]$$

It was discovered that the functionalized carbon nanotubes at 55, 60, 70 and 100 °C have crystallite sizes of 3.70, 3.49, 3.64 and 3.42 nm, respectively.

The Raman spectroscopy results show that *D* and *G* bands estimate at the Raman shift position of 1340 and 1570 cm^{-1}, respectively. That is almost similar for all functionalized carbon nanotubes. This explain that the natural structure carbon nanotubes have not being destroyed. In fact, it is necessary to notice that the existence of irregularities in the structure results in a very weak *D* band at near 1350 cm^{-1} [120]. The *D* band is consider as manifestation of the disorder or defect band, its peak intensity has been measured directly proportional to the level of the defect in the material under study. While the *G* band is credited to in-plane vibrations from E_{2g} modes and the *D* band to out-of-plane vibrations from A_{1g} modes [121]. The 2*D* band is the second order of the *D* band and is alluded to as its suggestion. It results from a two-phonon lattice cross section vibrational procedure.

Although, one of the main effect observed in the functionalized carbon nanotubes is the broadening of the *D* and *G* bands. This is due to the formation of the shoulder peaks that correspond to nanoscale Raman active sites along the tubes. Therefore, the higher value of width broadening of the *D* and *G* bands observed f-MWCNTs at 55 degrees indicated a large modification onto the surface of multi-walled carbon nanotubes compared to pristine and others functionalized carbon nanotubes sample. This can be further supported by deconvolution of the Raman spectra. The inserts of the Figure 4.2 show Raman data collected of the resulting f-MWCNTs which were prepared at various temperature compared with the pristine CNTs.

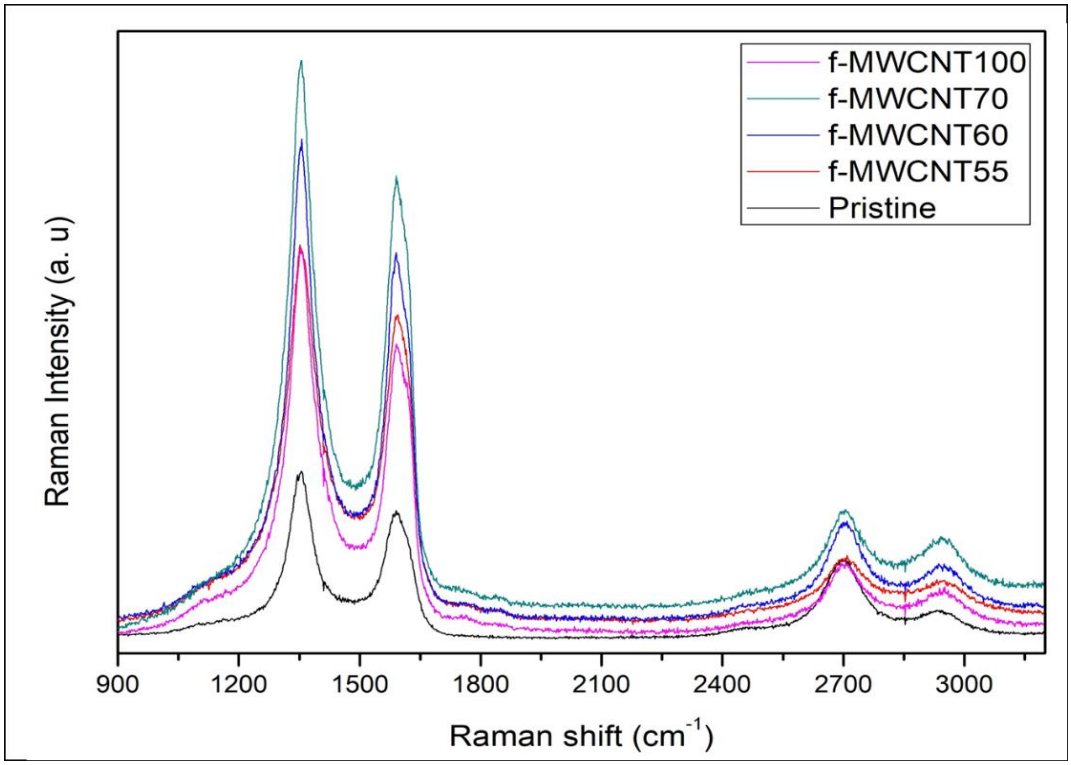

Figure 4. 2: Raman patterns of pristine multi-walled carbon nanotubes in comparison of f-MWCNTs taken at from 900-3200 cm^{-1}. The spectral patterns displayed two broad features in first order 1000 – 2000 cm^{-1}. And asymmetric feature in the second order spectra (2000 – 3400 cm^{-1})

It is seen that the relative height of the *D* and *G* bands were not constant. The heights of the f-MWCNTs are sufficiently different from the pristine, usually the covalent functionalization is related to the expansion of the *D* band intensity. It can be seen, there is broadening of the band in the functionalized materials. Moreover, the chemical functionalized samples can be supported by the intensity ratio I_D/I_G, further indicating rupture of sp^2 bond carbon atom to form sp^3 hybridized which justified the surface modification of CNTs. In addition, functionalized CNTs at 55 °C and 70 °C are significantly surface modified as can be seen in the spectra (Figure. 4.2). This reinforced by titration acid-base result, and FT-IR spectra of 55 °C and 70 °C functionalized CNTs. Those FT-IR spectra indicate similar features, which is resulting from surface modification of CNTs compared to pristine. The absorption peaks in the range of 2500 – 3200 cm^{-1} can be assigned to carbon with sp^3 hybridization.

Recent work [122] show that the analysis of disordered of materials by Raman spectroscopy is based on the splitting of the main Raman features. More than the five-peak model proposed by Sadezky *et al*. [123] has become popular curve fittings for graphitized carbonaceous materials, including MWCNTs. The latter model consists of the use of two very broad bands, with minor modulations, near 1200 and 1500 cm^{-1}, in addition to the *D*, *G* and D_0 bands [124].

The deconvolution strategy shows that each pattern base feature of the spectrum was fitted with a multi-peak system using Lorentzian and Gaussian peak. Pristine sample was fitted with nine peaks and functionalized samples resulting more than ten peaks, which resulting from greater concentration of carboxylic group in the sample, governed by the reaction condition. The control of temperature and time played major role in the chemical functionalization process. It has been shown that deconvolution method of Raman spectra to estimate the effect of mild oxidative reflux technique. This deconvolution model considered in the *D* and *G* bands region. In the *D* band region, a central *D* band and two sub-bands designed Dl (representing *D* left side) and Dr (representing *D* right side). A single side *S* band was reflected at the left side of the spectra. In the G band region, two bands namely Gl and Gr surrounded the central G band. The deconvolution of Raman spectra of each sample is shown separately shown in the next page. While fitting band is considered of the combination of Lorentzian and Gaussian bands.

The breaking of aromaticity upon chemical functionalization leads to the formation of smaller sp^2 domains that are confined by sp^3 bonds and with dimensions comparable to polycyclic aromatic hydrocarbon molecules. The covalent functionalization can also introduce polyene-like structures. Raman studies of polycyclic aromatic hydrocarbons (PAH's) showed bands at near 1250 and/or 1400 cm^{-1} , with deviations in the Raman peak position and relative intensity depending on the molecular size and symmetry, as well as, one peak at around 1600 cm^{-1} [120, 125]. Moreover, the Raman spectra of polyacetylene show two features at 1200 and 1500 cm^{-1} [126]. Thus, fitting bands Dl, Dr and Gr in the present deconvolution model were assigned to the presence of low size aromatic domains, analogous structures to PAH's, [120, 125] while S and Gl bands are identified to fingerprints of polyacetylene

like structures [126]. Furthermore, the Raman spectra of fullerenes show a base feature at approximately 1500 cm^{-1}, thus the Gl band can also have contributions from tube-end vibrations closes multi-walled CNTs. In the case of the highly functionalized material, the deconvolution required a band Gv (G valley) at near 1480 cm^{-1} in order to obtain an accurate curve-fitting.

The pristine carbon nanotubes was fitted with three Lorentzian bands and six Gaussian bands in the entire deconvolution Raman spectrum. The following bands in the first order of the pristine such as one Lorentzian S, one Lorentzian Dr, and Gaussian Gv are represented in the Raman shift at the position 1197.8 cm^{-1}, 1367.1 cm^{-1}, and 1531.3 cm^{-1}, respectively. However, in order to obtain a better fitting of the cumulative fit peak, the specific Gv band (standing for G valley) is required on the Raman shift of 1531.3 cm^{-1} between the *D* and *G* bands. The intensity ratio I_D/I_G was found to be equal to 1.304 ± 0.002. In the second order, the presence of DS, 2D, DG and 2G band resulting from the addition of *D* band and addition of *D* with average the G + Gv bands.

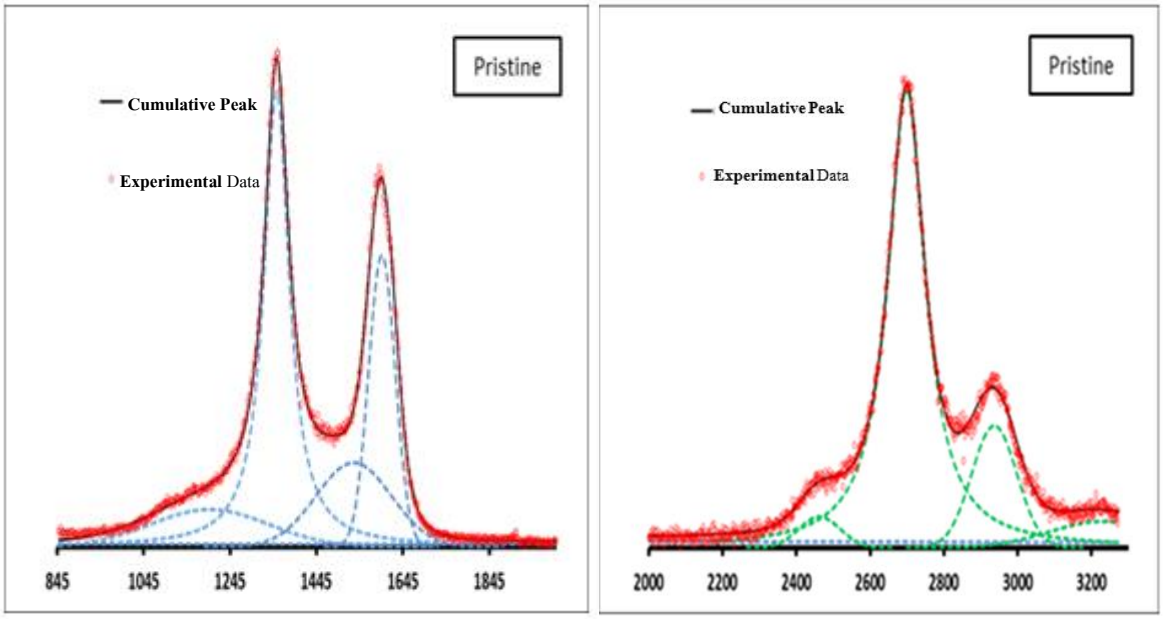

Figure 4. 3: Deconvolution model applied on Raman spectrum of pristine. First order shown between the values of 845 cm^{-1} - 1900 cm^{-1} and second order in the range of 2000 to 3300 cm^{-1}.

In the functionalized multi-walled carbon nanotubes samples, the material namely f-MWCNT (55) was fitting with a total number of 13 peaks in the range of 845 – 3200 cm^{-1}. Five Lorentzian bands and eight Gaussian bands as it can be seen in the Figure 4.4. The following bands S, Dl, Dr, Gl and Gr in the first order are appeared in the Raman shift of 1122.5 cm^{-1}, 1208.5 cm^{-1}, 1359.7 cm^{-1}, 1540.7 cm^{-1}, and 1613.5 cm^{-1}, respectively. It is noticeable that the Raman shift of S band decreases with 75 cm^{-1} while Dr band decreases with a value of 7.5 cm^{-1} in comparison of the pristine. The intensity ratio $I_{D/G}$ was found equal to 1.191 ± 0.003 which was lesser than 1.304 ± 0.002 value $I_{D/G}$ of pristine carbon nanotubes. More peaks required in the first order to obtain a better fitting of the cumulative fit peak. This is due to broadening of Raman patterns of this sample. In comparison with the pristine sample. The percentage area of *D* band decreases in 4 % with the increases in 5 % area of *G* band. This model is in accordance with Castiglioni *et al.* [120] that pointed out the first order region of the Raman spectra of any ‘‘graphitic’’ carbon sp^2 system as two categories of bands. These two Categories of bands relay to the convolution of Raman transitions from domains of similar type but having different shapes and sizes. This multiplicity explains the broadening effect [124, 127].

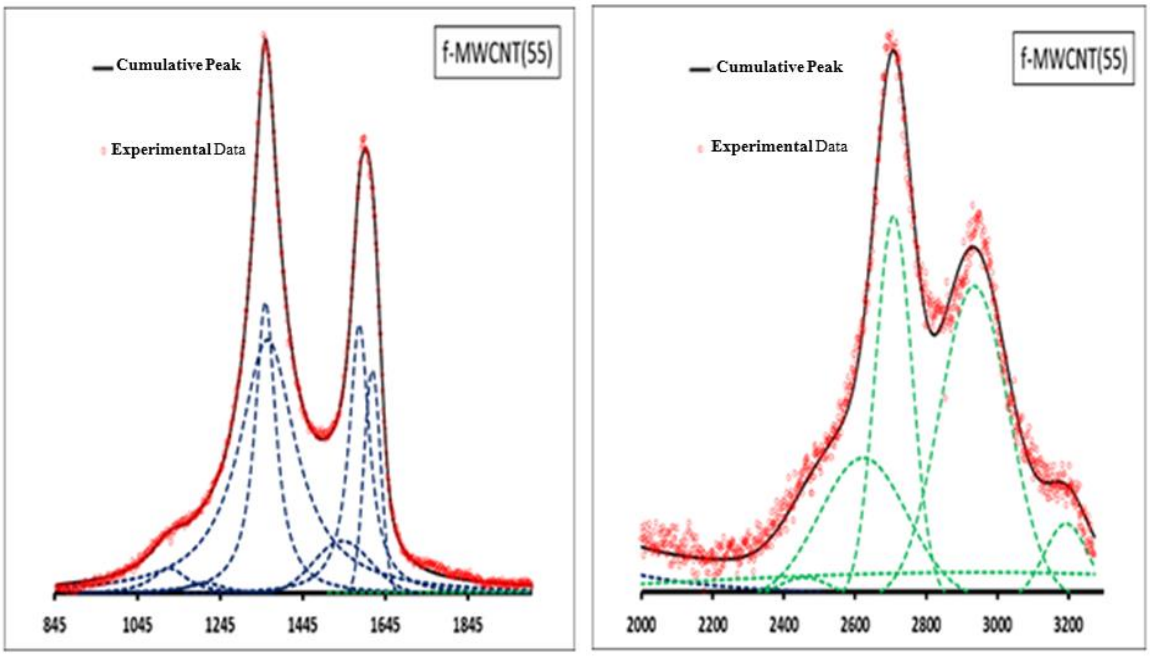

Figure 4. 4: Curve fitting of f-MWCNT(55) material. Showing two main region of the Raman spectrum. First order shown between the values of 845 cm^{-1} - 1900 cm^{-1} and second order in the range of 2000 to 3300 cm^{-1}.

In the second order region, several new bands were added in the central *D* band. Raman shift position of those additional bands correlate with the composite values found in the first order of the Raman spectrum. However, these bands can be represented mathematically as follows: D+S(DS), D+DI(DDI), D+D(2D), D+G(DG), D+Gr(2G), and D band plus the average of G and Gr, matches the value of the position DG band.

Regarding the multi-walled carbon nanotubes refluxed at 60 °C material. The deconvolution fitting was done using a total number of 12 peaks in the entire spectrum. While Six Lorentzian bands and seven Gaussian bands fitted correctly this Raman spectrum. The satellite bands S, Dl, Dr, Gl and Gr in the first order were acted in the position of the wavenumber of 1121.9 cm^{-1}, 1258.4 cm^{-1}, 1370.9 cm^{-1}, 1536.6 cm^{-1}, and 1620.0 cm^{-1}, respectively. The slight changes in those bands position compare to f-MWCNT(55) resulting to different concentration of carbonyl or hydroxyl group in the materials. The obtained intensity ratio $I_{D/G} = 1.262 \pm 0.003$ which was found slightly similar to pristine. While this value increases compared to functionalized multi-walled carbon nanotube [f-MWCNT(55)]. Moreover, the similarity in term of intensity peak will be justify the concentration of the carboxylic group in f-MWCNT(60) which closest to pristine CNT.

In the second order region, new bands were added in the central *D* band similar to f-MWCNT(60). Raman shift position of those additional bands correlate with the composite values found in the first order of the Raman spectrum. However, these bands can be represented mathematically as follows: D+S(DS), D+DI(DDI), D+D(2D), D+G(DG), D+Gr(2G), and D band plus the average of G and Gr, matches the value of the position DG band. Figure 4.5 gives deconvolution pattern of this materials indicated the fitted band DS at the position 2486.8 cm^{-1}, DDI (2566.6 cm^{-1}), 2D (2702.3 cm^{-1}), DG (2934.9 cm^{-1}), DG (2977.8 cm^{-1}) band obtained with the average of G and Gr, and 2G (3188.6 cm^{-1}). In comparison with the f-MWCNT(55) sample. The percentage area of *D* band increases in 8 % with the decreases in 4 % area of *G* band. A significant changes can also be observed in

comparison of pristine sample with deceases of approximately 13 cm^{-1} in the Dr band of f-MWCNT(55).

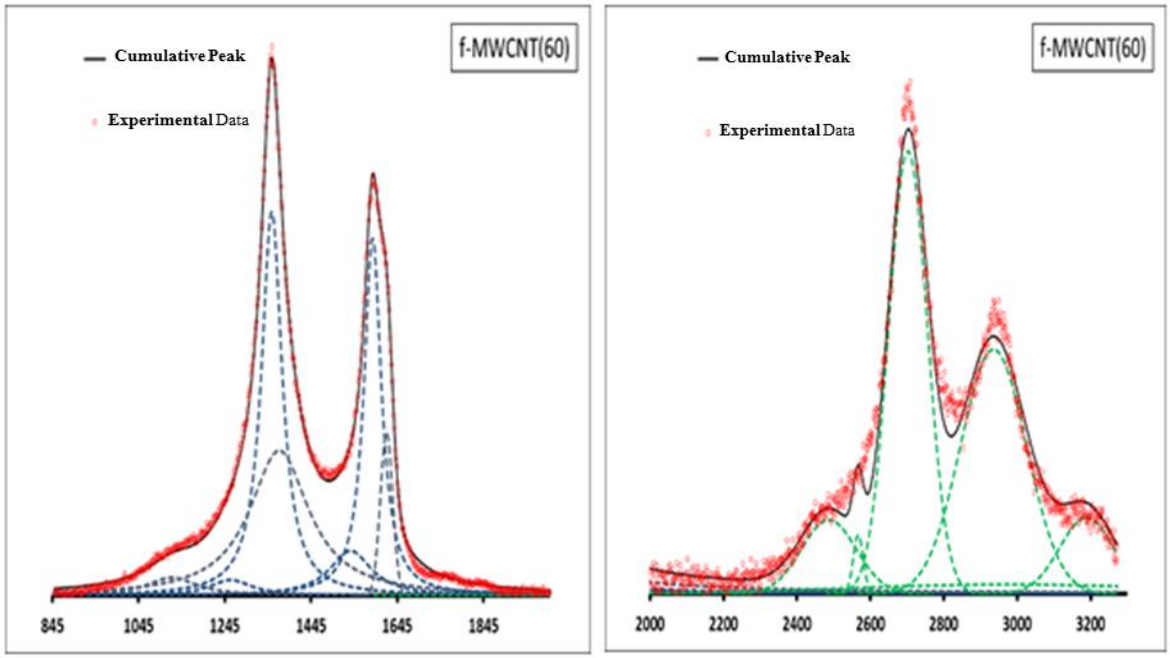

Figure 4. 5: Curve fitting of f-MWCNT(60) material. Showing two main region of the Raman spectrum. First order shown between the values of 845 cm^{-1} - 1900 cm^{-1} and second order in the range of 2000 to 3300 cm^{-1}.

Instead, the Raman spectrum of f-MWCNT(70) material in the Figure 4.6 shows a total number of 12 peaks to fit the entire spectrum. It was remarkable that the DG band disappeared to obtain the accurate fitting. This can be considered as decrease in concentration of the carbonyl and hydroxyl group in the materials. This was in accordance with the result reported by Susana *et al*. [122]. which stated that increases in the satellite band confirming higher chemical functionalization. The satellite band of this sample behaves differently compared to f-MWCNT(55) as will be explaining in details in Figure 4.9. However, it was found that intensity ratio $I_{D/G} = 1.210 \pm 0.002$ which estimated slightly similar to f-MWCNT(55) material. This value decreases compared to functionalized multi-walled carbon nanotube [f-MWCNT(60)]. In this instance, the expectation of disorder assume to be higher in this sample compared to pristine and functionalized carbon nanotube [f-MWCNT(60)]. This was confirmed by the percentage area of *D* and *G* bands, increases in 12 % and 7 % consecutively.

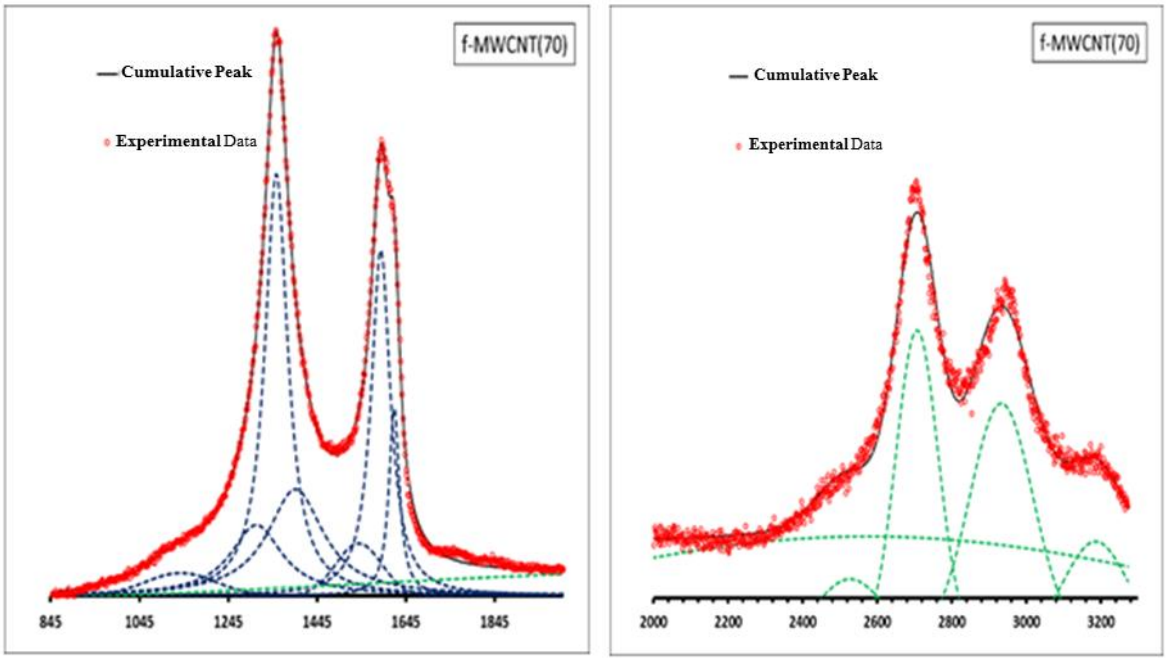

Figure 4. 6: Curve fitting of f-MWCNT(70) material. Showing two main region of the Raman spectrum. First order shown between the values of 845 cm^{-1} - 1900 cm^{-1} and second order in the range of 2000 to 3300 cm^{-1}.

The inserts of the Figure 4.7, provides Raman spectrum of functionalized multi-walled carbon nanotubes samples oxidized with a mixture of acid at 100 °C for 1 hour. This Raman spectrum was fitted with a total number of 12 peaks similar to the f-MWCNT(70). Five Lorentzian bands and seven Gaussian bands. However, the following bands S, Dl, Dr, Gl and Gr in the first order are appeared in the Raman shift of 1112.8 cm^{-1}, 1329.6 cm^{-1}, 1380.5 cm^{-1}, 1566.7 cm^{-1}, and 1613.5 cm^{-1}, respectively. It is obvious that the huge changes in the spectral features can be observed in the first and second order. The intensity ratio $I_{D/G} = 1.291 \pm 0.003$ closely identical to the value obtained of pristine and f-MWCNT(60) sample. This was confirmed by the percentage area of *D* and *G* bands, increases in 6 % and 4 % consecutively. A significant changes happen in the second order in the band. Moreover, this changes confirmed most ruptures on that structure due to chemical functionalization (functional groups and sp^3 carbon) and the domination of hydroxyl group compared to carboxylic group at reaction temperature range of 100 °C. That can be quantified by acid-base titration of the carboxylic group in the sample which is given in details in the next section.

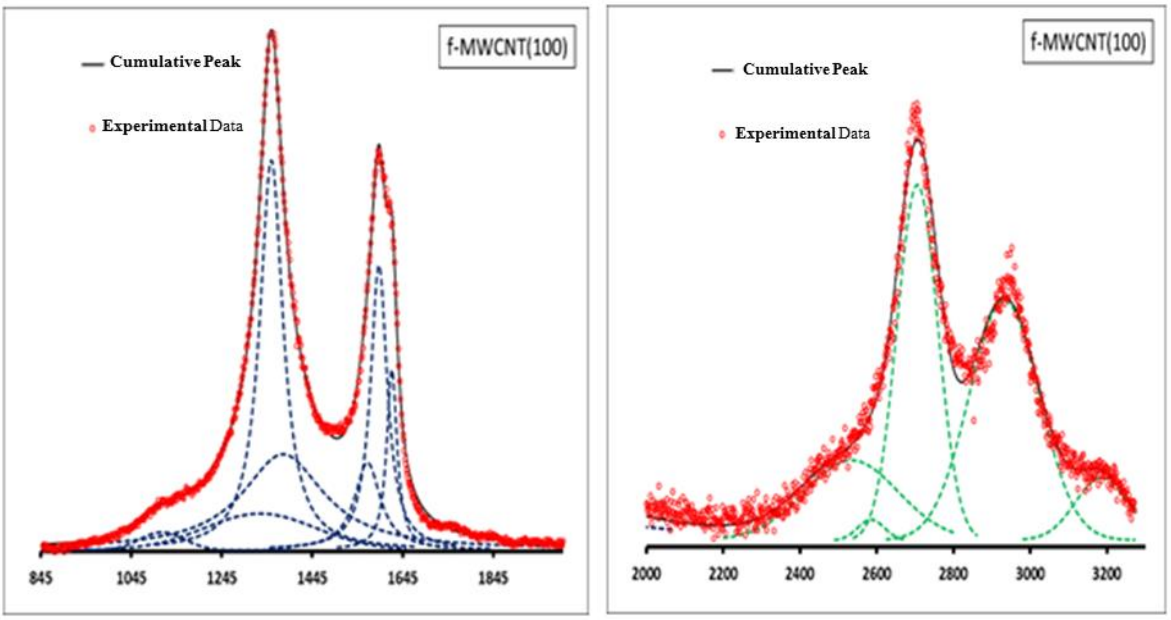

Figure 4. 7: Curve fitting of f-MWCNT(100) material. Showing two main region of the Raman spectrum. First order shown between the values of 845 cm^{-1} - 1900 cm^{-1} and second order in the range of 2000 to 3300 cm^{-1}.

Generally, the intensity ratio I_D/I_G also offered useful information conventionally used to indicate disorder in the samples. Figure 4.8 gives the intensity ratio I_D/I_G phonon peaks plotted as function of temperature of the reaction.

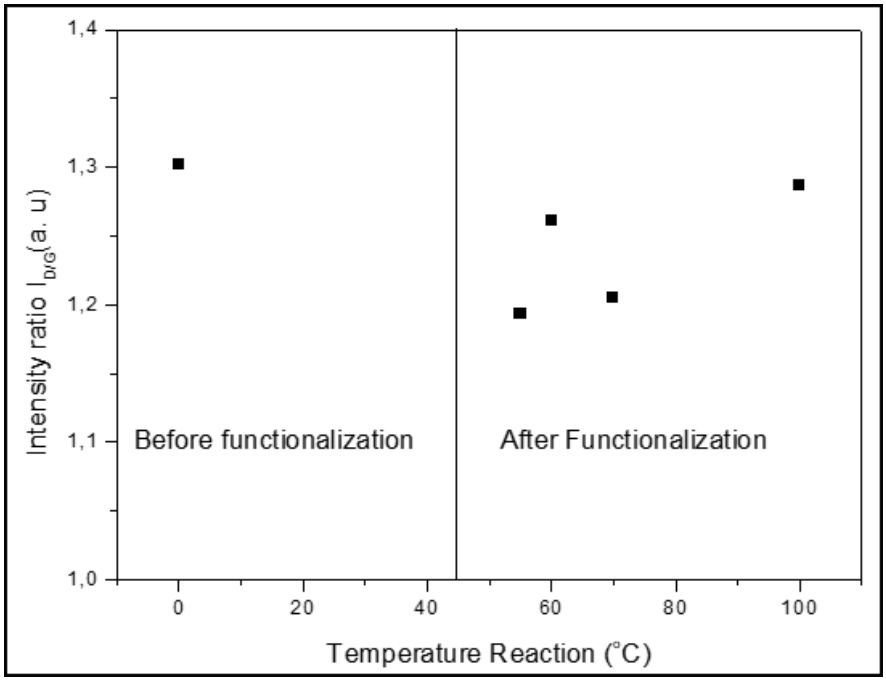

Figure 4. 8: Intensity ratio I_D/I_G as Function of reaction temperature. This was taken before chemical reaction (Pristine) and after chemical functionalization of the material under study revealed by the Raman spectroscopy.

It was found that for SWCNTs [128], the degree of covalent functionalization has been efficiently quantified by the ratio of the band intensity I_D/I_G. This can also be applied in the case of covalent functionalization the multi-walled carbon nanotubes as intensity ratio I_D/I_G changes. Many works report an increase of I_D/I_G ratio after oxidation of the materials. This was in contradiction with the result found by certain researchers [129, 130] who reported that intensity ratio I_D/I_G is not obvious changed with covalent functionalized multi-walled carbon nanotubes. However, this idea can be extended by evaluating the changes in the intensity of the bands in the first and second order of the spectrum.

The inserts of Figure 4.9 is showing the intensity trends major band obtained for oxidation of the carbon nanotubes compared with the pristine CNTs. This can be used as the follow-up of covalent functionalization against the refluxed reaction temperature.

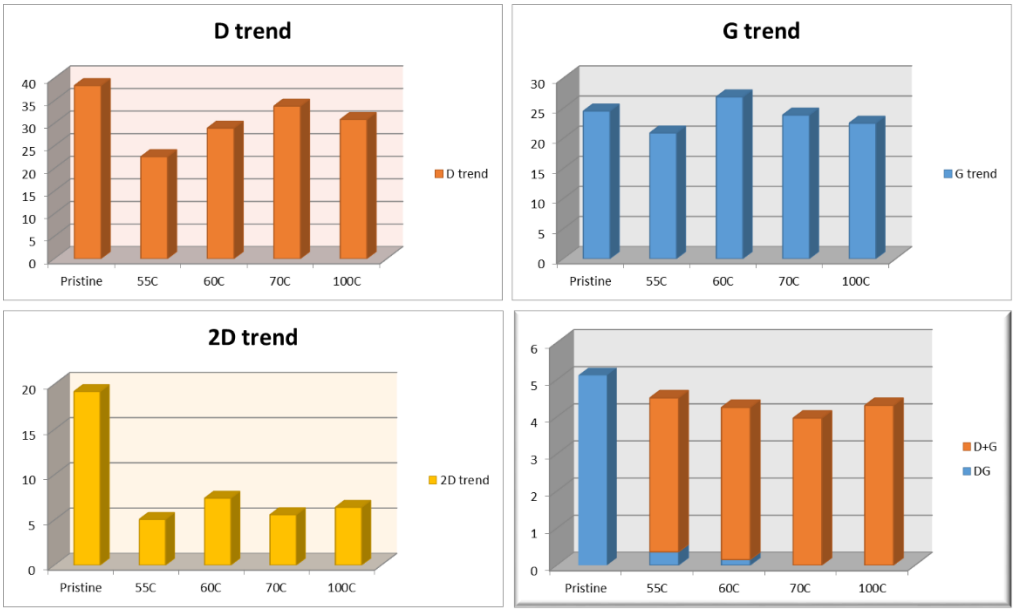

Figure 4. 9: Histogram plotted of intensity of D, 2D, G band as function of reaction temperature. f-MWCNTs are compared in term of the intensity trend of D, 2D, G bands. The strong change in the D and G band is responsible of the chemical functionalization of the carbon nanotubes.

The information above shows a correlation between the degree of functionalization and the effect of Raman spectrum in the samples. Therefore, to quantify the observed spectral broadening and their correlation with the chemical functionalization degree (CFD). It was important to build up a suitable deconvoluted pattern. The plotting of the sum of the area of the sub-bands/sum of D and Gl band multiply by 100 to quantify the chemical functionalization degree of the materials under study.

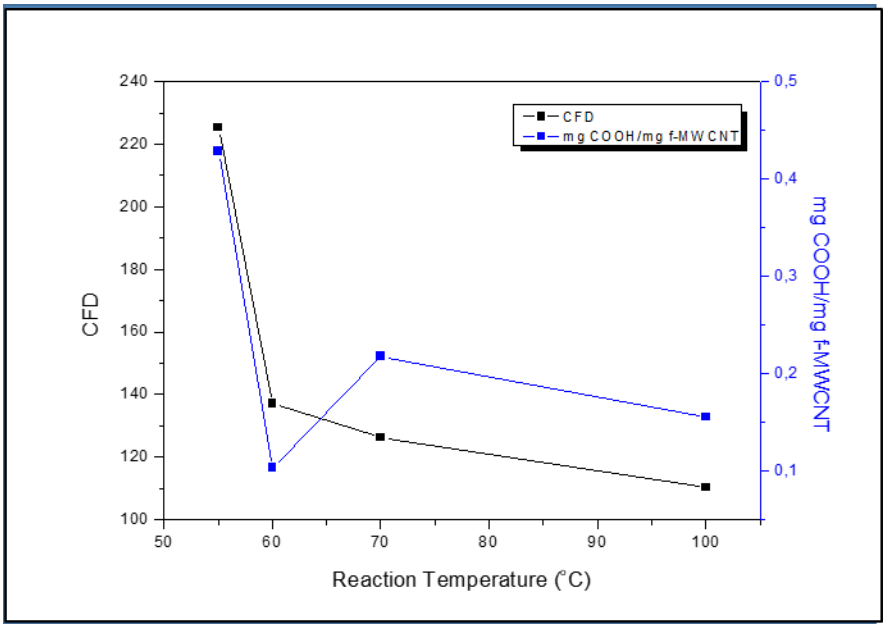

Figure 4. 10: Plot of the chemical functionalization degree (CFD) obtained by Raman spectroscopy [Raman CFD = Sum [rel. area (S, Dl, Dr, Gv, Gl, Gr)] / Sum [rel. area (D, Gl) 100], in comparison with the functionalization degree determined by acid-base titration.

The deconvolution method shows that f-MWCNT(55) was the most functionalized. It was found that the CFD decreases when the reaction temperature increases as seen in Figure 4.10. In addition, the Raman spectra of functionalized carbon nanotubes show the significant disorder on the carbon nanotube compared to the pristine sample. The strong difference relay on their area fit and I_G/I_D peak ratio. The intensity of minor band is plotted as function of the reaction temperature. Furthermore, the trend of *D* band in first order is intensely correlated with the concentration of the carboxylic group in the sample obtained from acid-base titration. Which proved that f-MWCNT(55) is the most functionalized sample and that can be confirmed also by Zeta potential analysis. The *D* band trends in first and second order, *G* band trends first order, 2*G* band trends second order and satellite *S* band trends first order are shown in Figure 4.11. Further Zeta potential analysis gives necessary information about the chemical functionalization degree (CFD) of the samples under study in the next section.

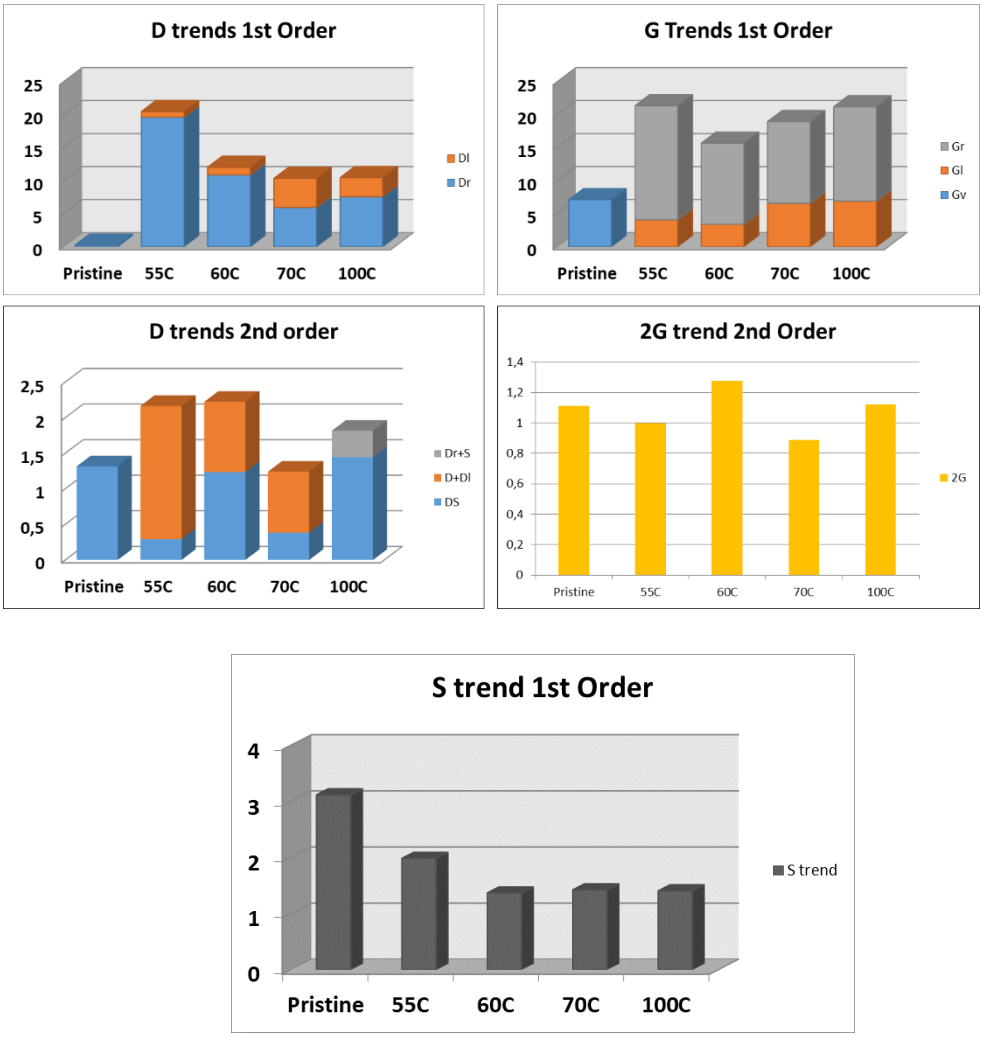

Figure 4. 11: Histogram gives percentage of intensity of the D, G, 2G and S bands in first and second order. The model provided a quantification of the band broadening which shows that D band has been typically associated with disorder on the graphitic material.

4.1.3. Zeta Potential Analysis of f-MWCNTs

Few amount (≤ 1 mg) of samples under study were dispersed in 3 ml of distilled water. Shake and place into cell for measurement. These samples were negatively charged by deprotonation of the carboxylic acid groups produced during chemical oxidation. The results show that f-MWCNT(55) indicates high surface modification compared to other functionalized carbon nanotubes samples. A large broadening for 55 °C compares to other CNTs observe by Raman shifts can support this result. The Zeta potential and conductivity recorded of functionalized multi-walled carbon nanotubes are summarized in this Table 4.1 below:

Table 4. 1: Zeta potential and conductivity result of f-MWCNTs and pristine.

Temperature (°C)	Zeta Potential (mV)	Conductivity (mS. cm^{-1})
55	- 44.8 ± 0.05	0.02210
60	- 31.8 ± 0.05	0.01180
70	- 29.6 ± 0.05	0.00912
100	- 38.9 ± 0.05	0.01480
Pristine	- 13.8 ± 0.05	0.00910

The relative zeta potential spectra of the materials under study are shown in the appendix. Conductivity of the samples under study decrease as the mild oxidative temperature increase. Which is not the case with f-MWCNT(100) due to lower amount of the carboxylic group decrease in the sample. The quantification of the carboxylic was study by Boehm acid-base titration.

4.1.4. Titration of functionalized Multi-walled carbon nanotubes

Acid-base titration used to determine surface degree of functionalization of the f-MWCNTs (Table 4.2). Two aqueous solutions of different concentration of NaOH and HCl, were prepared to quantify carbonyl group on surface of carbon nanotubes. The following steps were done to perfect the results:

- MWCNTs-COOH reacts NaOH excess gives MWCNTs-COO^-Na^+ and NaOH,
- Filtration process to separate the MWCNT-COONa from the excess NaOH,
- Addition of HCl excess into the supernatants,
- Determination of the HCl excess by titration with NaOH.

Experimentally, a known amount of f-MWCNTs as can be seen in Table 4.2 added 15 ml NaOH 0.001 M. Sonicated for 10 min to disperse carbon nanotubes and filtrated. A volume of 11 ml of filtrated solution, added exactly 11 ml of HCl 0.001 M. To avoid titration of carbonic acid. It was boiling for 20 min to remove CO_2 from the solution. Cool down the solution. 2 ml of the solution was used to measure

pH. While 15 ml was splitted in tree (5 ml). Titrated with NaOH 0.001M up to neutral point pH 7. Table 4.2 gives details information about the neutralized reaction result of functionalized and pristine multi-walled carbon nanotubes. Further histogram showing dependence of the concentration of carboxyl group against refluxing reaction temperature displayed in Figure 4.12.

Table 4. 2: Titration results of pristine and f-MWCNTs.

Temperature (°C)	Time (hours)	Initial Mass (mg) f-MWCNTs	mmol COOH per mg f-MWCNTs	mg COOH per mg f-MWCNTs
55	24	1.2 ± 0.05	9.523×10^{-3}	4.287×10^{-1}
60	24	2.0 ± 0.05	2.295×10^{-3}	1.033×10^{-1}
70	24	1.8 ± 0.05	4.481×10^{-3}	2.018×10^{-1}
100	01	2.0 ± 0.05	3.451×10^{-3}	1.556×10^{-1}
Pristine	00	1.0 ± 0.05	1.400×10^{-3}	0.640×10^{-1}

These results evaluate quantitatively the concentration of functionalized group onto the surface of the multi-walled carbon nanotubes. Although the control parameter is mainly refluxing temperature and accompanied by the refluxing reaction time. The change in temperature affect efficiently surface environment of the carbon nanotube as can be seen in section 4.1 decreases of 1730 cm^{-1} absorption peak in the FT-IR Spectra.

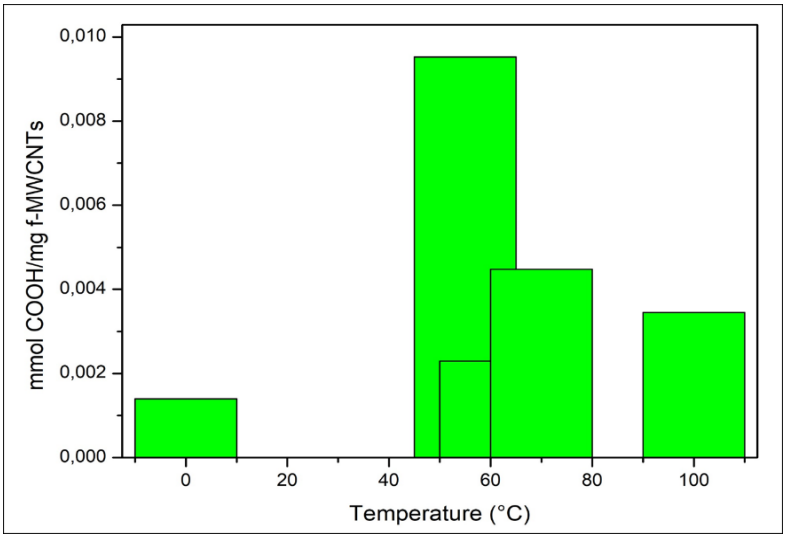

Figure 4. 12: Histogram of the concentration of mmol COOH/mg f-MWCNTs as function of Temperature.

From this result, it is noticeable that more carboxylic group have been attached on the surface of multi-walled carbon nanotubes at 55 °C. Thus, increase further refluxing reaction temperature destroy carbon nanotubes and favor formation of hydroxyl group. It observes with f-MWCNT(100) when the refluxing time extended to 24 hours. All carbon nanotubes were destroyed and Fourier transform infrared shows a broad large peak of hydroxyl group (appendix). The results from neutralization reaction allows clear compilation of data to quantify carboxyl group in the materials under study. As shown in the histogram, high concentration occurs at 55 °C and decrease with increasing temperature. In order to uncertain this CFD, the morphology images of the samples under study were obtained using Field Emission – Scanning Electron Microscopy.

4.1.5. Scanning Electron Microscopy

Experimentally, 0.1 mg of samples under study was firstly dispersed in 5 ml isopropanol, sonicated for 60 min at 27 °C to obtain a homogenous dispersion of the MWCNTs. A Silicon substrate was sonicated for five minutes with acetone followed by, 5 min using isopropanol. Then it was flushed with N_2 gas to prepare the surface as a support for CNTs. The solution is drop cast on a silicon substrate using a micro pipe.

Field Emission Scanning Electron Microscope (FE-SEM) imaged the morphologies of the samples under study at same magnification of 100 nm. It should be noticeable that not significant differences were monitored by comparing the samples under study.

Figure 4.13 gives the SEM micrograph of the pristine and functionalized multi-walled carbon nanotubes. Unfortunately, the quality of these images is not very high. Nevertheless, stronger changes in term of the morphologies can be seen in the High Resolution electron transmission micrographs or TESCAN micrographs. Further electronic transport was also done to study the conductivity and the resistance of these chemical functionalized carbon nanotubes. In this case, the aligned carbon nanotubes devices were fabricated for *I-V* characteristic measurement.

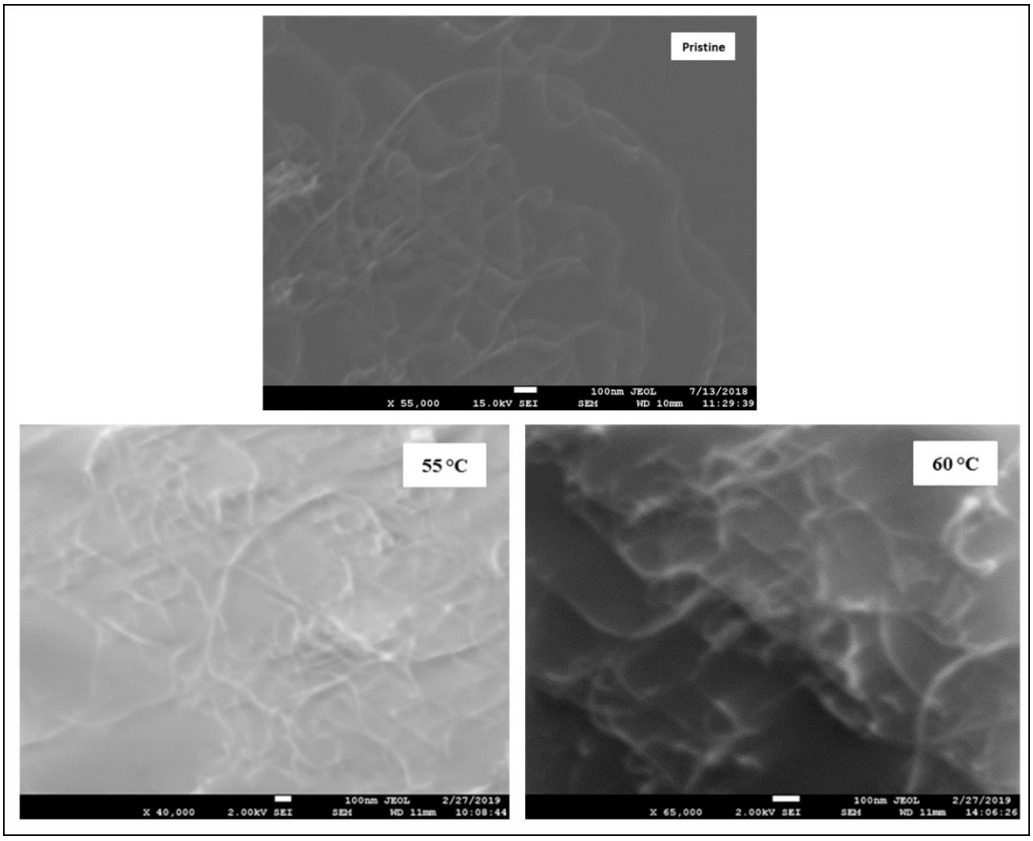

Figure 4. 13: Morphologies of the pristine CNTs and functionalized multi-walled carbon nanotubes 55 °C and 60 °C taken at same magnification.

4.1.6. I-V Characteristic of f-MWCNTs

The intensity of the current versus bias voltage measured of the functionalized multi-walled carbon nanotubes at room temperature is shown in Figure 4.14. It has been measured using the semiconductor device analyzer (B1500A). The calibration of the instrument was done by connecting two points in contact and *I-V* sweep was measured. It should give resistance below 25 Ω to certainly that machine is ready for measurement.

I-V measurement results show the pristine sample contains no carbonyl group, which can be justified by the slope of the current against bias voltage. The change in the slop indicates modification in the material under study. The slop of functionalized carbon nanotubes consecutively change compared to pristine sample. That can be assign to the novel group attached onto the surface of multi-walled carbon nanotubes. The maximum the current of 80 µA recorded in the range of - 3.5 mV to 3.5 mV.

Relative resistance has been calculated for each functionalized multi-walled carbon nanotubes. It is well known that the pristine MWCNT behaves as metallic material [104]. Their resistance increases with temperature. By breaking of pi bonds, this affects the mobility of the electron. This should be the main reason of the increases in resistance in the functionalized multi-walled carbon nanotubes samples. The resistance of the device at room temperature was recorded in the range of 28.0 – 55.0 kΩ which is larger than the fundamental resistance quantum of 25.9 kΩ and thus the requirements for the Coulomb blockade regime are encountered [14]. The values of the resistance observed on the functionalized MWCNTs is shown in Figure 4.14. This result indicate that average resistance can be increases with reaction temperature and being reversible.

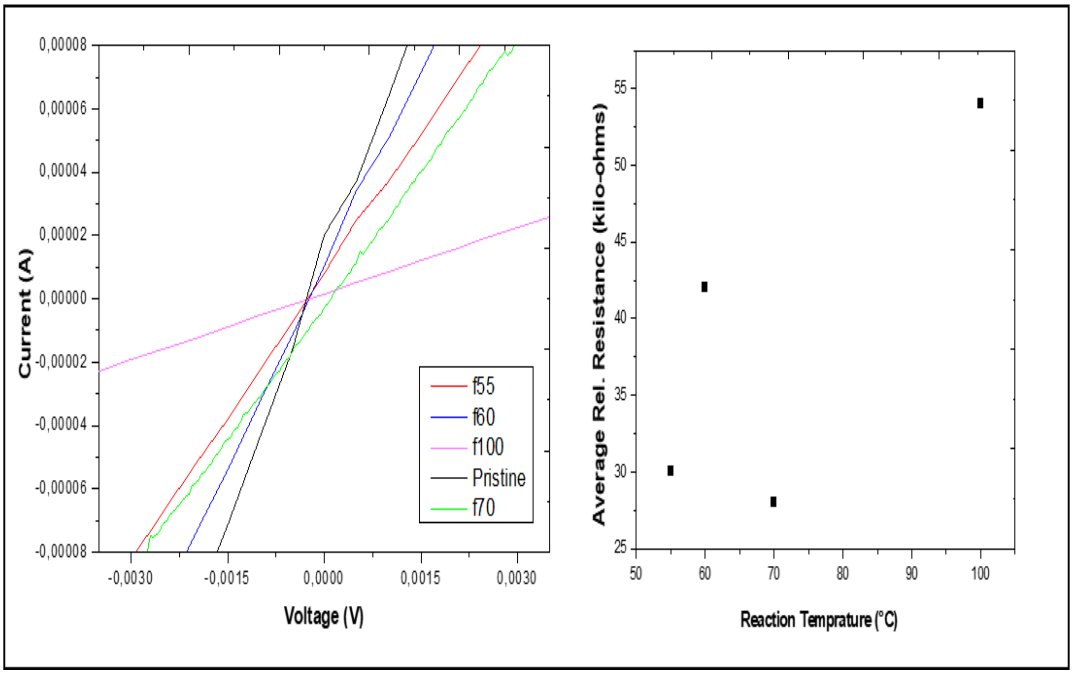

Figure 4. 14: I-V measurement of Pristine and f-MWCNTs (left). Average Relative Resistance as function of reaction temperature (right).

4.2. Gadolinium-DTPA loaded onto surface of f-MWCNTs

This sub-section presents the results of characterization of the following techniques: Fourier Transform Infra-Red spectroscopy; Raman spectroscopy; Induced Coupled Plasma-Optical Emission Spectroscopy; High Resolution Transmission Electron Microscopy, and electronic transport associated with magnetic measurement. It is also give a discussion on the correlation of the main results.

4.2.1. FT-IR spectroscopy

The complex magnetic molecular Gd-DTPA loading into functionalized carbon nanotubes Gd-DTPA-f-MWCNTs was submitted to FT-IR to validate the chemical reaction. These results have shown that the complex chelate molecular (Gd-DTPA) can be linked with the functionalized multi-walled carbon nanotubes (f-MWCNTs) via amide organic group. The results from TOP-SEM can be used as the confirmation and additional data of these FT-IR pattern results.

In fact, the wavenumber in the range of 1672 cm^{-1} indicate the presence of C-N vibrations. The wavenumber 670 - 770 cm^{-1} represents the Gd-N mode. The chemical groups C-O and C=O stretching vibrations are represented by the peaks in the range of 110 cm^{-1} and 1760 cm^{-1}, respectively. In particular, the peak at 1660 cm^{-1} and 1750 cm^{-1} confirm the presence of two carbonyl environments. In addition, sample reflux at 55 °C shows a new carbonyl environment in the range of 1826 cm^{-1}.

The samples indicate intense peak at 633 cm^{-1}, which directly governed the stretching vibration of Gd-O in the materials. This peak is observed in all samples. It weakly appears on the sample refluxed at 100 °C due to lower carboxylic group in this particular sample. That can be correlates with the ICP-OES results indicated lower percentage of Gd loaded due to less concentration of the carboxylic group in the samples. Figure 4.15 shows FT-IR spectra of Gd-DTPA loaded in the multi-walled carbon nanotubes taken in the range of 600 - 4000 cm^{-1}. The wavenumber from 600 cm^{-1} to 2000 cm^{-1} is zooming on top-right in the Figure 4.15, indicating the organic function and different stretching vibration in the materials.

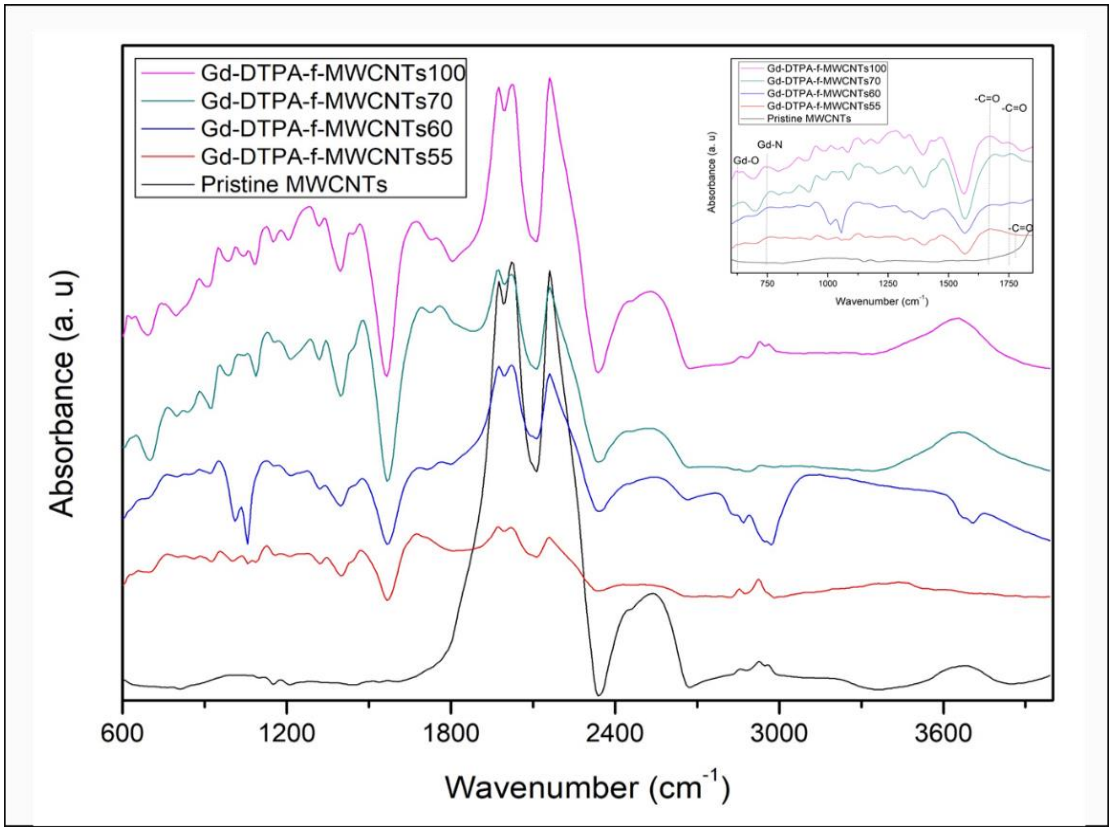

Figure 4. 15: FTIR spectra of pristine and Gd-DTPA loaded into functionalized multi-walled carbon nanotubes.

4.2.2. TOF-SIM spectrometry

Figure 4.16 gives the surface morphologies of the material. That was obtained from FIB-SEM. Time of flight secondary ion mass spectrometry (TOF-SIMS) results obtained from the loading Gd-DTPA onto the surface of carbon nanotubes Gd-DTPA-f-MWCNTs are further given in Figure 4.17. The measurements were taken in 25 x 25 μm^2. LYRA3 FIB scanning electron microscope with C-TOF was used for this analysis. TOF-SIMS analysis was done in positive ion mode with 4 min time of flight, using Gallium gun source of energy of about 30 KeV to produce the ion fragment. The ion beam current was one nano-amperes. The time of flight was measured with the TOFWERK detector.

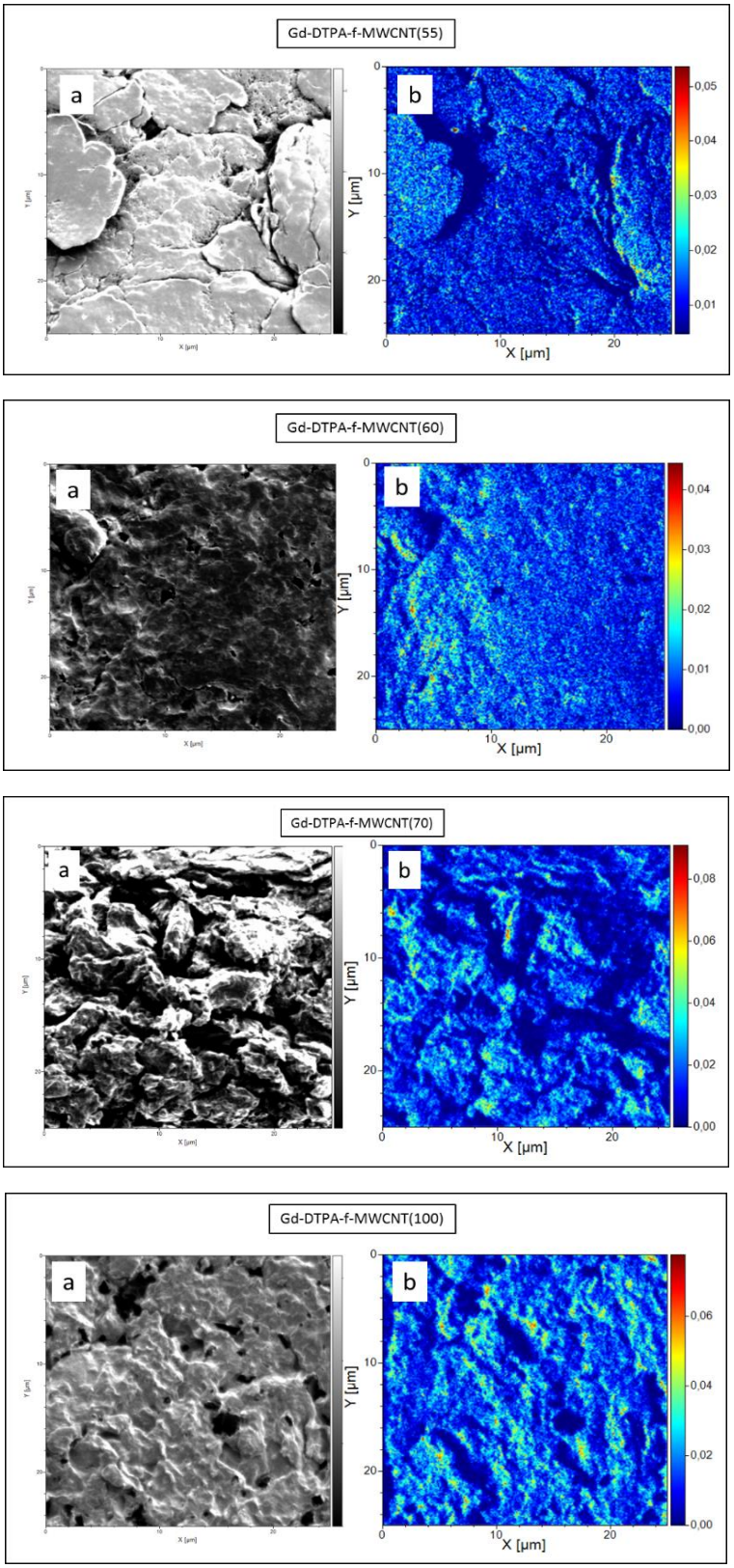

Figure 4. 16: Showing morphologies images taken on the surface of Gd-DTPA-f-MWCNTs materials. The focused Ion bean scanning electron images (a). Distribution map of Gadolinium ion Ga (b). This result show that the change in the morphology can be affected by reaction temperature of during the covalent functionalization of the multi-walled carbon nanotubes.

This technique investigates qualitative elemental and molecular composition of the materials under study. Magnetic complex Gd-DTPA was chemically loaded with stoichiometry mole ratio 1:1 with the carboxylate functionalized multi-walled carbon nanotubes for 24 hours at 30 °C. TOF-SIMS result confirmed the loading of the Gd-DTPA onto the functionalized multi-walled carbon nanotubes via the carboxylate group of functionalized carbon nanotubes.

Mass charge ratio of 158 m/q indicates that the isotope $^{158}Gd^{+}$ with the relative intensity approximately of 1 x 10^{-3} dominated in the Gd-DTPA-f-MWCNTs. Thus, the value obtained for the Gd-DTPA-f-MWCNT(60) slightly differed with the other samples in term of the mass-charge ratio. Which gives the relative intensity in the range of 1 x 10^{-4}. That can directly correlate with the ICP result and acid-base titration obtain in this sample. Showing slightly lower % Gd and significant changes in the concentration of the carboxylic group in the sample. In addition, the fragment $(^{158}Gd^{16}O)^{+}$ ion appear in the relative intensity approximately 1 x 10^{-4} for the Gd-DTPA-f-MWCNT(60) which has the lowest value of intensity compared to other samples. This result makes TOF-SIMS a semi-quantitative technique for elemental and molecular analysis of the materials.

TOF analyzer makes possible to distinguish between several ion species even at the same nominal mass. The presence of fragmentation pattern of gadolinium isotopes and $(^{158}Gd^{16}O)^{+}$ were showing a positive secondary ion mass spectra of Gd-DTPA-f-MWCNTs materials in high mass range as inserts the Figure 4.17. This chemical species reveal the chemical attachment of Gd from the magnetic molecular Gd-DTPA linked with the oxygen from carboxylic group of functionalized the multi-walled carbon nanotubes.

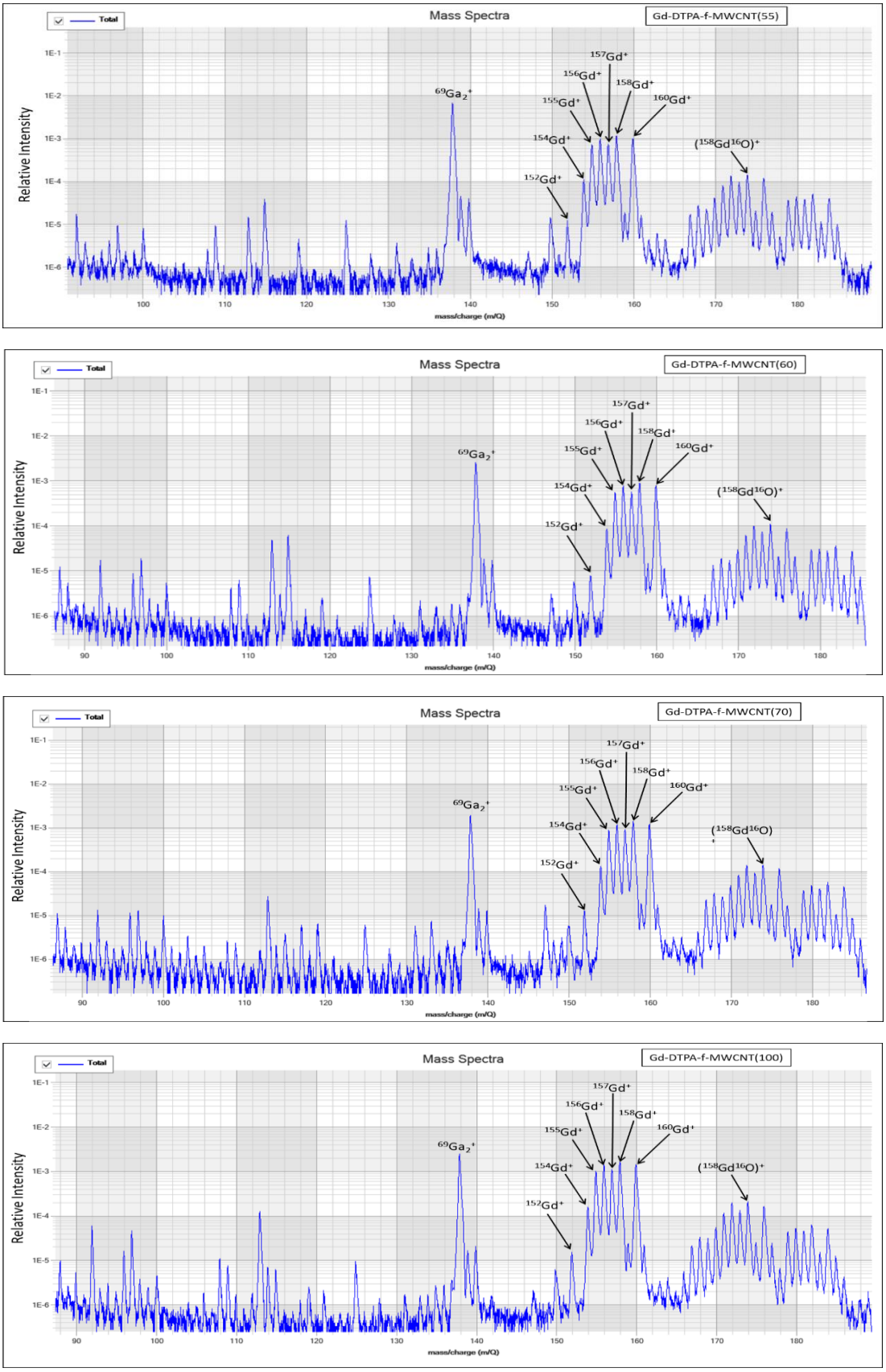

Figure 4. 17: Showing a positive secondary ion mass spectra of Gd-DTPA-f-MWCNTs materials in high mass range. Indicating the presence of fragmentation pattern of gadolinium isotopes and $(^{158}Gd^{16}O)^+$ ion in the material under study.

4.2.3. Raman spectroscopy

The Raman spectra were obtained in the range 400 cm^{-1} – 3500 cm^{-1}. Those Raman data were taken in two different areas using the laser excitation (514 nm). The bright region of each sample show greater background, and dark region with less background which can be assigned to MWCNTs area with no excitation electrons. Figure 4.18 displayed the Raman spectrum of the loaded functionalized multi-walled carbon nanotubes refluxed at the temperature of 55 degree Celsius. The inserts in Figure 4.18 gives their images. It is necessary to mention that the deconvolution method was performed in the Gd-DTPA-f-MWCNT(55) black area side data. That was done in first order which located in the Raman shift between 800 cm^{-1} – 2000 cm^{-1} of the Raman spectrum. The comparison of the spectra for absolute values would be more feasible if background substation carried out.

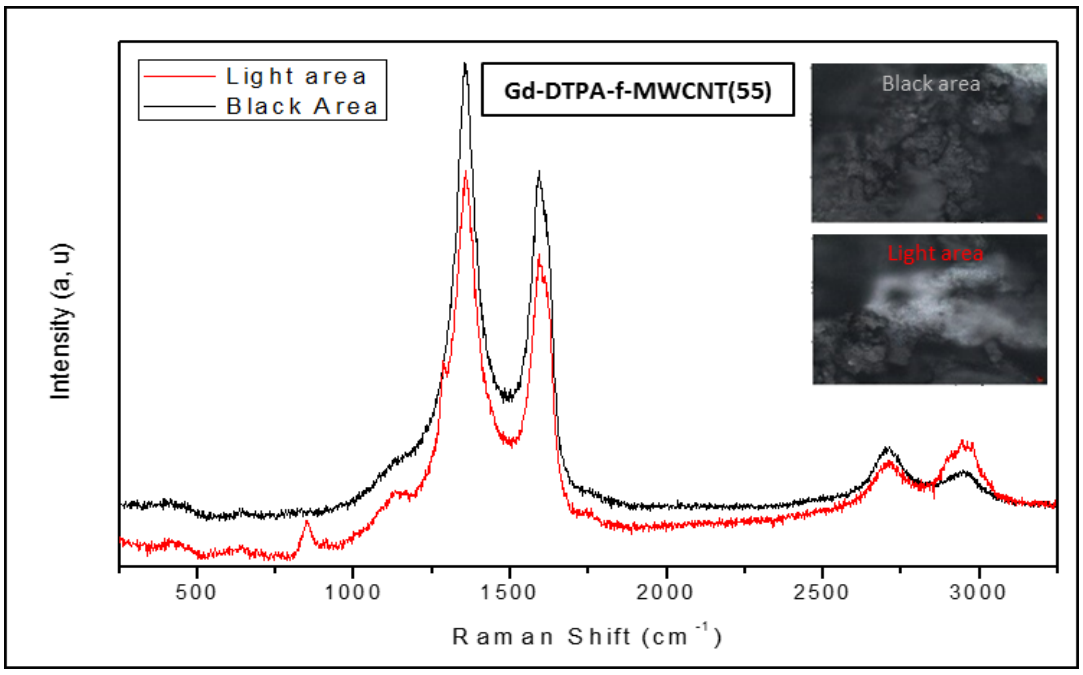

Figure 4. 18: Comparison of light and black area Raman spectra of magnetic molecular Gd-DTPA chemically reacted with functionalized multi-walled carbon nanotube in the period of 24 hours. The intense peak between 1000 cm^{-1} and 2000 cm^{-1} attributed in *D* and *G* bands.

The deconvolution model was used to quantitatively evaluate the changes in the area fit and intensity of the fitting bands as depicted in Figure 4.19. Concerning the

Gd-DTPA loaded onto functionalized carbon nanotube [f-MWCNT(55)] sample, the best fitting of this material was done using seven Lorentzian peaks. The inserts of Figure 4.19 illustrates deconvolution pattern of Gd-DTPA-f-MWCNT(55) materials.

Raman studies of polycyclic aromatic hydrocarbons presented bands near 1250 and/or 1400 cm^{-1}, with deviations in the Raman shift position and relative intensity depending on the molecular size and symmetry, as well as, one peak at around 1600 cm^{-1}. [120, 125]. Moreover, the Raman spectra of polyacetylene show two features at 1200 and 1500 cm^{-1} [126]. Thus, fitting bands Dl, Dr and Gr in the present deconvolution model were assigned to the existence of low size aromatic domains, analogous structures to PAH's, [120, 125] while S and Gl bands are identified to fingerprints of polyacetylene like structures [126]. Furthermore, the Raman spectra of fullerenes show a base feature at approximately 1500 cm^{-1}, thus the Gl band can also have contributions from tube-end vibrations, but this is not very sure for MWNCTs.

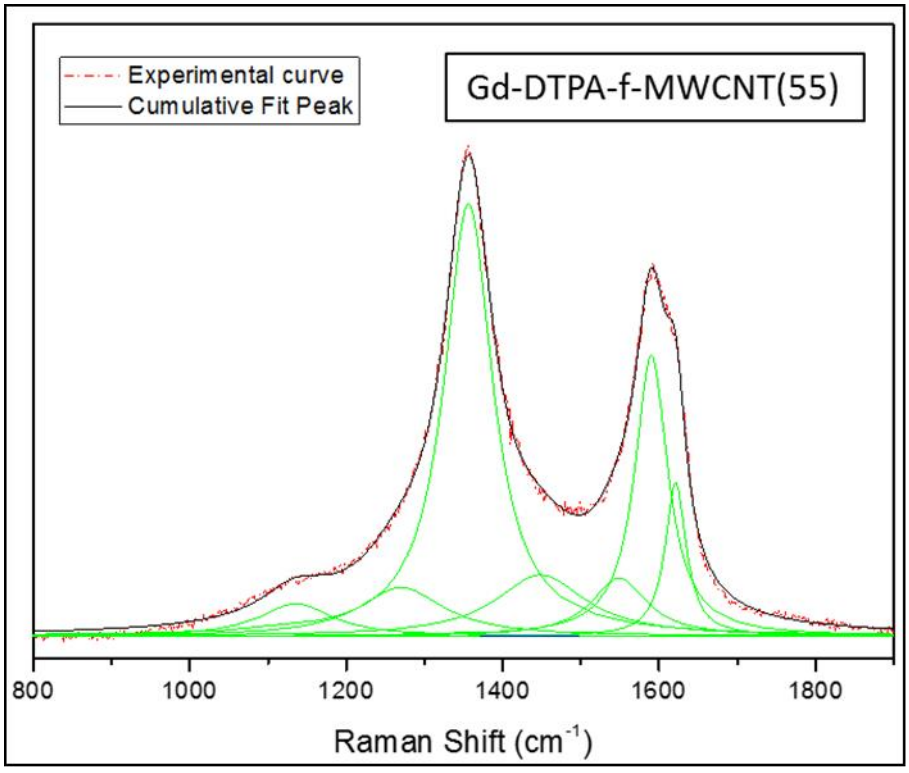

Figure 4. 19: Deconvolution of Raman spectra of Gd-DTPA-f-MWCNT(55) using a 514 nm excitation laser. It was taken in the range from 800 cm^{-1} to 1900 cm^{-1} of the Raman spectrum.

Those fitting peaks are identified as satellite bands in the range of 800 cm^{-1} to 1900 cm^{-1}. However, the satellite peak namely S, Dl, Dr, Gl and Gr bands are necessary recognized in the peak positions corresponding to 1135.5 cm^{-1}, 1270.4 cm^{-1}, 1448.5 cm^{-1}, 1548.9 cm^{-1} and 1621.6 cm^{-1}, respectively. The presence of the fitting peaks DI, Dr, and Gr were attributed to manifestation of the low aromatic domain [120, 125]. Although the S and GI bands are assigned to polyacetylene like structure [126]. The polycyclic aromatic hydrocarbons showed bands in the vicinity of 1250 and 1400 cm^{-1}. The variations in the position and relative intensity depends on the molecular size and symmetry. These samples show the increase in the Raman shift and intensity of the band (S and GI) compared with the covalent functionalized multi-walled carbon nanotubes [f-MWCNT(55)]. This designated the growths fingerprints of ligand Gd-DTPA in the materials under study.

It was remarkable to see the broadening of the *D* and *G* bands in the spectra of Gd-DTPA-f-MWCNT(55). Moreover, there is fluctuation in term of the percentage area of *D* and *G* bands in this material. The percentage area of *D* band increases approximately 23 % and 2 % in the *G* band. That was found when compared the f-MWCNT(55) sample with the loaded Gd-DTPA onto the surface f-MWCNT(55) material, namely Gd-DTPA-f-MWCNT(55). In addition, percentage area of *D* and *G* bands can be associate with intensity ratio $I_{D/G}$ which confirmed this increment varying from a value of 1.191 ± 0.003 to 1.264 ± 0.002 on the loaded sample with Gd-DTPA.

The changes in the Raman spectra resulting to the new organic functional group attached on the carbon nanotubes. However, the huge change can be observed in the first order *D* and *G* bands, particularly in the range of 500 cm^{-1} to 1200 cm^{-1}. The Gd-DTPA-f-MWCNT(55) magnetic complex sample behaves differently compared to other samples in this range of wavenumber. Moreover, that can be observed even its second order of the Raman spectrum. This can be justified in fact that the concentration of gadolinium is more dominated onto the surface of carbon nanotubes and increases disorder revealed on the Raman shift.

Instead, Figure 4.20, offers Raman spectrum of the sample obtained by the loading of Gd-DTPA onto the surface of the multi-walled carbon nanotubes refluxed in acid mixture for 24 hours in the temperature of 60 degree Celsius, indicating the two main area. Light region and dark region as shown in left of the Figure 4.20 below.

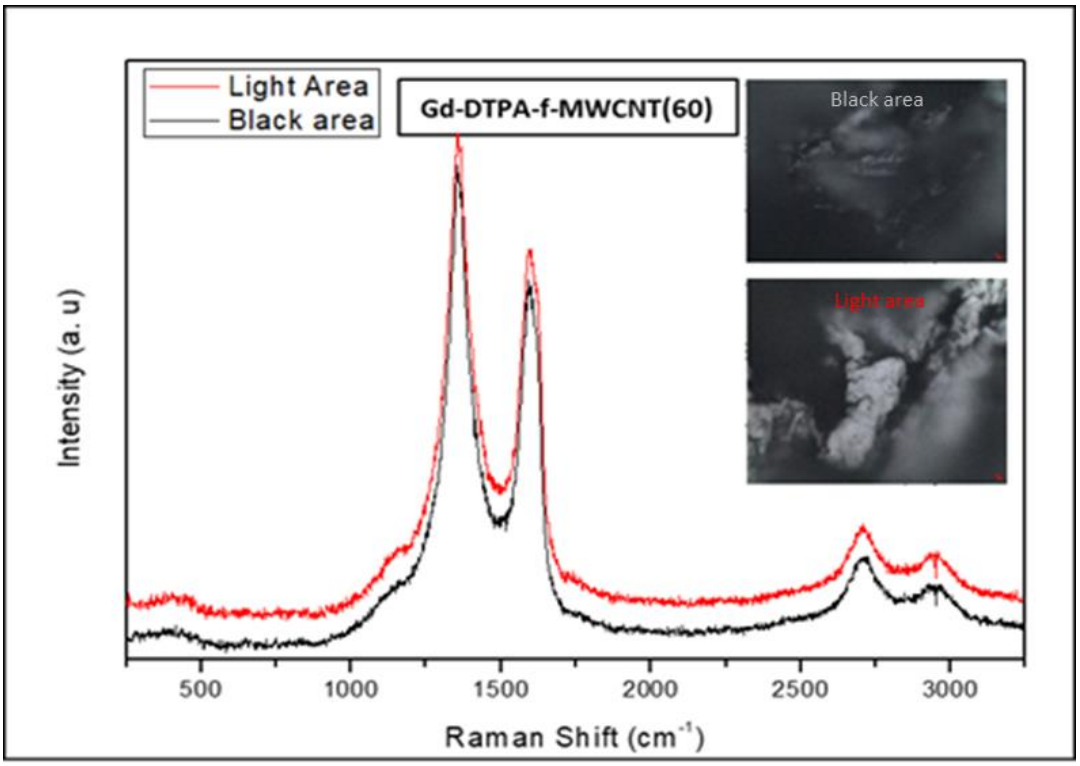

Figure 4. 20: Comparison of light and black area Raman spectra of magnetic molecular Gd-DTPA chemically reacted with f-MWCNT(60) in the period of 24 hours. The intense peak between 1000 cm^{-1} and 2000 cm^{-1} attributed in *D* and *G* bands.

The deconvolution model was used to calculate the changes in the area fit and intensity of the fitting bands. The best fit for the spectrum (black area) was done using seven Lorentzian peaks. The inserts of Figure 4.21 illustrate the deconvolution pattern of Gd-DTPA-f-MWCNT(60). The fitting peaks S and GI bands are in 1143.2 cm^{-1} and 1503.9 cm^{-1}, respectively. This shows that there is an increase in the position and relative intensity of these two sub-peaks (S and GI) compared to the functionalized multi-walled carbon nanotubes [f-MWCNT(60)]. That can be indicating the progression fingerprints of polyacetylene structures which can be

resulting from Gd-DTPA complex molecular attached onto the multi-walled carbon nanotubes.

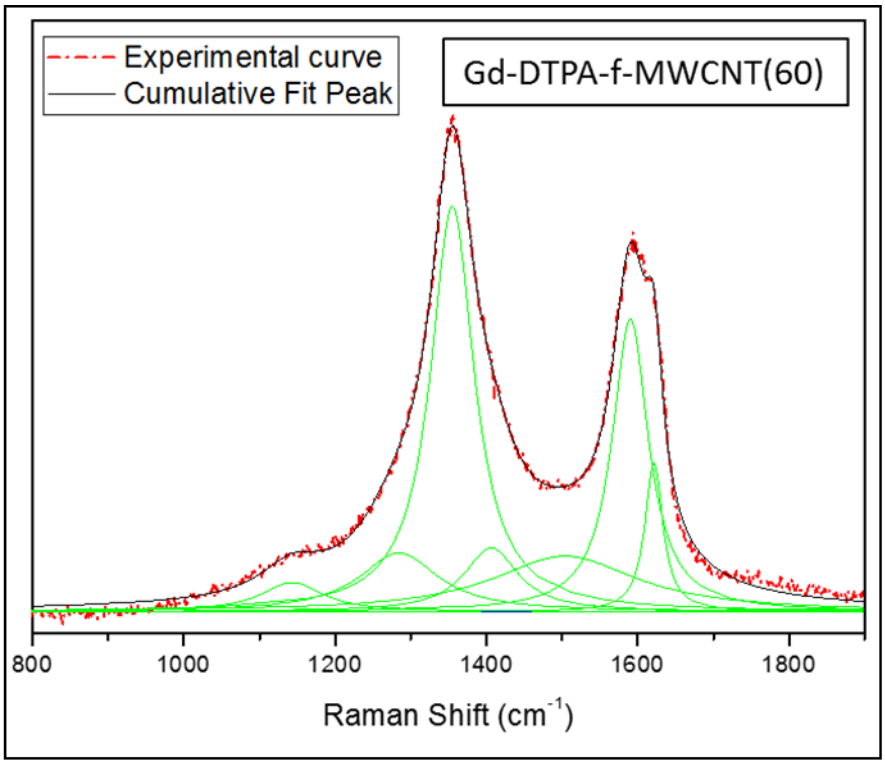

Figure 4. 21: Deconvolution of Raman spectra of Gd-DTPA-f-MWCNT(60) using a 514 nm excitation laser. It was taken in the range from 800 cm^{-1} to 1900 cm^{-1} of the Raman spectrum.

Deconvolution pattern shows significantly the changes happened in term of the intensity ratio, and the percentage area of *D* band as well as *G* band. In comparison with functionalized multi-walled carbon nanotubes [f-MWCNT(60)] without gadolinium loading. The calculated intensity ratio slightly decreases from 1.262 ± 0.003 to 1.231 ± 0.004. Whereas the percentage of the area of *D* band varying from 28.57 % to a value of 36.17 %. The relative % area of *G* band decreases slight about 1 % with the increase in *D* bands. This behavior was expected to express the order of the graphitic materials.

In addition, it was found that the intensity ratio decreases with a value of 0.033 compared to the loaded Gd-GTPA onto the functionalized carbon nanotubes Gd-DTPA-f-MWCNT(50). This can be due to the lower disorder in the

Gd-DTPA-f-MWCNT(60) governed by the concentration of the carboxylic group in the material.

Concerning the sample Gd-DTPA loaded chemically in the carbon nanotubes oxidized at 70 degree Celsius. The previous plotted Raman data in Figure 4.20, indicates slightly similarity of in the intensity ratio between functionalized and Gd-DTPA loaded sample. The slight difference can be estimating about of 0.050 in term of intensity ratio. Therefore, it shows a closest value to the intensity ratio of Gd-DTPA-f-MWCNT(55).

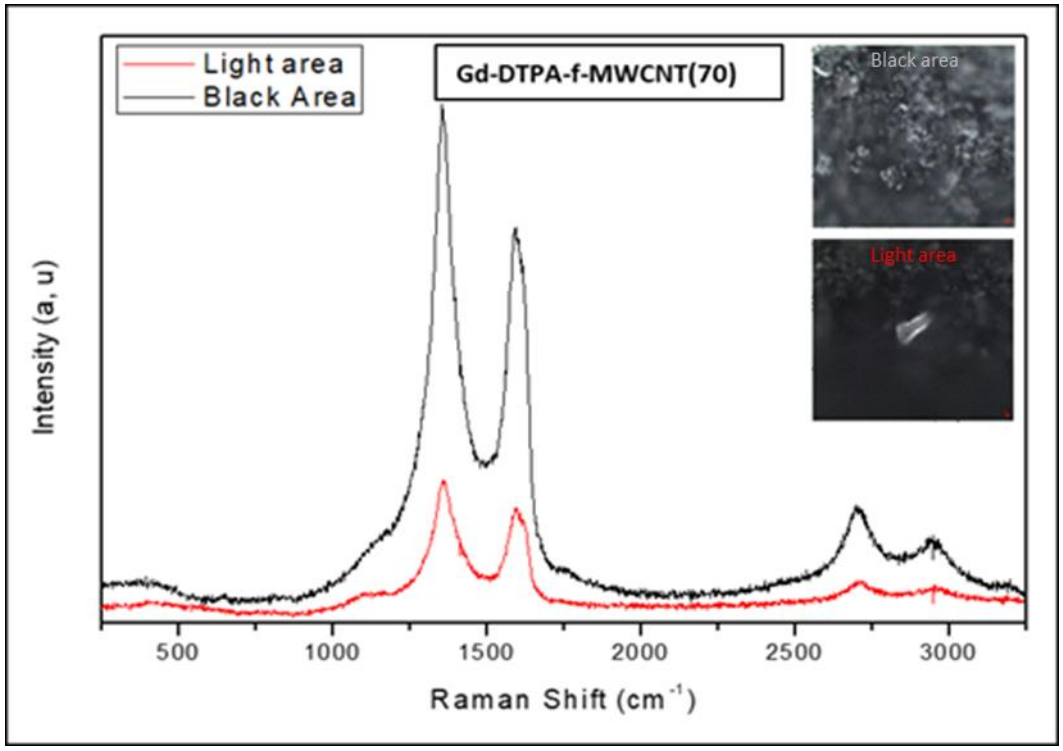

Figure 4. 22: Comparison of light and black area Raman spectra of magnetic molecular Gd-DTPA chemically reacted with f-MWCNT(70) in the period of 24 hours. The intense peak between 1000 cm^{-1} and 2000 cm^{-1} attributed in *D* and *G* bands. Range between 2000 cm^{-1} to 3300 cm^{-1} assigned to 2D band.

Deconvolution pattern provides the useful information about the % area of the *D* and *G* bands. To compare the level of disorder in the material between functionalized and Gd loaded sample. The percentage area of those samples show an increases from 31.72 % to 36.20 % and 21.65 % to 22.40 % in the *D* and *G* bands respectively. Certain researchers have shown that Raman studies of the polycyclic aromatic

hydrocarbons (PAH's) exhibited bands near 1250 cm^{-1} and 1400 cm^{-1}, with a change in the position and relative intensity depending on the molecular size and symmetry, including one additional peak at around 1600 cm^{-1}. [120, 125]. However, this sample has shown increases in position and intensity of the S band with decrease in position of GI bands compared with the functionalized multi-walled carbon nanotubes f-MWCNT(70). This can be resulting from the changes in the structure due to the presence of magnetic complex Gd-DTPA in the sample.

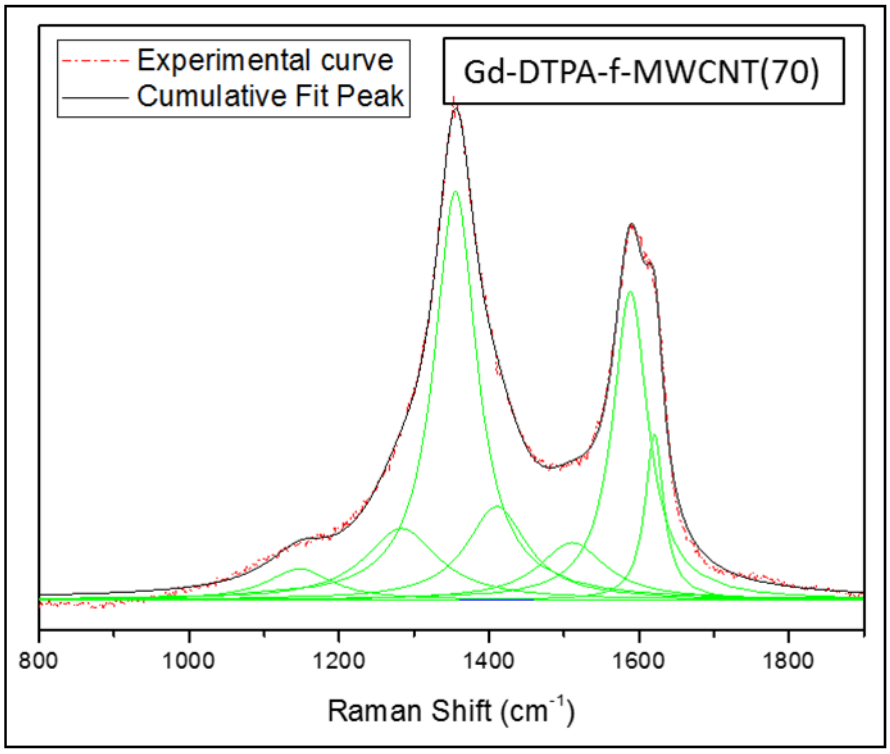

Figure 4. 23: Deconvolution of Raman spectra of Gd-DTPA-f-MWCNT(70) using a 514 nm excitation laser. It was taken in the range from 800 cm^{-1} to 1900 cm^{-1} of the Raman spectrum.

In relation to Gd-DTPA-f-MWCNT(100) sample, *D* and *G* bands resulting from the deconvolution model, the relative percentage area increases more from functionalized multi-walled carbon nanotubes [f-MWCNT(100)] compared with the chemically loaded Gd-DTPA on the multi-walled carbon nanotubes Gd-DTPA f-MWCNT(100). The percentage area of those samples show an increase from 31.30 % to 42.20 % and 16.35 % to 22.9 % in the *D* and *G* bands, respectively. Figure 4.24 displayed deconvolution pattern of the Raman data after background substration for the loaded

Gd-DTPA attached onto functionalization of multi-walled carbon nanotube prepared at 100 degree Celsius. Consequently, the S and GI bands obtain at 1141.4 cm^{-1} and 1566.7 cm^{-1} attributed to the fingerprints of polyacetylene structures governed by the presence of Gd-DTPA chemically attached with functionalized multi-walled carbon nanotubes prepare at the temperature of 100 °C, namely Gd-DTPA-f-MWCNT(100) material. This result has displayed clearly an increase in term of S band with a decreases in the GI band compared to the f-MWCNT(100) sample without gadolinium loading in the sample.

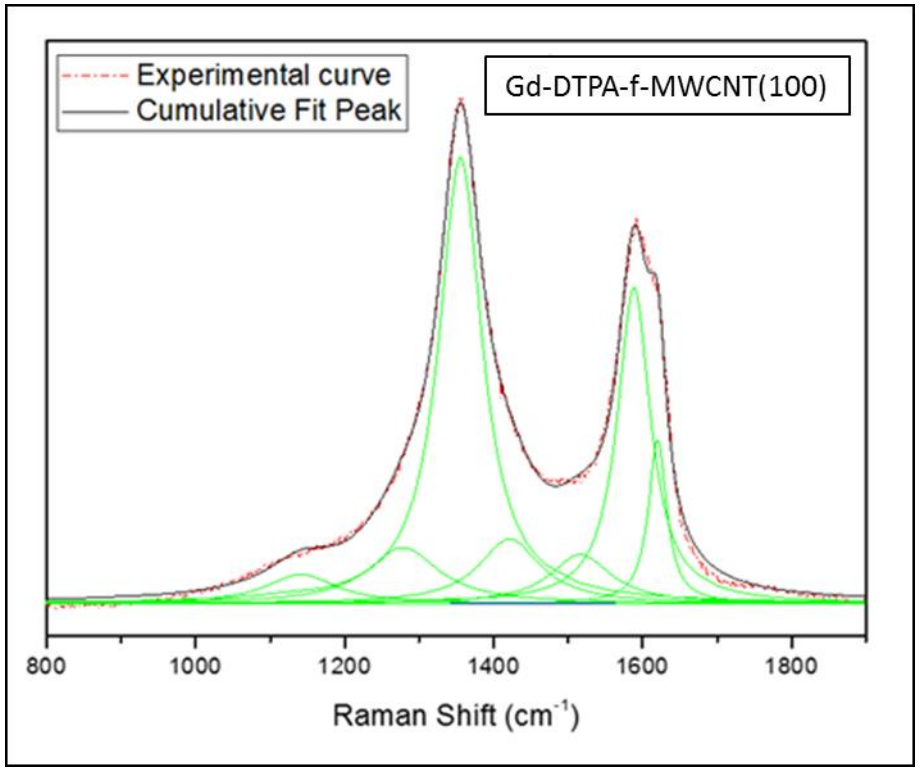

Figure 4. 24: Curve-fitting Raman spectra of Gd-DTPA-f-MWCNT(100) using a 514 nm excitation laser. Less significant change observed in the intensity ratio of *D* and *G* bands. Deconvolution was taken in the range from 800 cm^{-1} to 1900 cm^{-1} of the Raman spectrum.

The previous Raman spectra have shown the presence of the satellite S, DI, Dr, Gl and Gr band in the spectral feature of the curve-fitting. Those satellite bands were observed in all loaded sample with Gd-DTPA. Which were chemically prepared identical way. The intensity ratio of *D* and *G* bands of loaded samples with Gd-DTPA have shown a greater similarity. The calculated crystallite size using Tuinstra Koenig

relation in the Gd-DTPA-f-MWNCT samples have been shown as well large similarity because, it depends on the intensity ratio of *D* and *G* bands. It was revealed that the loaded samples with Gd-DTPA at 55, 60, 70 and 100 °C of functionalized multi-walled carbon nanotubes have crystallite size of 3.49, 3.56, 3.50 and 3.49 nm, respectively.

This can stand for a novelty of this Raman result. Moreover, the relative areas of these satellite bands related to the structural complexity introduced upon the material via stoichiometry chemical reaction of Gd-DTPA with f-MWCNTs.

The compilation of the images attached in each single Raman spectra can be state as the laser excitation energy reacts with the material and produces two regions. The blacker area which can be attributed to the closest point where gadolinium occupy since the electron density of Gd is much higher. That show higher florescence. A typical Raman Spectrum of Gd-DTPA-f-MWCNT(100) sample shown in Figure 4.25 displayed black and light region as well. The electron absorbs the energy. Delocalization of electron might be conducted in this area. In this case it is not very sure because this should lead to observe strong electron-phonon coupling of delocalized pi-electron. Florescence should be done in future to observe the excitation of Gd-electrons which moving from one state to another state.

As the samples have been loaded with gadolinium in respect of the chemical stoichiometry of the reaction. Further confirmation of the % Gd in the samples was studied by inductively coupled plasma-optical emission spectrophotometry (ICP/OES) to support the Raman and FI-IR results which indicated huge changes in the Raman spectra of the material under study.

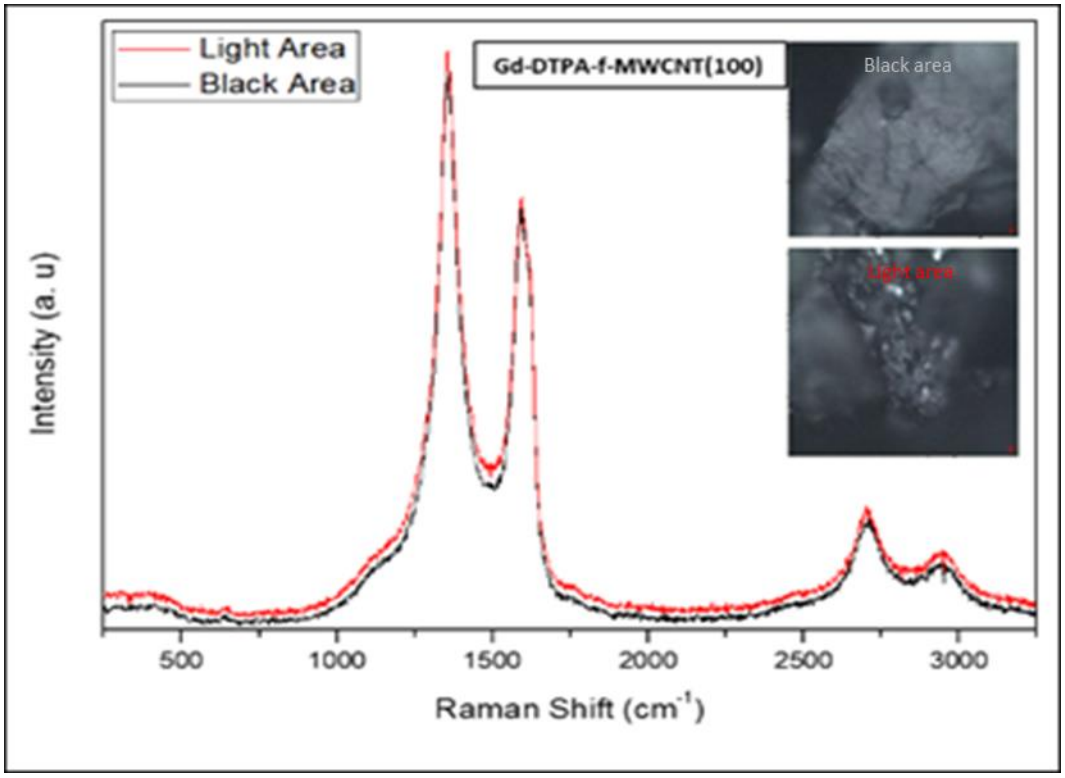

Figure 4. 25: Comparison of light and black area Raman spectra of magnetic molecular Gd-DTPA chemically reacted with f-MWCNT(100) in the period of 24 hours. The intense peak between 1000 cm^{-1} and 2000 cm^{-1} attributed in *D* and *G* bands. Range between 2000 cm^{-1} to 3300 cm^{-1} assigned to 2D band.

4.2.4. Inductively Coupled Plasma-Optical Emission Spectrometry

The percentage of gadolinium in each Gd-DTPA-f-MWCNTs sample was determined by inductively coupled plasma-optical emission technique. Sample was injected into a radiofrequency (RF) induced argon plasma using one of the nebulizers. It sprayed reach the plasma and is rapidly dried, vaporized and excited by collisional excitation. The atomic emission emanating plasma is seen either in a radial or axial configuration. With aid of a lens, the results is collected in the selector device. Then, weight percentage of selected element are recorded. Table 4.3 gives ICP/OES results of each single sample in term of the percentage. As the sample were prepared in function of reaction temperature.

Table 4. 3: Percentage of Gadolinium in the each samples.

Samples composition	% Gd (w/w)
Gd-DTPA-f-MWCNT(55)	4.95 ± 0.02
Gd-DTPA-f-MWCNT(60)	5.00 ± 0.02
Gd-DTPA-f-MWCNT(70)	5.48 ± 0.02
Gd-DTPA-f-MWCNT(100)	5.76 ± 0.02

The result from ICP-OES show that the percentage of Fe found is less than 0.19 %. This is because Fe and cobalt were used as catalyst during CVD. Base on the calculation, the percentage of gadolinium loaded in this sample is higher compared to pristine samples. This can be justified by titration results which proved that f-MWCNT(55) contains higher concentration of 9.523×10^{-3} mmol COOH per mg of f-MWCNTs. In addition, it is testifying that the chemical reactions of loading Gd-DTPA onto the surface of the carbon nanotube were totally successful.

It is noticeable that the % Gd is varying with increase temperature. This is due to the high effect of functionalization of multi-walled carbon nanotubes. High concentration of carboxyl group indicate high needs of Gd-DTPA surrounding the f-MWCNTs. The cation Gd^{3+} shows strong interaction with COO^- and tertiary Nitrogen of DTPA molecule. The hydroxyl group presents also great affinity with Gd^{3+} due to its electronegativity governed to oxygen atom. Although we know the concentration of carboxylic acid which can be main site of attachment of the ligand in the sample. In the totally absence of hydroxyl group. Less number of carboxylic group revealed by lower amount of Gd^{3+}. In this case, it noticeable that OH- group also might played a role in the others samples. In the FTIR spectra. The peak at 1660 cm^{-1} and 1750 cm^{-1} confirm the existing of two carbonyl environments in the sample 60, 70 and 100 °C. But the sample reflux at 55 °C shows a new carbonyl environment in the range of 1826 cm^{-1} related only to carboxylic group. Although the Gd-DTPA-f-MWCNTs(100) sample dominates as shown in Figure 4.26 which can be resulting from the affinity of the hydroxyl with Gd^{3+} in the sample. X-ray photoelectron spectroscopy will be done in future to determine the ratio of hydroxyl and carboxylic group in the samples. This plotted revealed that the

Gd-DTPA-f-MWCNT(55) will be more stable in term of temperature controlling the loading of the magnetic complex molecular and gives higher concentration of carboxylic group in the material.

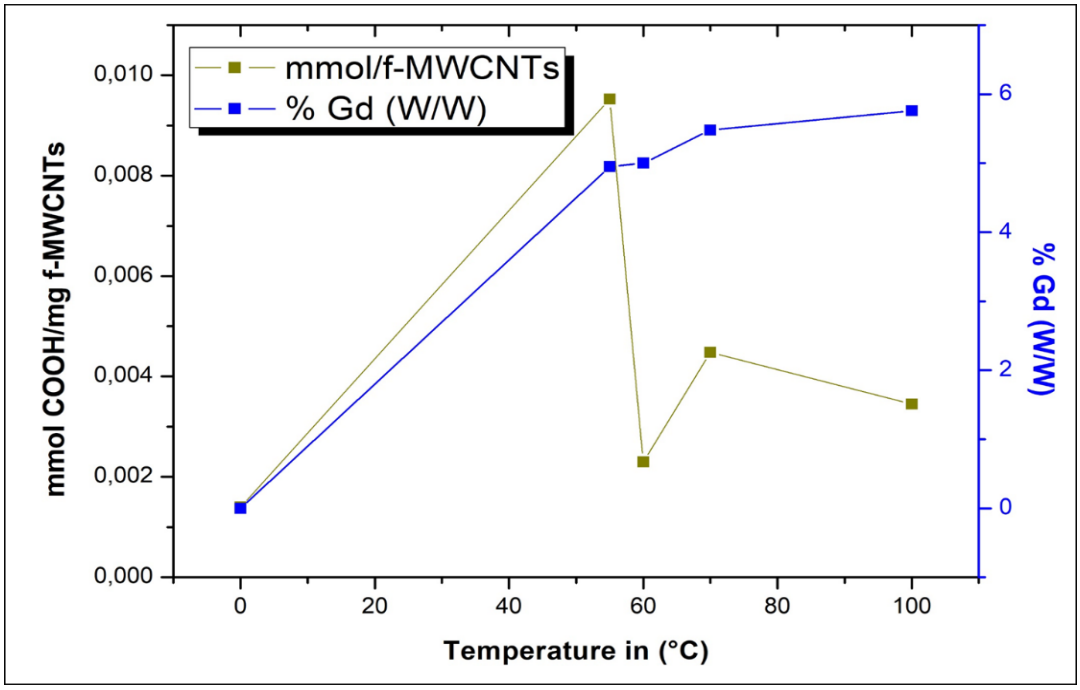

Figure 4. 26: Plotted of Dependence of temperature as function of gadolinium percentage and Carboxylic group per f-MWCNTs against gadolinium percentage.

4.2.5. High Resolution Transmission Electron Microscopy

Morphologies of the sample under study were investigated by HRTEM. The results show that Gd-DTPA complex was randomly dispersed onto the carbon nanotubes. This cannot easily be identify on the surface of carbon nanotubes in the micrographs due to the stoichiometry (1:1) of the reaction. Therefore, the microstructure with spherical shape can be noticeable as shown in Figure 4.27 in the Gd-DTPA-f-MWCNT(55) sample at 0.5 µm magnification. This can be attributed to the higher concentration of carboxylate group which attach the Gadolinium onto the surface of CNTs. Moreover, this will definitely affect the magnetic behavior the sample. Due to the expectation changes on the magnetic environment (delocalized

electrons) and mole concentration of the carboxylic group in the materials under study.

The Pristine sample displays uniform surface on the bundles. This indicates the absence of impurity attached on the outer wall of the carbon nanotubes. Gd-DTPA-f-MWCNTs samples were damages on their surface, which directly indicate efficient modification on the surface of CNTs. The complex molecular center cannot be clearly monitor on the micrographs of all samples. While this can evidently be seen on the Gd-DTPA-f-MWCNT(55) and Gd-DTPA-f-MWCNT(70) compared to Gd-DTPA-f-MWCNT(60) and Gd-DTPA-f-MWCNT(100) samples. HRTEM images show homogenous outer diameter of the Gd-DTPA loaded carbon nanotubes bundles. Whereas the Gd-DTPA-f-MWCNT(70) displayed not identical outer diameter.

It's also demonstrate that preparation condition of functionalization of CNTs affect the length of the Gd-DTPA-f-MWCNT(100). These broken nanotubes have shorter length compared to Gd-DTPA-f-MWCNTs 55, 60, and 70 °C. Increase in temperature destroyed CNTs by reducing the length of the bundles. The HRTEM image of pristine carbon nanotubes and Gd-DTPA-f-MWCNTs are shown in the Figure 4.27.

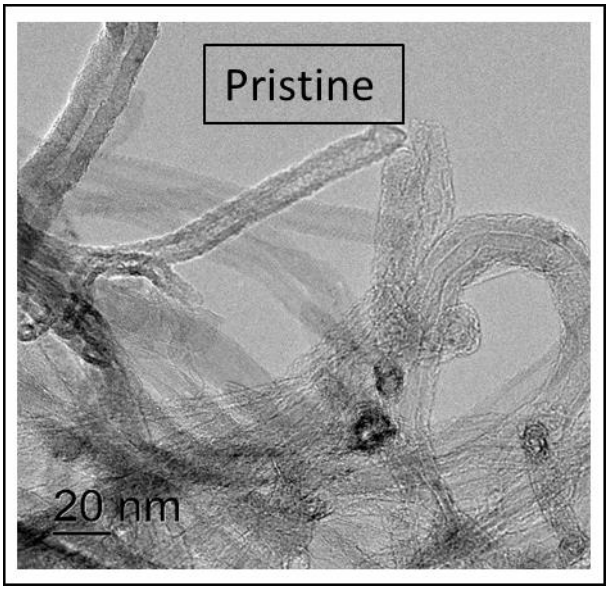

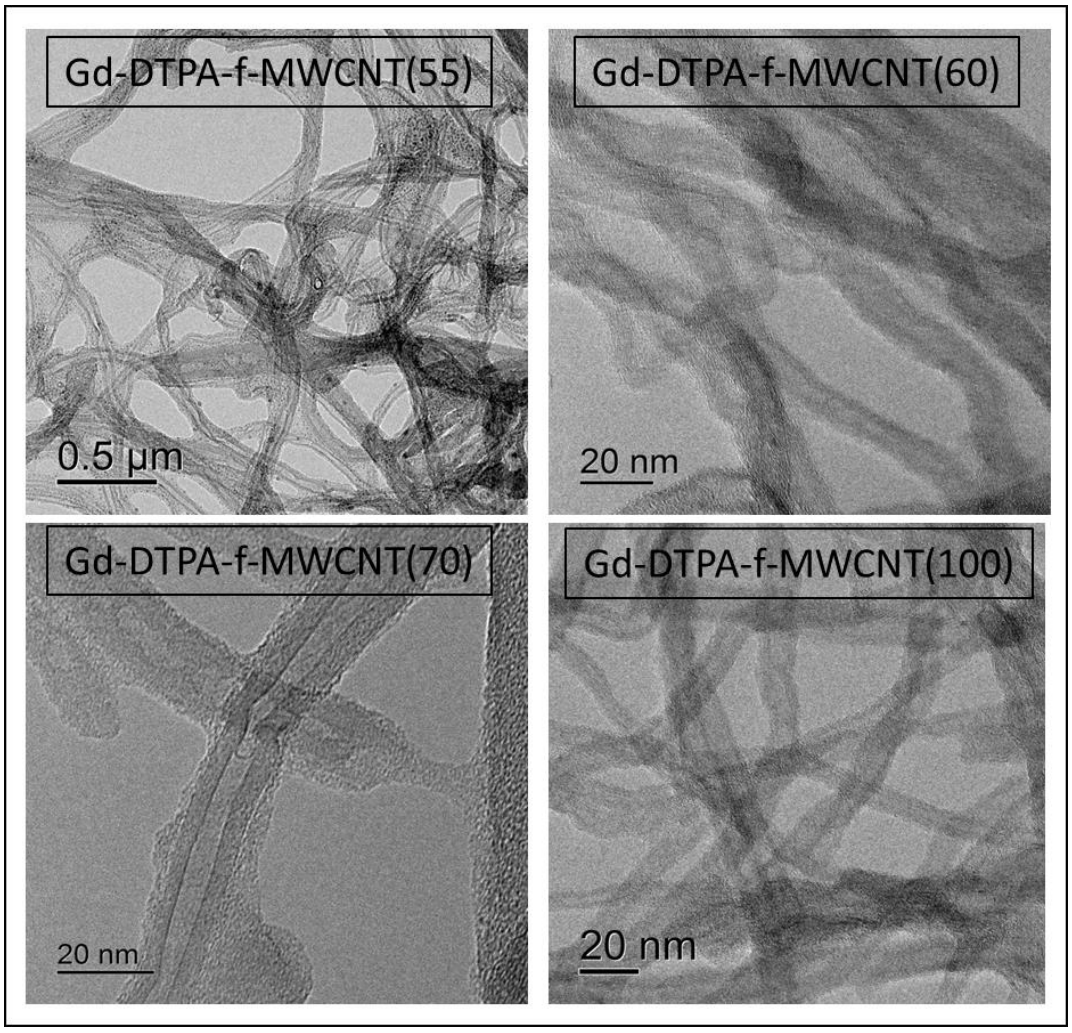

Figure 4. 27: Morphologies images from High-Resolution Transmission electron microscopy of pristine and Gadolinium-DTPA loaded onto multi-walled carbon nanotubes show non uniform coverage of the complex.

4.2.6. Magnetization characteristics of Gd functionalized CNTs

The tailoring of magnetic properties of carbon nanotubes has major implications for various technological applications including MRI contrast agents [131] as well as more niche area applications in spintronics [132]. As shown in previous sections, the synthetic chemistry route used in this investigation has allowed for a more controlled functionalization of multi-walled carbon nanotubes. In the next section of work, it is demonstrated how the degree of functionalization of the nanotubes, and hence the extent to which Gd can be loaded onto the CNTs, modifies or changes the magnetic properties.

Gd functionalized nanotubes have before been synthesized, however until now these studies have always shown a superparamagnetic signature [133, 134, 135]. Superparamagnetism is a phenomenon observable in ferromagnetic nanoscale non-interacting systems. However, the magnetic signatures of the samples used in this study show a clear deviation from what has thus far been reported in literature. As shown in Figure 4.28 and Figure 4.29 below, a clear hysteric behaviour can be seen, this is indicated by a pronounced and temperature dependent coercive field (H_C) as well as magnetic remanence. These features are clear indications of a ferromagnetic character. However, in addition to these observations it is apparent that the magnetic properties show a distinct temperature dependence, this includes a change in slope of the saturation moment, which increases to a point of non-saturation as the temperature decreases. This is an indication that there is a competing magnetic phase different to the ferromagnetism [136]. It is important to note that all samples show same hysteretic behaviors signature at three different temperature. The Gd-DTPA-f-MWCNT(100) sample is represented from Figure 4.28 to Figure 4.31.

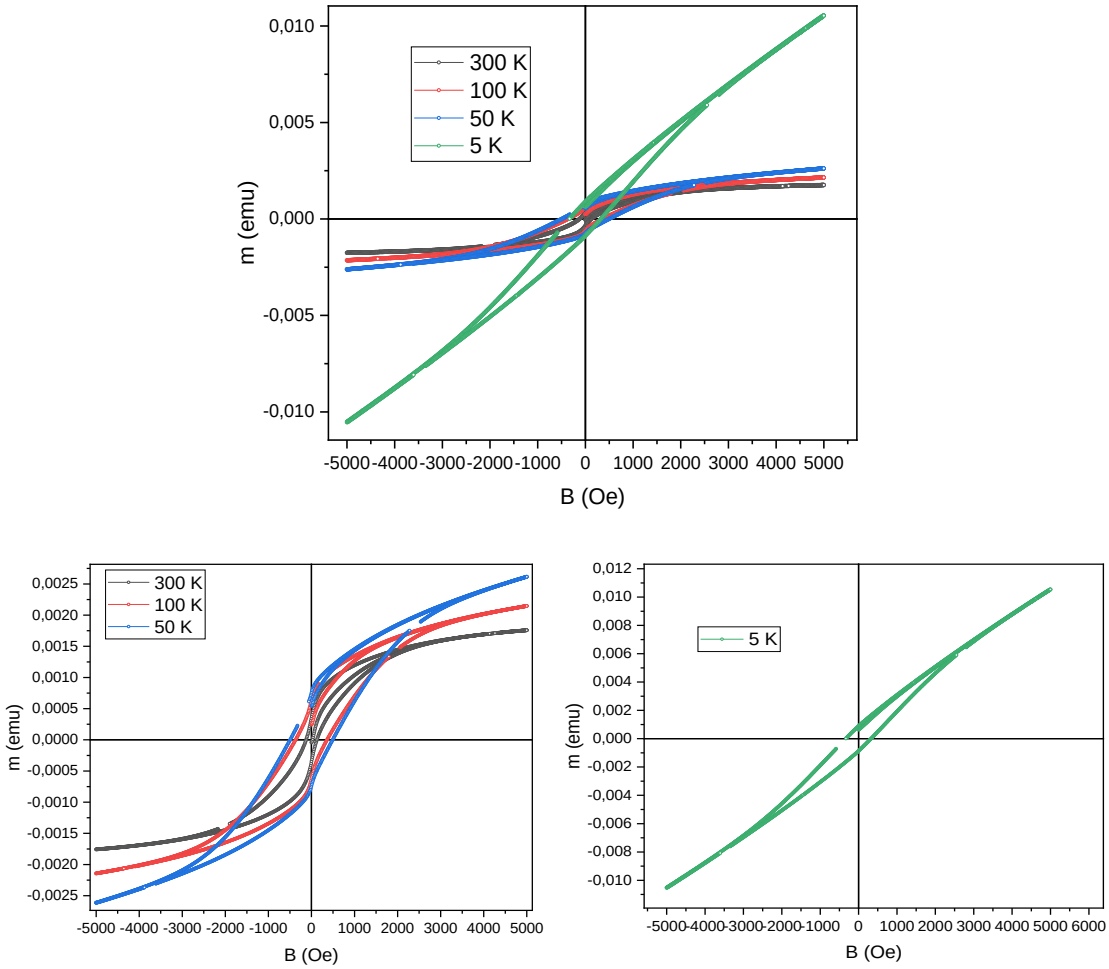

Figure 4. 28: Illustrates Hysteretic behavior of the samples show signatures of a mixed magnetic phase with competition between ferromagnetism and antiferromagnetic ordering. This is evident from the clear hysteresis (ferromagnetic part), as well as the non-saturation as temperature is reduced (evidence for antiferromagnetic).

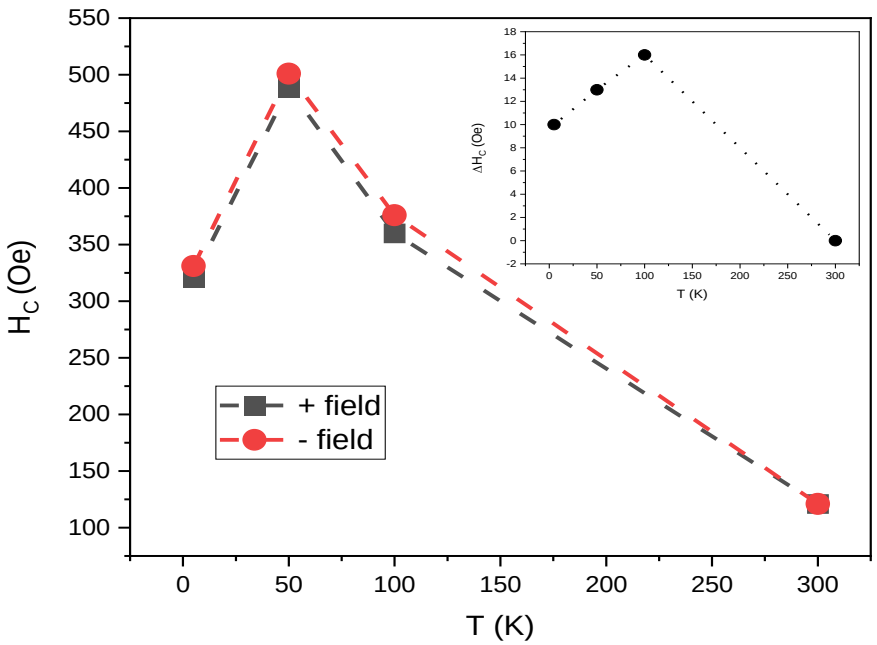

Figure 4. 29: Demonstration of the coercive field of the Gd-functionalized multi walled nanotubes shows a temperature dependence, where it increases as temperature decreases until reaching low temperatures where the magnetic moment diverges after which H_c decreases. A further observation is the slight asymmetry in the coercive field, an indication of exchange bias, thus further supporting the mixed or competing magnetic nature of this material.

Therefore, it is even more inserting that the temperature dependence of the coercive field shows an asymmetric value that increases with decreasing temperature. For a purely ferromagnetic system, this asymmetry is not expected but has however been observed before in system that exhibit exchange bias [137]. Exchange bias is a phenomena that occurs when a system with antiferromagnetic (AFM) and ferromagnetic (FM) domains in contact are cooled through the Neel temperature (with Curie temperature higher than the Néel temperature), which leads to a coupling of the antiferromagnetic and ferromagnetic domains in such a way that an anisotropy or tilting occurs in the ferromagnet. This exchange bias is generally observed in AFM and FM layered systems however is well documented in nanoscale system, they are composed of fine particle with small dimensions where ferromagnetic cores are coated with antiferromagnetic surfaces [137] , as well as in inhomogeneous materials which are composed of multiple random sized AF-FM domain interfaces. Both scenarios can be imagined in the current system which is composed of magnetic ferromagnetic centres distributed across the CNTs surface. The exchange bias is also commonly associated with spin glass systems.

As seen in Figure 4.30, the temperature dependence of the magnetic moment for field cooled as well as zero field cooled measurement (FC and ZFC) no clear blocking temperature can be identified, ruling out the possibility of a purely superparamagnetic scenario, furthermore, when plotting the increase susceptibility as a function of the temperature a pronounced linear region can be observed for much of the data, this linear region can be fitted to the Curie-Weiss law (equation 2.5).

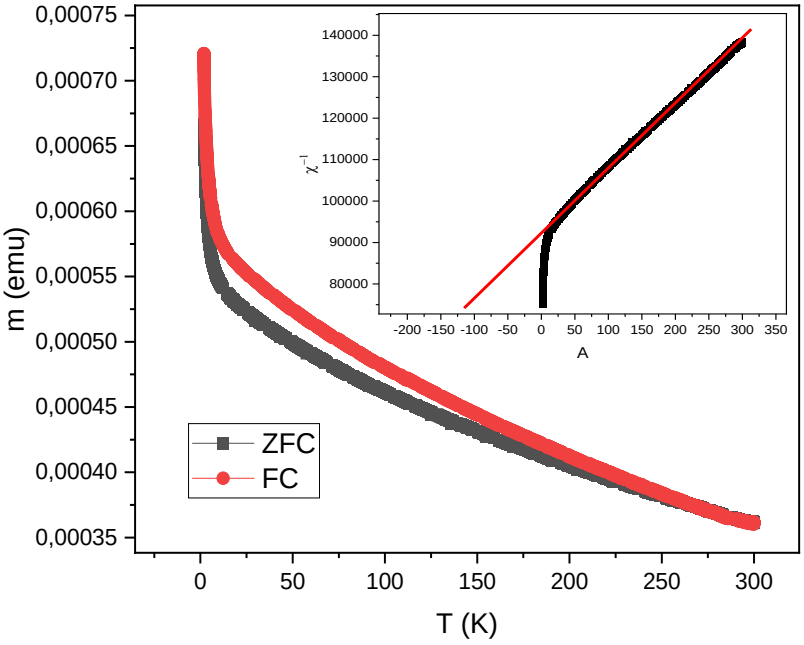

Figure 4. 30: FC and ZFC susceptibility plot of Gd-DTPA-f-MWCNTs showing the temperature dependence of the magnetic moment, the lack of blocking temperature rule out superparamagnetism. The inset shows a plot of the temperature dependence of the inverse susceptibility, the Curie-Weiss law fitted to linear region yields a negative curie-Weiss temperature indicating the presence of antiferromagnetic interaction.

It can be seen that the Curie-Weiss temperatures take on negative value a clear indication that antiferromagnetic coupling exists in the samples. As we are dealing with a nanoscale system, it is necessary to investigate the origin of this mixed or competing magnetic signature. On one hand, we have the ferromagnetic centres of the Gd-DTPA ligand, which are attached to the nanotubes, however it is clear there is a strong coupling between such centres as these are expected to be purely superparamagnetic which is not the case here. As noted above, there is a clear indication of competing magnetic order, this should be mediated by the conducting lattice of the nanotubes and thus the RKKY interaction is most likely [138]. Accordingly, the distance between respective Gd-DTPA ligands would determine the

character, either FM or AFM, and thus it is quite possible to have competing order based just on the random distribution of the Gd-DTPA centres.

In order to further evaluate the nature of such a mixed magnetic phase, we examine the derivative of the hysteresis loops. By plotting the first derivative of the magnetic moment as a function of the applied field, we are able to plot Figures 4.31 (a-d). There the overall character of the hysteresis slope changes as the temperature is decreased. Firstly, at room temperature the system has a pronounced peak centered at zero applied field, as the temperature is lowered, this central peak is reduced and the two-satellite broad peaks increase in area. This trend continues, as the temperature is further lowered, then reaching temperatures below which the moment diverse, the center peak no longer occurs. Following the analysis of [139], such features in the hysteresis can be interpreted as evidence of a mixed competing phase.

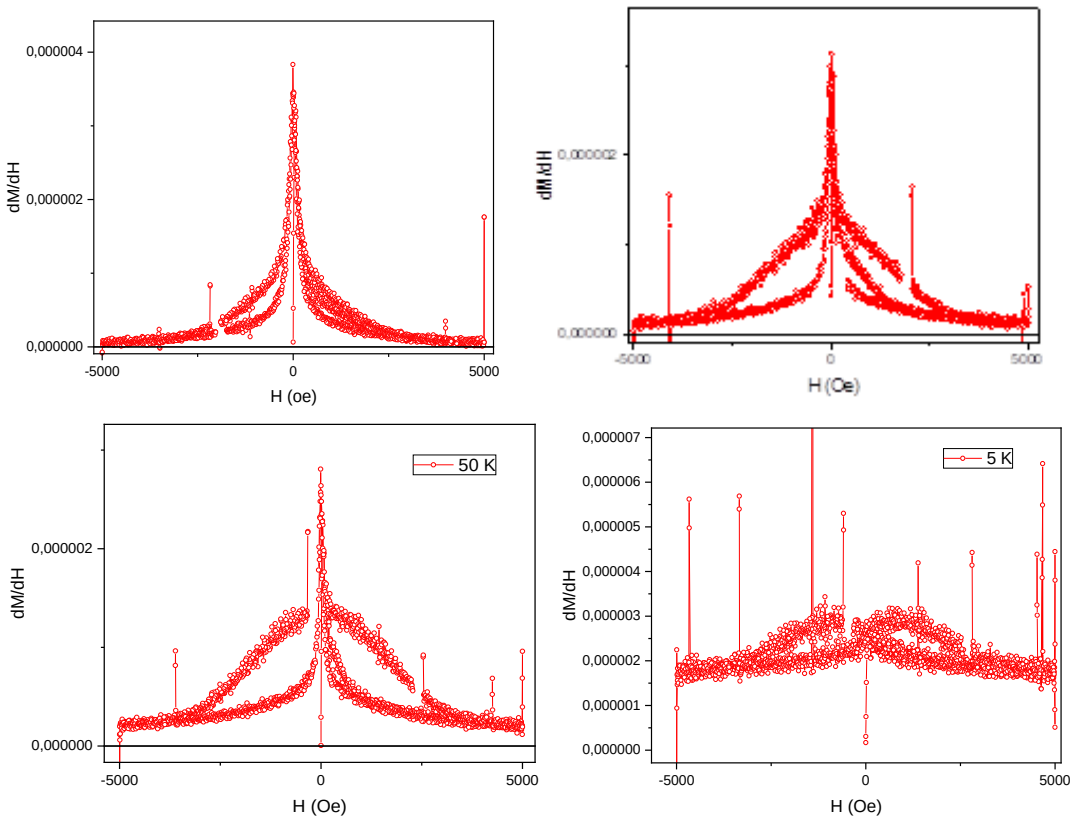

Figure 4. 31: Plot of the first derivative of the magnetic moment as a function of applied field. This plotting procedure allow for the disentanglement of the mixed phase contribution to the magnetic properties, there are two pronounced features as would be expected for a mixed system, this is evident by the sharp central peak at zero field and then the two broader peaks at finite values of applied field. The central peak is diminished as temperature decreases, indicated suppression of the misaligned anti-ferromagnetic character and growth of the ferromagnetic domains.

The central peak being antiferromagnetic whereas the two symmetric side band relating to the ferromagnetic domains. As a weight shift in these peaks occurs as the temperature is lowered, it can be assumed that there is a shift in the dominant type of magnetic domains. The Ferromagnetic bands increased in size confirmed by the increase in coercive field with decreasing temperature (Figure 4.29). In order to qualitatively analyze this system, we rely on the recent deconvolution scheme presented in [139].

To investigate how the magnetic character can be modified across the samples used in this study, a comparative investigation into the hysteretic behavior is conducted. This is carried out at 300 K. As expected, there is a significant difference of the magnetic response for samples synthesized at different reaction temperatures. As shown in Figure 4.32, upon an increase in the reaction temperature the large field response shows a wide variation in slope. This is explained when considering that the unfunctionalized nanotubes are intrinsically diamagnetic and predicted to have a large negative slope [140]. As the reaction temperature is increased this negative slope is steadily increased until a positive slope is observed for reaction temperature 100 ^{o}C. The rise in temperature makes CNTs unstable and braking down the structure of the complex with increases reaction time. Which gives birth to few diamagnetic material in the sample. The FT-IR result has shown that the rise in the reaction time and temperature destroy progressively carboxylic group by showing a large band between 3200 – 3500 cm^{-1} which resulting of stretching vibration bond of hydroxyl group in the sample. This can be explained in terms of the increase in degree of functionalization across the samples as the temperature decrease with increase reaction time. As more functional groups are added to the nanotubes, the diamagnetic character, which is a result of the conduction electrons, is degraded. This is because the addition of functional groups disrupts the pi-conduction bands. This in turn means that, as expected, higher degree of functionalization or attachment of the Gd-DTPA ligand leads to a stronger spin interaction. This is due to a larger dispersion and reduction of the distance between spin centers.

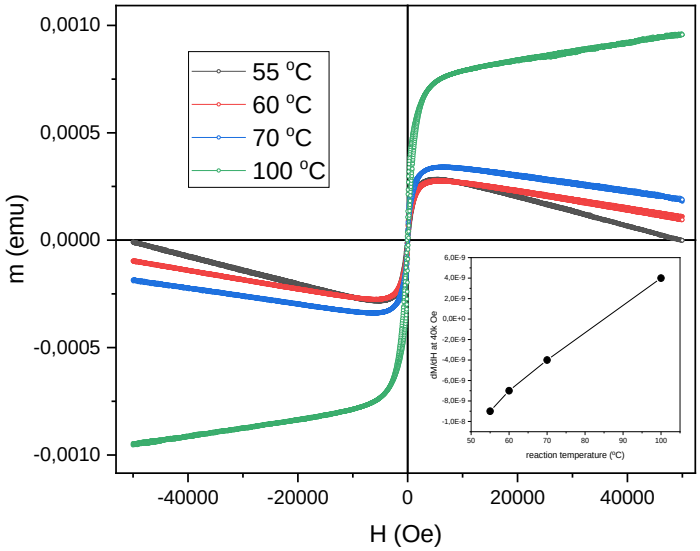

Figure 4. 32: Comparison of magnetic hysteresis for the samples synthesized at various temperature range. The intrinsic diamagnetic response of the nanotubes is reduced with increasing temperature, indicating disruption of the conduction pi-electron network as more Gd-DTPA is attached to the nanotubes. The inset shows the temperature dependence of the slope of the large field part, the increase in slope indicate the samples move away from diamagnetic to a more ferromagnetic system with increasing temperature.

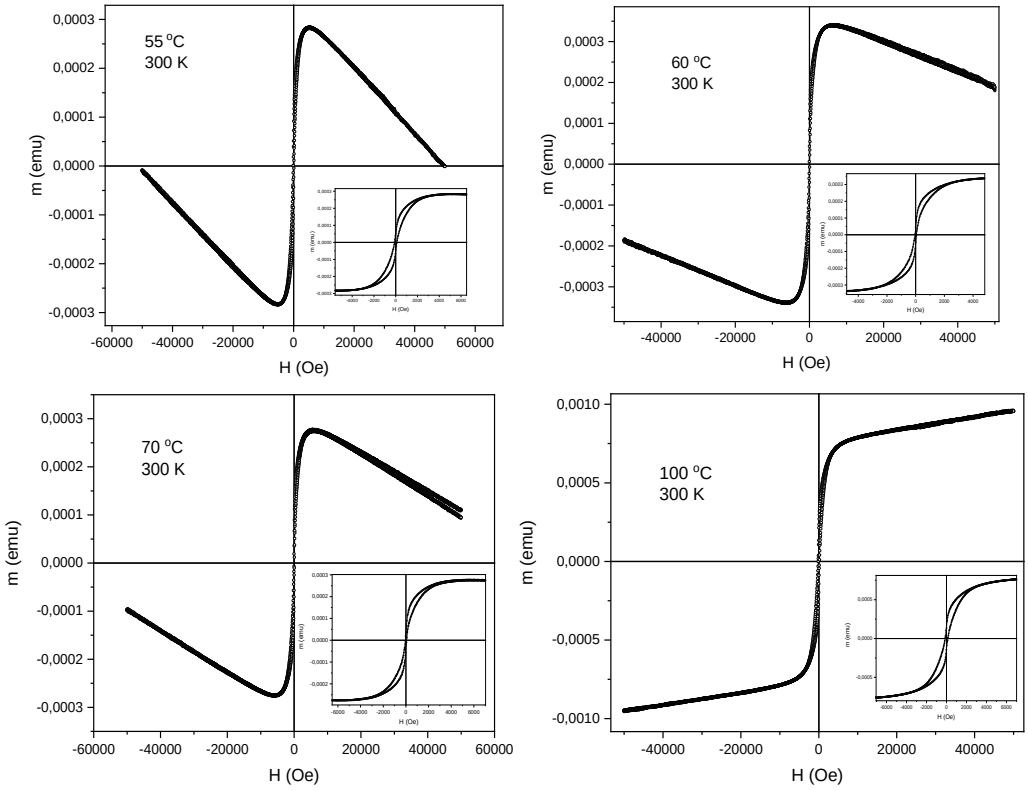

Figure 4. 33: Magnetic hysteresis across the samples synthesized at various reaction temperatures indicates that as the reaction temperature increases, the system moves away from a diamagnetic character typical for intrinsic nanotubes. This is evident by the slope, also we see that the low field region has a pronounced variation in the coercive field.

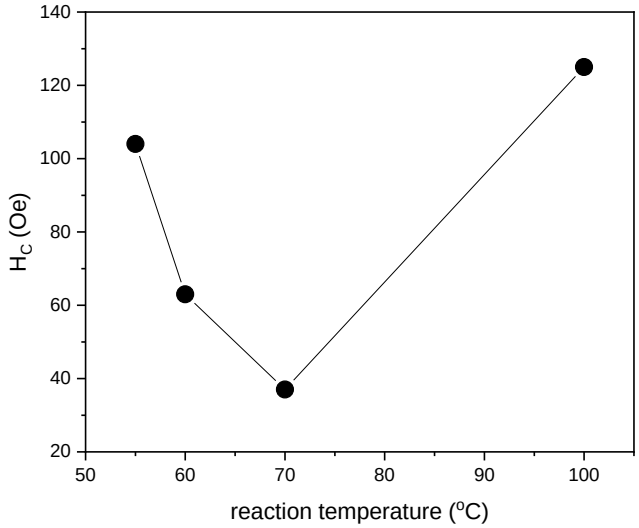

Figure 4. 34: Variation between coercive field and reaction temperature. As reaction temperature increases the distribution of the Gd-DTPA ligands increases and leads to a disruption of the ferromagnetic character, this trend reaches a minimum for the 70 C sample, upon reactions at higher temperatures the hysteresis increases significantly indicating perhaps that additional loading results on the presence of hydroxyl group, also in large coupling between spin centers, resulting in large ferromagnetic response.

The reduction of the diamagnetic CNT contribution also indicates that the conduction electrons are themselves then mediating the interaction between spin centers, as would be required for the RKKY mechanism. As before, it is important to examine the low field region across the samples as well. As shown in Figure 4.33, the hysteresis of individual reaction temperature samples are plotted, each plot shows the low field section as an inset. As can be seen here, the individual reaction temperature all has some level of hysteretic behavior, an indication of Gd-DTPA ligand attachment at all temperatures. What is interesting to note, is the variation of the H_c field across the samples. This is plotted in Figure 4.34, where we see an initial decrease in the coercive field until reaching a minimum for sample 70 °C, after that a steep increase for the last sample at 100 °C. The decrease in the coercive field as the attachment of the Gd-DTPA increase is an indication that the ferromagnetic domains is being disrupted, most likely due to increased disorder, a closer distribution of the dispersion and thus an enhanced RKKY interaction mediated by the conduction electrons.

Chapter 5

Graphene oxide and reduce graphene oxide

This chapter will be discuss the information about different characterization technique applied on the graphene materials. The analysis procedures, discussion and interpretation of the results are conferred in this chapter. It also deals with the procedure attached of Gd-DTPA complex molecular onto graphene oxide, as well as, reduced graphene oxide. In addition, It also shows the results gained from the different measurements at room and low temperature using graphene oxide (GO) and reduced graphene oxide (rGO) materials under study.

5.1. Graphene oxide

This part depicts the characterization of the following techniques: Fourier Transform Infra-Red spectroscopy; Raman spectroscopy; Scanning Electron Microscopy; Atomic force microscopy; Zeta potential and Acid-base titration obtained with graphene oxide.

5.1.1. FT-IR spectroscopy

Graphene oxide synthesized from graphite powder was carry out using modified Hummers method. FT-IR measurement of graphene oxide powder was measured at room temperature. This sample was not in binder with KBr matrix and not in pellets. FT-IR data collected shows that absorption bond of –COOH group is assigned at the peak with the wavenumber 1720 cm^{-1}. Neither graphene nor graphite powder show any peak at this wavenumber which is in agreement with the result reported by D. Bikiaris *et al.* [118]. A large peak is observed at 1153 cm^{-1} wavelength is related to stretching vibration of C-O bonds. Moreover,

it should be mentioned that the peak, which is appeared in the region of 1200 cm^{-1} assigned to stretch vibration of C-OH (carboxylic acid) group [141].

Figure 5.1 gives FT-IR spectra of single layer graphene oxide and graphite powder. Large change can be observed between graphene oxide and graphite or graphene FT-IR spectra. This resulting from new organic group that have been successfully introduced onto surface of graphene single layer. Furthermore, the analysis quantitative of the acid in the sample was done by acid-base titration using Boehm method.

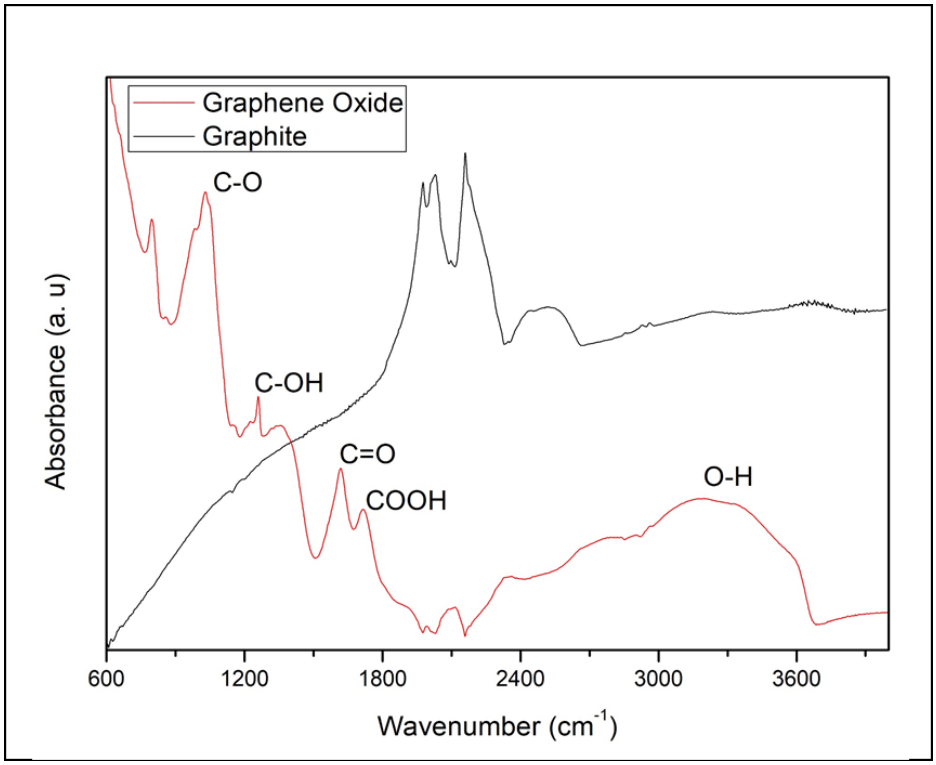

Figure 5. 1: FT-IR spectra of single layer graphene oxide and graphite powder.

5.1.2. Titration of Graphene Oxide

Acid-base titration used to determine surface degree of functionalization of the graphene oxide. Similar concentration of hydrochloric acid HCl 0.10 M and sodium Hydroxide NaOH 0.10 M were prepare in this case to quantify carboxylic group introduce on surface of graphene single layer.

Experimentally, 5 mg graphene oxide added 25 ml NaOH 0.1 M. Sonicated for 2 hours at room temperature and filtrated with 0.22 µm membrane filter of diameter 47 mm. A volume of 19 ml of filtrated solution added exactly 19 ml of HCl 0.1 M. Stirred for 5 min and further filtrate to remove graphene salt formed. The excess of NaOH titrated with HCl 0.1 M up to neutral point pH 7. This titration result shows that calculated concentration of carboxylic group is found about 8.2 x 10^{-2} mmol COOH per mg of GO. While the highest concentration of f-MWCNT (55 °C) was found 9.523 x 10^{-3} mmol COOH per mg. This shows a strong agreement with FT-IR indicating the typical absorption band of carboxylic at 1720 cm^{-1}.

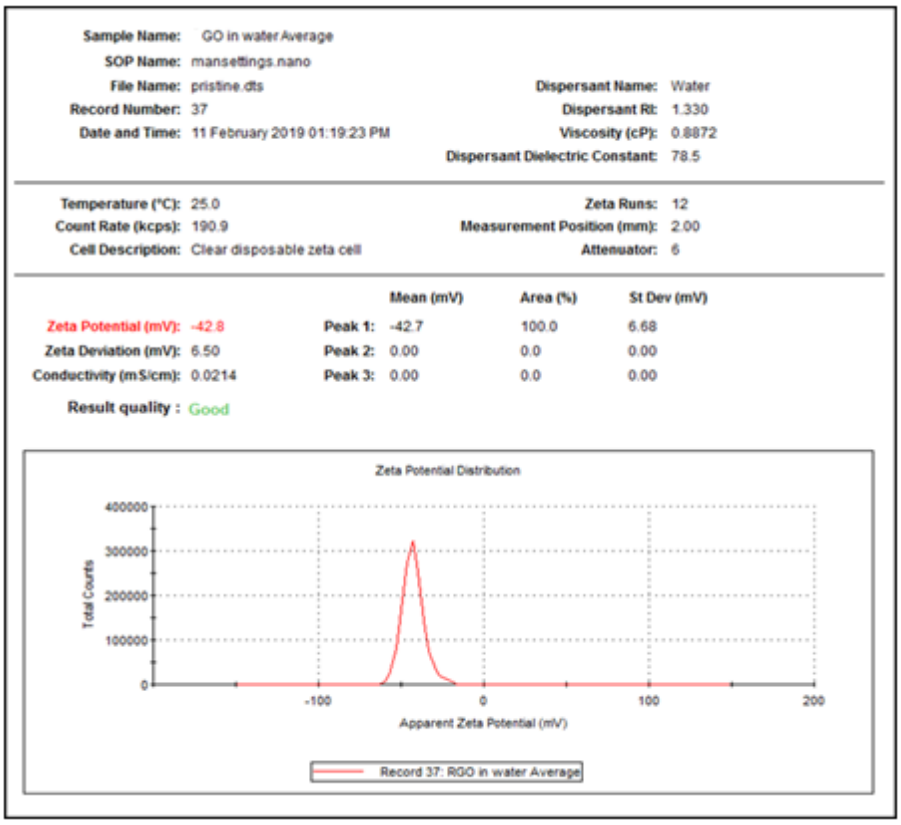

Figure 5. 2: Average spectra from Zeta potential analysis of graphene oxide (GO) sample

That can be also supported by the Zeta potential analysis, which gives a value of – 42.8 ± 0.05 mV average voltage as can be seen in Figure 5.2 above. Experimentally, GO was dissolved in water and Zeta potential data was collected at room temperature.

Raman spectrum of the graphene oxide was compared with the magnetic molecular complex Gd-DPTA loaded onto the surface of the graphene oxide GO-Gd-DTPA. Chemical oxidation of graphite using modified Hummers method which resulting of insertion of the new organic group in the graphene sheet. This increases the disorder in the *D* bands in the Raman spectrum as shown in the next section 5.2. The carboxylic group can be converted to hydroxyl via reduction. Moreover, this allows chemical bond between carbon in the graphene oxide to be rearranged and produced so called reduced graphene oxide. However, it is necessary to react graphene oxide and reduced graphene oxide with magnetic molecule complex to study their changes in term of magnetic behavior.

5.2. Gd-DTPA loaded onto surface of Graphene oxide

This portion will deal with the characterization of the following techniques: Fourier Transform Infra-Red spectroscopy; Raman spectroscopy; Induced Coupled Plasma Optical Emission Spectroscopy; High Resolution Transmission Electron Microscopy, and electronic transport with magnetic measurement.

5.2.1. FT-IR spectroscopy

The inserts of Figure 5.3 gives the Gd-DTPA loading into graphene oxide GO-Gd-DTPA, comparing with pure graphene oxide synthesized via modified hummers method. FT-IR results have shown that the complex chelate molecular (Gd-DTPA) was successfully linked with the graphene oxide materials after 24 hours of the chemical reaction in water at the temperature of 32 °C. The percentage of Gadolinium determined in the GO-Gd-DTPA sample was 8.01 ± 0.02 % (w/w) by Induced Coupled Plasma-Optical Emission spectrometry.

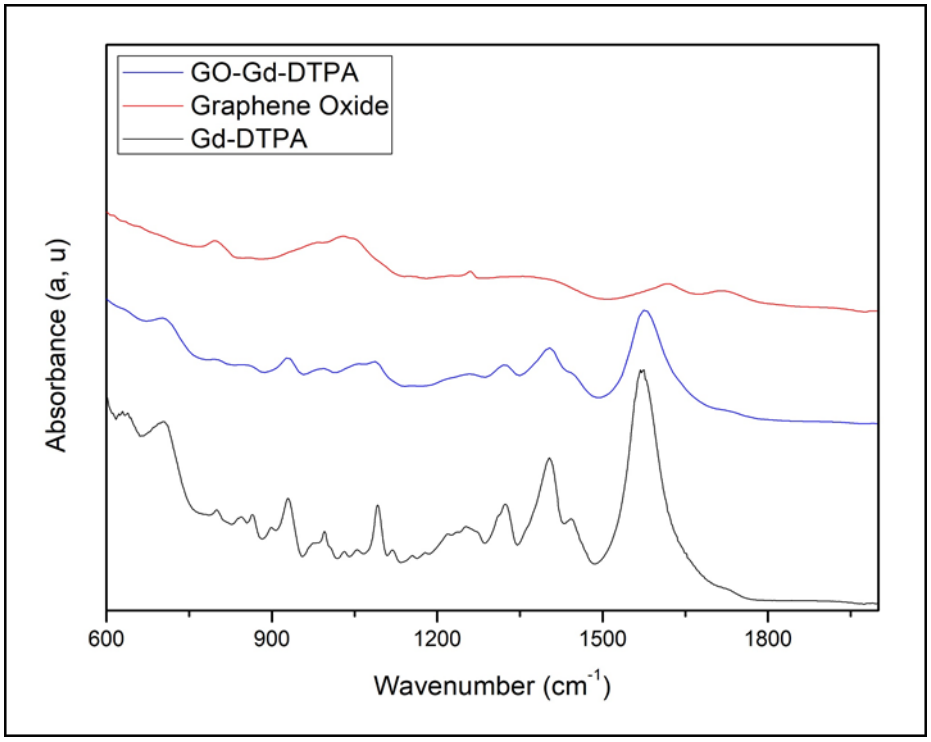

Figure 5. 3: FT-IR spectra of graphene oxide (GO), GO-Gd-DTPA and Gd-DTPA taken in the range from 600 cm^{-1} to 1800 cm^{-1} wavenumber.

FT-IR Data collected of GO-Gd-DTPA shows a typical peak in the wavenumber in the range from 1200 cm^{-1} to 1780 cm^{-1} indicated the presence of carbonyl group specially C-N stretching vibrations. The absorption bond at 633 cm^{-1} and 695 cm^{-1} are assigned at the stretching vibration of the Gd-O and Gd-N, respectively. The organic function C-O and C=O stretching vibrations are represented by the peaks in the range of 110 cm^{-1} and 1660 cm^{-1}, respectively.

Moreover, the presence of the new peak at the position of 1170 cm^{-1} reveals the stretching vibration of the hydroxyl group of graphene oxide with gadolinium central ion. The proof of success of this loading is given in Figure 5.3. By comparing the GO-Gd-DTPA with pure complex molecule Gd-DTPA spectrum. Raman data collected at room temperature in the next section confirms it also.

5.2.2. Raman spectroscopy

Figure 5.4 displays Raman spectrum of graphene oxide. The Stokes phonon energy shift caused by laser excitation (514 nm) creates two main peaks *D* and *G* bands estimate at 1343.7 cm^{-1} and 1587.4 cm^{-1}, respectively. The intensity ratio I_D/I_G = 0.96 ± 0.004 of the graphene oxide increases to the value of I_D/I_G = 1.558 ± 0.003 in the GO-Gd-DTPA sample. This increment in term of intensity ration of the *D* and *G* bands resulting of disorder when the magnetic molecule Gd-DTPA loaded on the surface of graphene oxide. In many literature Raman intensity increases with the level of disorder in the structure of the material. This results show that greater value of intensity ratio I_D/I_G = 1.558 ± 0.003 indicates rupture of sp^2 bond carbon atom to form sp^3 hybridized which justified the surface modification of graphene single layered. In addition, the images of the GO-Gd-DTPA sample are shown on the Figure 5.4. It seems appear two region, which are black and light region. This can be assume resulting from the excitation of electron of gadolinium in the presence of the Laser beam of 514 nm wavenumber. This excitation can be confirm in future by Photo-luminescence spectroscopy.

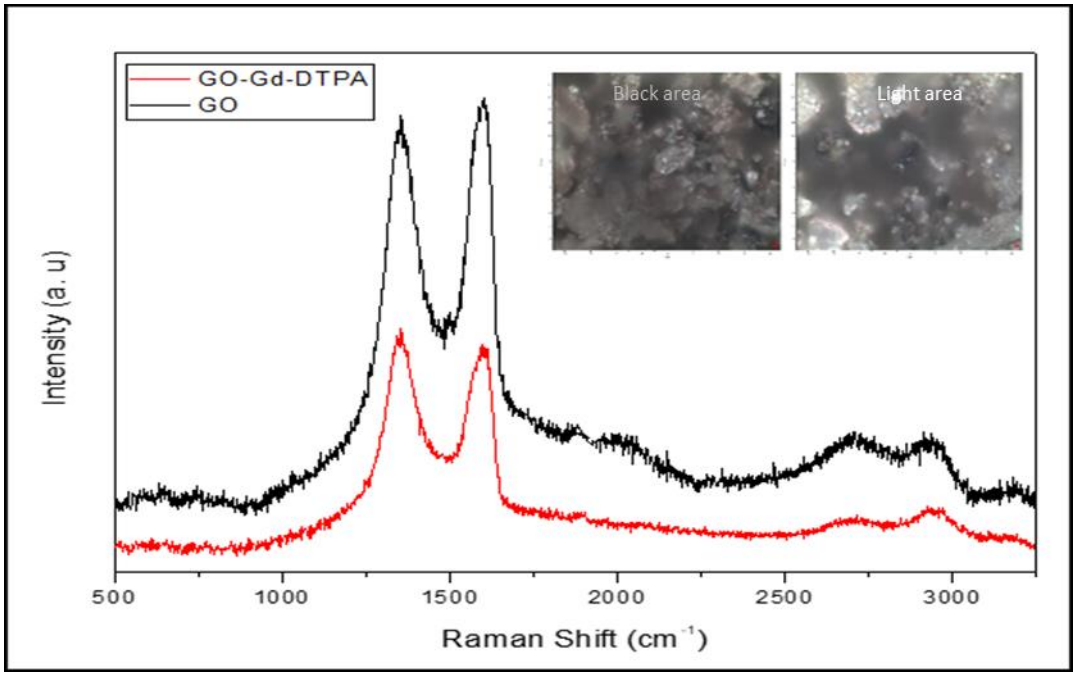

Figure 5. 4: Typical Raman spectra for a single-layer graphene oxide in comparison with GO-Gd-DTPA material using a 514 nm excitation laser. Raman spectra taken in the range from 50 cm^{-1} to 3500 cm^{-1}.

Although the graphene can be identified by the position and shape of its *G* (1580 cm^{-1}) and 2*D* (2690 cm^{-1}) peaks. While graphite powder can be seen at 1550 cm^{-1} peak position which are not revealed in the graphene oxide material under study. Moreover, the result shows also that nature of graphene single layered was not destroyed ever thought chemical modification have been successfully done on the graphene sheet. The variation of the relative intensities of the *G* band (E_{2g} mode of sp^2 carbon) and *D* band (symmetry A_{1g} mode) in the Raman spectrum of GO-Gd-DTPA reveals the change of electronic conjugation states [142]. It was found that the *D* band intensity increases significantly resulting to large out-of-plane vibrational A_{1g} mode attributed to the structural defect related to GO-Gd-DTPA material. The second order of the Raman spectrum, demonstrates higher value of width broadening of the *D* and *G* bands observed on the Gd-DTPA loaded onto graphene oxide GO-Gd-DTPA sample. Deconvolution pattern of the Raman spectra as depicted in Figure 5.5, evaluating the area percentage of *D* and *G* bands in graphene oxide and GO-Gd-DTPA materials.

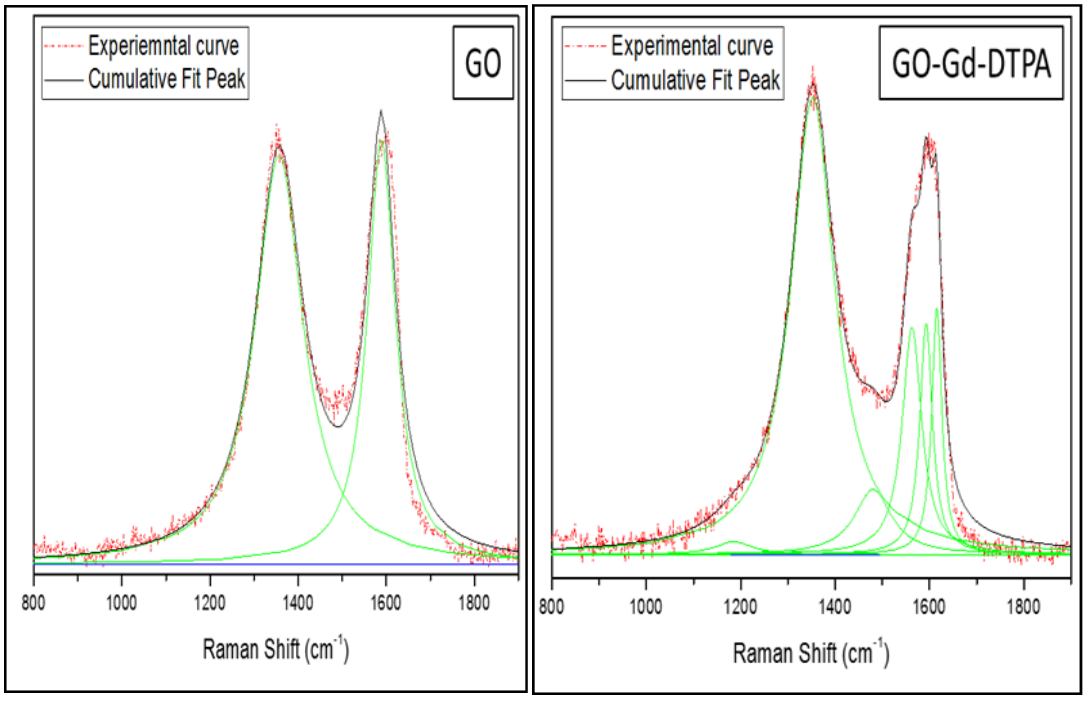

Figure 5. 5: Deconvolution of Raman spectra for a single-layer graphene oxide in comparison with GO-Gd-DTPA material using a 514 nm excitation laser. It was taken in the range from 800 cm^{-1} to 1900 cm^{-1}.

Regarding the deconvolution model of the Raman spectrum of loaded sample with Gd-DTPA. It was found that the new satellite bands such as S, Dv, GI and Gr bands were necessary need to obtain the best fit of the experimental data characteristic of the GO-Gd-DTPA material. The rupture of aromaticity upon chemical reaction leads to the formation of smaller sp^2 domains that are confined by sp^3 bonds [143] and have dimension comparable to polycyclic aromatic hydrocarbons molecules. More extended covalent functionalization can also introduce polyene-like structures. Although, Raman spectra of polycyclic aromatic hydrocarbons always showed bands near 1250 and/or 1400 cm^{-1} , with variations in the position and relative intensity depending on the molecular size and symmetry, as well as, one peak at around 1600 cm^{-1} [120, 125]. GO-Gd-DTPA sample required an addition of two bands S and GI bands to obtain a better curve fitting. The fingerprints of polyacetylene in Raman studies of carbon material [126]. Therefore, it is resulting from the presence of magnetic ligand Gd-DTPA in the materials under study. However, the presence of the satellite bands, in particular the Gv (G band Valley) is due to the presence of DTPA in the sample.

It is evident that 2D band combines the area fit of *D* band. Therefore, if the *D* band is high, indicating more sp^2 carbon converted to sp^3 carbon in the material [143]. The increase in FWHM in the *G* band also indicates more disorder in the materials. That confirmed a large modification onto the surface of single graphene sheet sample. Which is supported FT-IR spectrum of graphene oxide showing a feature that is resulting from surface modification of graphene sheet. The changed on the Raman shift can be observed on the GO-Gd-DTPA compared to GO samples. Which shifted 27 cm^{-1} more compare to graphene oxide materials.

5.3. Reduced Graphene oxide

This slice will be showing the characterization of the following techniques: Fourier Transform Infra-Red spectroscopy; UV-visible spectroscopy; Raman spectroscopy; High Resolution Transmission Electron Microscopy; Atomic force microscopy and Acid-base titration data collected using reduced graphene oxide.

5.3.1. FT-IR and UV-visible spectroscopy

Reduced Graphene oxide synthesized by the reduction of graphene oxide using L-ascorbic acid. FT-IR data of reduced graphene oxide powder was measured at room temperature. The data collected shows that absorption bond of –COOH group that is assigned for graphene oxide at the peak position 1720 cm^{-1} wavenumber that is disappearing with increasing reduction reaction time. A large peak is observed after 3600 cm^{-1} wavelength is related to stretching vibration of O-H bonds. Which can be consider coming from the conversion of C=O into hydroxyl group. This conversion is occasioning low solubility of the reduced graphene oxide in certain solvent like water. Figure 5.6 gives FT-IR spectra of single layer graphene oxide and reduced graphene oxide.

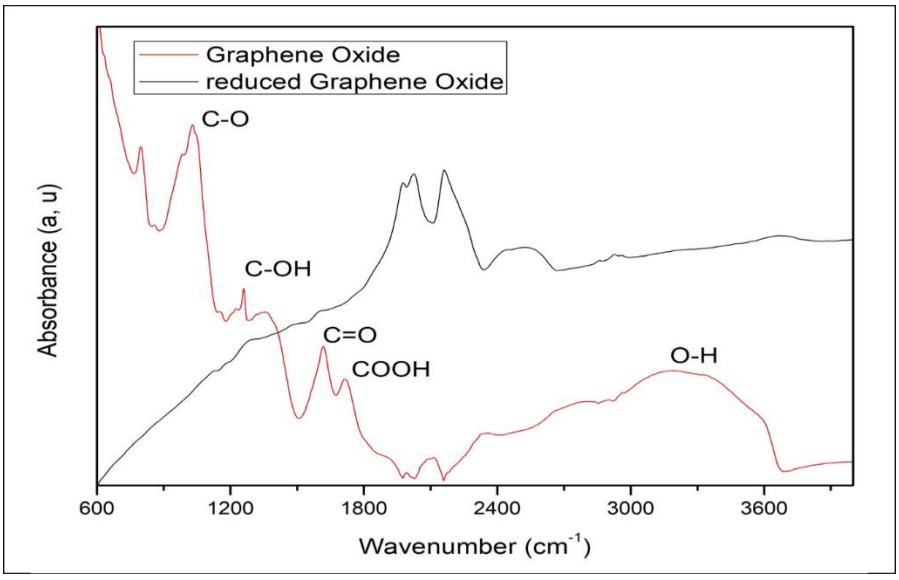

Figure 5. 6: Plotted FT-IR spectra of single layer graphene oxide and reduced graphene oxide.

Enormous change can be observed between graphene oxide and reduced graphene oxide FT-IR spectra. This resulting from new organic group that have been successfully reduced under influence of L-ascorbic acid onto surface of graphene oxide single layer. This afford to reduced graphene oxide similar property closed to single layer graphene due to the rearrangement of chemical bonds. The inserts of Figure 5.7 gives the reduction progression of GO gradually reduced to rGO in water at room temperature.

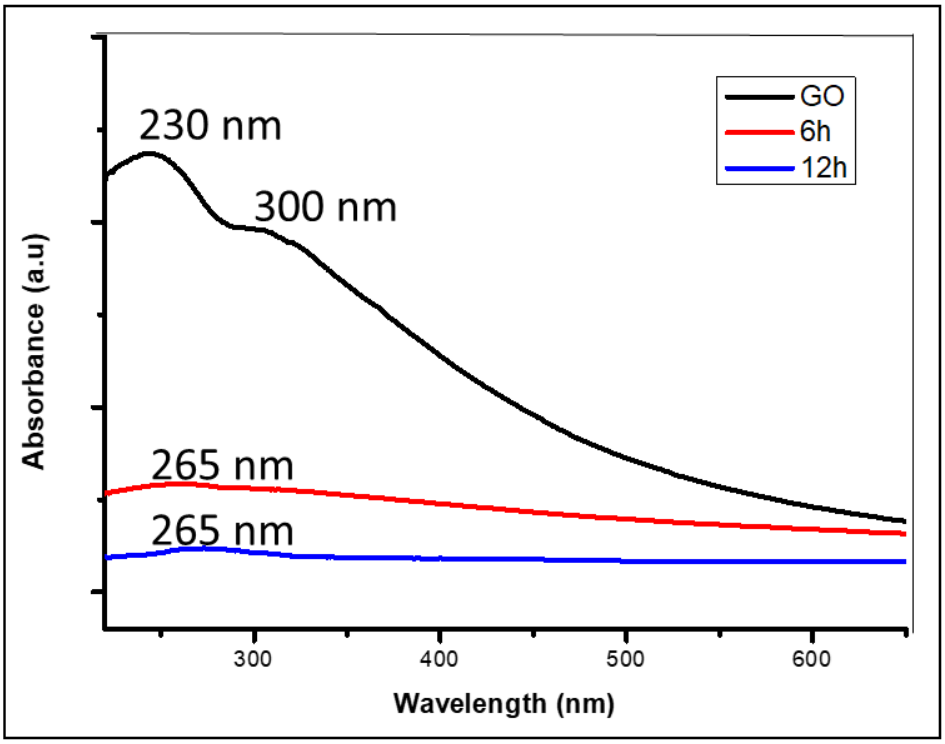

Figure 5. 7: UV-vis spectra of GO aqueous dispersions before and after being reduced for 6 hours and 12 hours.

This was monitor with UV-visible. The reduction of GO was performed using L-ascorbic acid in water at room temperature. The reduction progression of GO was successfully confirmed by UV-visible as shown in Figure 5.7. The peak at the position 230 nm and 300 nm are typically GO peak, decreasing gradually with reaction time. Meanwhile, a characteristic absorption peak of reduced graphene oxide appears at 264 nm, which can be observed after 6 hours and 12 hours reduction time.

The quantification of the carboxylic group in the samples reduced in 12 hours was done by acid - base titration is given in details in the next section.

5.3.2. Acid-Base Titration of Reduced Graphene Oxide

Acid-base titration used to determine surface degree of functionalization in reduced graphene oxide. In this case, a similar concentration of hydrochloric acid HCl 0.001 M and sodium Hydroxide NaOH 0.001 M. those aqueous solution were prepare to quantify the remaining carboxylic group left on surface of graphene single layer. After GO being reduced via L-ascorbic acid for 12 hours.

The rGO titration result shows that calculated concentration of carboxylic group is found to be 7.5 x 10^{-4} mmol COOH per mg of rGO. This result shows a strong agreement with FT-IR spectrum which did not reveal the presence of the typical absorption band of carboxylic at 1720 cm^{-1}. L-ascorbic reduced the concentration of acid and converted them into hydroxyl group or covalent C-C bond. This was confirmed once more in the FI-IR spectra showing large band between 3000 cm^{-1} to 3700 cm^{-1} wavenumber. Moreover, it can also be supported by the Raman spectra, which gives a value of *D* and *G* bands to be nearly similar to pure single layered graphene oxide.

5.4. Gd-DTPA loaded into surface of Reduced Graphene Oxide

This segment will be dealing with the characterization of the following techniques: Fourier Transform Infra-Red spectroscopy; Raman spectroscopy; Induced Coupled Plasma Optical Emission Spectroscopy; High Resolution Transmission Electron Microscopy and electronic transport with magnetic measurement.

5.4.1. FT-IR spectroscopy

FI-IR spectrum Gd-DTPA loaded onto reduced graphene oxide were collected at were measured at room temperature. The significant different observed in the range from 600 cm^{-1} to 1784 cm^{-1} proved that Gd-DTPA was succefully attached on the functional group on the surface of reduced graphene oxide. This is displayed on the top-right in Figure 5.8. However, the absorption bond at 633 cm^{-1} and 695 cm^{-1} are assigned at the stretching vibration of the Gd-O and Gd-N, respectively.

It can be seen that the shift in the peak appeared in the range of the wavenumber of 1200 cm^{-1} to 1784 cm^{-1} are typically indicate the great change in the carbonyl environment. Therefore, the peaks positioned at 2860 cm^{-1} and 2960 cm^{-1} are due to C-H stretching vibration bonds in the sample [141].

The peaks observed at the position 1070 cm^{-1} is characteristic peak of CH_2 stretch vibration which can be consider related to reduction of the C-O to CH_2. Figure 5.8 gives FT-IR spectra of rGO-Gd-DTPA and rGO with baseline correction of the sample. It is also displayed zooming part that indicated huge changes in the surroundings of the carbonyl.

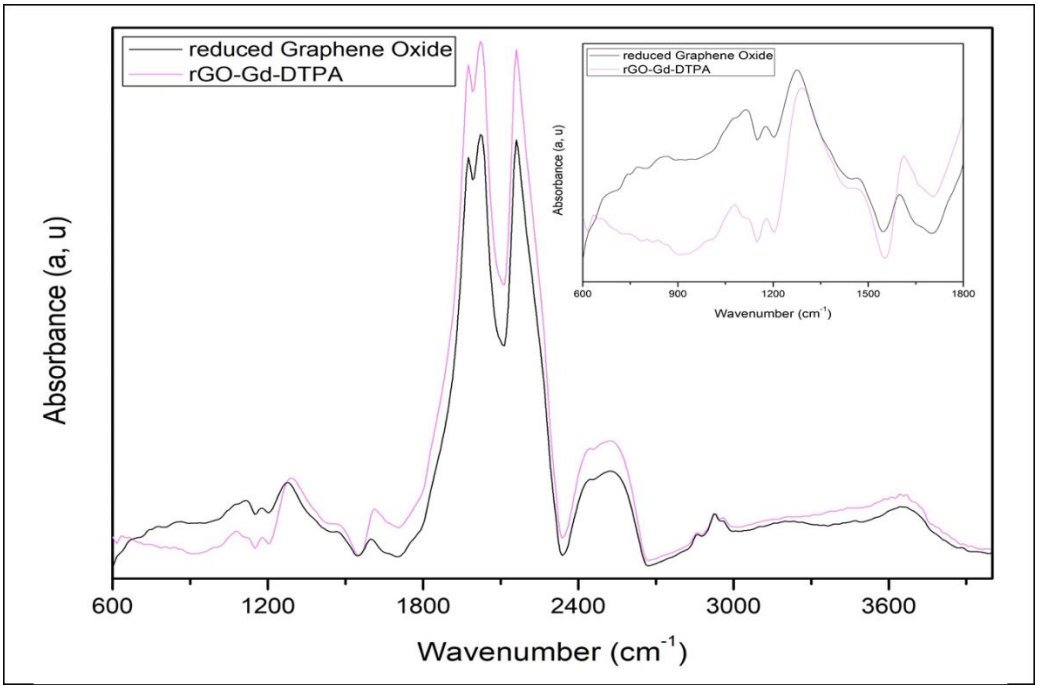

Figure 5. 8: FT-IR spectra of rGO-Gd-DTPA and rGO with data baseline correction.

Further, the percentage of gadolinium in this rGO-Gd-DTPA sample was determine by inductively coupled plasma-optical emission technique. Samples were injected into a radiofrequency (RF) induced argon plasma using one of the nebulizers. Sample sprayed reach the plasma and is rapidly dried, vaporized and excited by collisional excitation. With aid of a lens, the results was collected in the selector device. The weight percentage of gadolinium was found 1.16 ± 0.02 % in the rGO-Gd-DTPA sample. Which was obtained after 12 hours reduction times via L-ascorbic acid. The cation Gd^{3+} shows strong interaction with COO^{-} and tertiary Nitrogen of DTPA molecule.

5.4.2. Raman spectroscopy

Compilation of the characteristic Raman data collected for rGO-Gd-DTPA and rGO materials shown the large changes on *D* and *G* phonon peaks. This results show greater similarity in intensity ratio $I_D/I_G = 1.283 \pm 0.003$ value. It is luckily displayed the broadening in *D* and *G* bands in the spectral pattern resulting of the rupture sp^2 bond carbon atom to form sp^3 hybridized. It was found that the *D* band intensity increases significantly as shown in Figure 5.9, resulting to large out-of-plane vibrational A_{1g} mode attributed to the structural defect related to rGO-Gd-DTPA material. In addition, it can be seen in the Raman spectra of GO in comparison with rGO and rGO-Gd-DTPA material. This can be consider originated from the loading of Gd-DTPA on the surface of reduced graphene oxide and the creation of sp^3 carbon in the material.

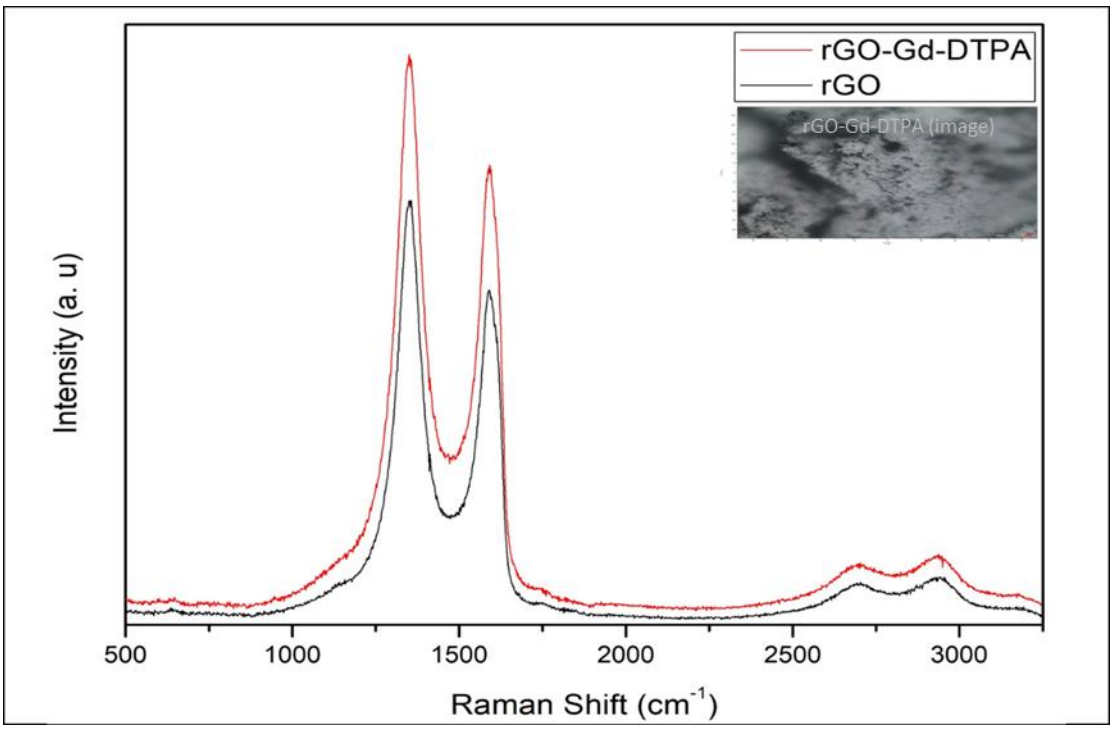

Figure 5. 9: Typical Raman spectra for a single-layer reduced graphene oxide and rGO-Gd-DTPA sample. Raman spectra taken in the range from 500 - 3250 cm^{-1}.

Deconvolution method was used to evaluate quantitatively the area fit of the materials as intensity ratio of *D* and *G* bands cannot explain this effect. The rupture of

aromaticity by chemical reaction leads to the formation of smaller sp^2 domains that are confined by sp^3 bonds. Thus, it has dimension comparable to PAH's molecules. More extended covalent functionalization can also introduce polyene-like structures. Although, polycyclic aromatic hydrocarbons (PAH's) showed bands near 1250 and/or 1400 cm^{-1} in the Raman spectra, accompanied with variations in the position and relative intensity depending on the molecular size and symmetry, Including also one peak at around 1600 cm^{-1} [120, 125]. Therefore, this sample shows the changes of the position and intensity of the S and GI band compared with the reduced graphene oxide. In this case, it is remarkable that the S band position increases from 1139.6 cm^{-1} to 1203 cm^{-1} while GI bands moves from 1531.5 cm^{-1} to 1567 cm^{-1}. This designated the growths of fingerprints of polyacetylene structures resulting from ligand Gd-DTPA in the materials under study.

Consequently, the deconvolution pattern shows that the % area of *D* and *G* bands increases significantly from the sample reduced graphene oxide to rGO-Gd-DTPA. In the *D* band region, the value moved from 19.59 % to 59.67 % respectively. While in the *G* band increases from 1.02 % to 6.03 %, consequently. This changes in areas justified the surface modification of graphene single layered. This agrees with the result found by Jiali *et al.* [144] who investigated the reduction of GO using L-ascorbic acid for different reaction time.

In the reduced graphene oxide material, the smallest concentration of carboxyl group and hydroxyl persist in the sample, which attached with Gd-DTPA increases slightly the disorder in this samples. This can be justified by titration results, which proved that concentration of about 7.5 x 10^{-4} mmol COOH per mg of rGO. It becomes approximately ninety times lesser than graphene oxide. The inserts of Figure 5.10 nominates comparison of decovoluted Raman spectra of reduce graphene oxide (rGO) and rGO-Gd-DTPA samples. The Stokes phonon energy shift caused by laser excitation of about 514 nm wavenumber.

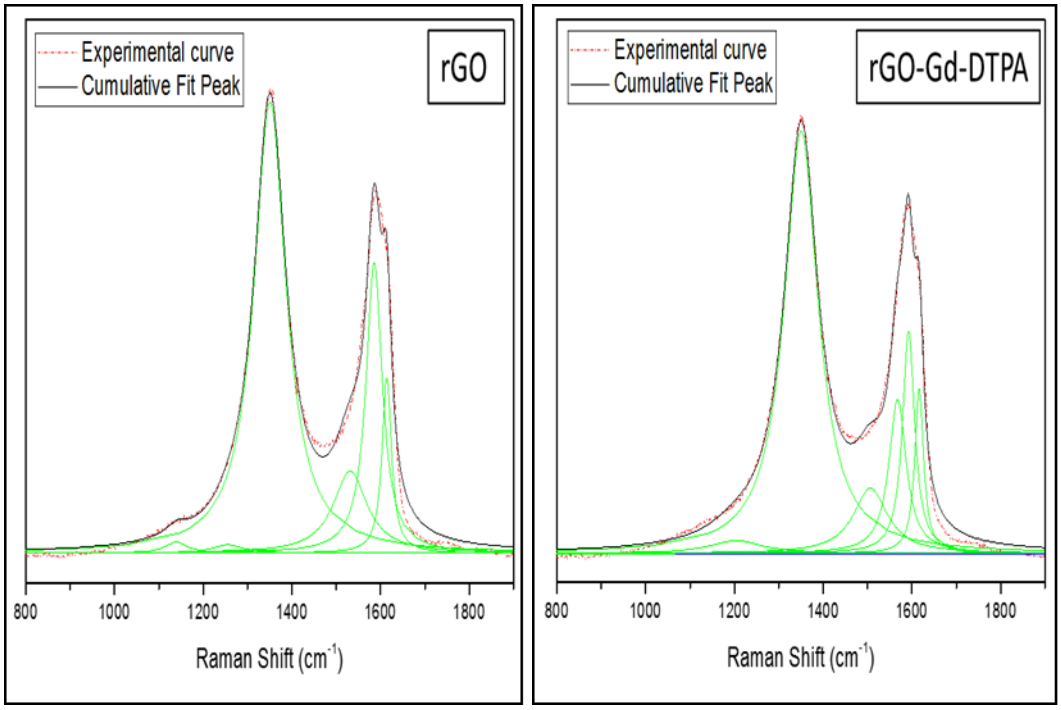

Figure 5. 10: Deconvolution of Raman spectra for a reduced graphene oxide in comparison with rGO-Gd-DTPA material using a 514 nm excitation laser. It was taken in the range from 800 cm^{-1} to 1900 cm^{-1}.

Compilation of the Raman spectrum obtained from the rGO-Gd-DTPA sample indicated the presence of the subpeaks in the range of 1200 cm^{-1} to 1550 cm^{-1}. Which can be resulting from disruption of the graphite lattice leading to small sp^2 region confined by sp^3 bonds. In addition, it can be assume like the satellite Gv band gives the confirmation of the ligand Gd-DTPA, even though this Gv band is usually reported of polyacetylene like structure in the sample [126].

5.5. Magnetic measurement of GO-Gd-DTPA and rGO-Gd-DTPA

The magnetic measurements have been made with the SQUID magnetometer (MPMS, Quantum Design) with a sensitivity of 1 x 10^{-8} emu. The magnetization per unit mass M (H, T) in emu/g have been measured for both the powder samples GO-DTPA and rGO-Gd-DTPA varying magnetic field (H) from -15,000 Oe to +15,000 Oe at the temperature 298 K.

Figure 5.11: magnetic susceptibility of Gd-DTPA magnetic molecular loaded onto the surface of graphene oxide (GO-Gd-DTPA) material. The result shows paramagnetic behavior on the sample. Resulting from the interaction between Gd and the spin of electron of the carbonyl and/or epoxy group of the sample. This magnetic behavior is surprise different from what has been reported before in the literature. In a graphene oxide, however pi-electron develop ferromagnetism due to the unique structure of the material. Therefore others reported superparamagnetic behavior when reduced the organic functionality in the material [141]. Further modification of the environment of the organic group by attached Gd-DPTA on the carbonyl group of the graphene oxide change magnetic behavior of the material.

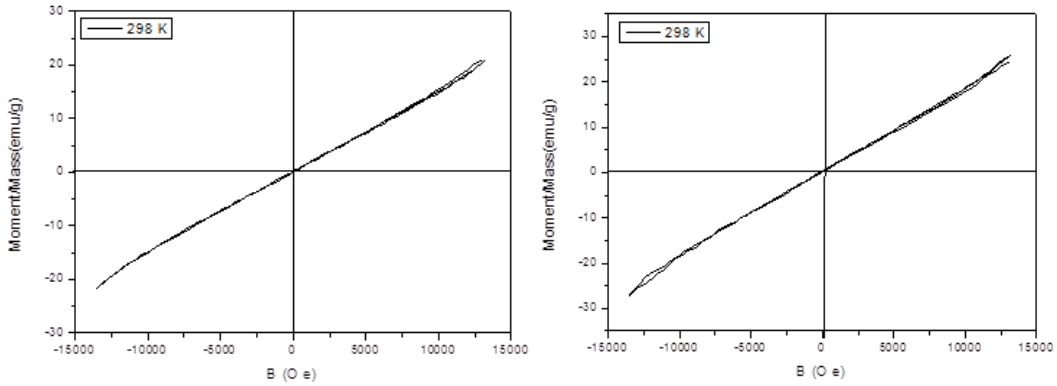

Figure 5. 11: The variation of magnetic moment as function of magnetic field taken in the range of -15000 to +15000. Magnetic behavior between forward and reverse sweep of GO-Gd-DTPA (left) and rGO-Gd-DTPA (right) samples taken at room temperature.

The graphitic material generally exhibit diamagnetic properties or paramagnetic as the slope is non negative. Therefore, many research group reported the

ferromagnetism in graphene oxide. Which comes from the graphitic regions circulated epoxy group and it has S-shaped M-H curve [145, 146]. Recently, it had been report that the frequency dependence behavior of the AC susceptibility of graphite oxide and extract spin glass behavior. The magnetic moment change with time at low temperature. Temperature field dependent will be require for further investigation about the magnetic properties. Figure 5.12 gives a comparative magnetic curve of GO-Gd-DTPA and rGO-Gd-DTPA samples at room temperature.

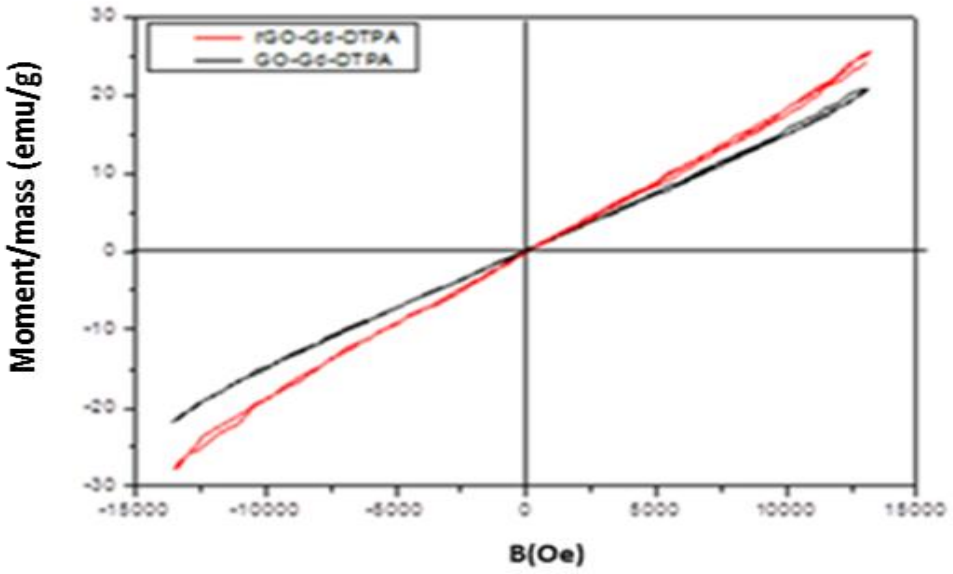

Figure 5. 12: Hysteretic behavior between forward and reverse sweep taken from GO-Gd-DTPA and rGO-Gd-DTPA at room temperature. The concentration of the carboxylic group increase the slope of the graph. Even though the sample present paramagnetic behavior at room temperature.

The coercive field H_C value is very small (<30 Oe) for both the samples at 300 K. It should be noted that the GO-Gd-DTPA (Mmax - 22 emu/g) sample shows comparatively lower value of magnetic moment than the rGO-Gd-DTPA (Mmax - 28 emu/g). It clearly indicates that the oxygen related functionalized groups namely, –O–H and COOH, are partly responsible for the magnetic characteristics of the oxides. Since the above functionalities are gradually removed during the reduction process for the preparation of rGO-Gd-DTPA, it reveals lower magnetic moment. Our FTIR and UV-visible study strongly supports the above observations.

Chapter 6

Conclusion and Recommendations

Carbon nanotubes are mainly used in different ways such as alloy with metal, major component for physical strength increase and, as devices layer installed in the accessory by the different manufactured semiconductor industries. The surface modification of carbon nanotubes extend their application in several sectors.

In this works, the functionalization of carbon nanotubes involving oxidative reflux was done in order to introduce chemical functionality along the surface and ends of carbon nanotubes. The method invariably results in an unpredictable degree of chemical functionalization of carbon nanotube surfaces, variable lattice order, and potentially introduces chemically different nanoscale environments.

This study was focused on a predictable approach towards the functionalization of multi-walled carbon nanotubes (MWCNTs); aimed at manipulating the degree and chemical nature of functionalization by controlling oxidative reaction temperatures, with a view to incorporate a magnetic complex Gd-DTPA on the nanotube surface via ternary complex formation.

Our findings indicate functionalization occurs at temperatures as low as 55 °C. However, the chemical nature of the attached functional groups varies with increasing temperature – understanding the latter is essential for the attachment of metal complexes Gd-DTPA to carbon nanotubes. Investigation of the functionalized MWCNTs were using spectroscopic techniques elucidates the prevailing chemical nature of the nanotube surface that suggests carboxylate functionality, is replaced at higher temperatures, by the formation of hydroxyl moieties. This observation is substantiated through deconvolution of *D* and *G* phonon modes of recorded Raman

spectra, corroborated by Zeta potential studies and analysis of acid-base titration data. The attachment of the Gadolinium complex of diethylenetriaminepentaaccetic acid, [$GdDTPAH_2$], to a functionalized-MWCNT is confirmed by chemical analysis using Inductively Coupled Plasma Atomic Emission Spectroscopy (ICP-OES), High-Resolution Transmission Electron Microscopy (HRTEM).

In this study, a comparative investigation into the hysteretic behavior was conducted. This was carried out at 300 K. As expected, there was a significant difference of the magnetic response for samples synthesized at different reaction temperatures. The results have shown an increase in the reaction temperature the large field response shows a wide variation in slope. This is explained when considering that the unfunctionalized nanotubes are intrinsically diamagnetic and predicted to have a large negative slope [140]. As the reaction temperature is increased this negative slope is steadily increased until a positive slope is observed for reaction temperature at 100 ^{o}C. The rise in temperature makes CNTs unstable and braking down the structure of the complex with increases reaction time. Which gives birth to few diamagnetic material in the sample. The FT-IR result has shown that the rise in the reaction time and temperature destroy progressively carboxylic group by showing a large band between 3200 – 3500 cm^{-1} which resulting of stretching vibration bond of hydroxyl group in the sample. This can be explained in terms of the increase in degree of functionalization across the samples as the temperature decrease with increase reaction time. As more functional groups are added to the nanotubes, the diamagnetic character which is a result of the conduction electrons is degraded. This is because the addition of functional groups disrupts the pi-conduction bands. This in turn means that, as expected, higher degree of functionalization or attachment of the Gd-DTPA ligand leads to a stronger spin interaction. This is due to a larger dispersion and reduction of the distance between spin centers.

These investigations were thus able to show that even thought at highest reaction temperature the more controlled functionalization and subsequent attachment of the Gd-DTPA ligands to the nanotubes can result in a variation of magnetic properties. We firstly see a strong deviation in these samples magnetic response as compared to

previous report which all indicated superparamagnetism. Our samples show hysteresis as well as indications of antiferromagnetic interaction and possibly an anisotropic exchange bias. This was only possible in systems which strong spin interactions. Further supported by random order Gd distribution of the complex in the material. This indicates that by controlling the Gd-DTPA distribution it is possible to tailor the magnetic character of the nanotubes, either increasing or decreasing the magnetic coupling between spins. This leads to complex magnetic mixed system that is valuable not only from a fundamental point for view but also for applications for spintronic devices.

In other hands, Carbonyl group have been introduced onto graphene single layer surface via Modified Hummers method. Sodium nitrate and potassium permanganate used as oxidant reactants. L-ascorbic acid used to produce reduced graphene oxide. Lower concentration of carboxylate group on reduced graphene oxide influenced the magnetic and electronic properties of the sample. Magnetic environment Gd-DTPA affected electronic transport properties of the reduced and graphene oxide. The presence of carbonyl groups has been characterized by Fourier transform Infrared (FT-IR) spectroscopy. Raman spectroscopy, High Resolution Transmission electron microscopy (TEM), Scanning electron spectroscopy (SEM) and Zeta potential were done for qualitative analysis purpose. Quantification of the functionalization group was determined by Boehm titration. The results indicated that paramagnetic behavior of ligand being unluckily not converted to superparamagnetic behaviors. It was shown the concentration of the organic functionality group (carbonyl) increases the slope of the curve which was higher concentration of Gd in the material. In addition, higher surface modification of graphene oxide and reduced graphene oxide using Gd-DTPA increases excitation of gadolinium electron in their last orbital. Those complexes can be used to increase or decrease the relaxation times of carbon-13 nuclei in NMR spectrometry.

The future work should be focused on the fluorescence as the materials had shown higher excitation in term of the energy band. The change in the oxidation process manipulating time as well as the reaction temperature in the range of five degree

from 55 – 100 °C could positively increases the concentration of the carboxylate group in the materials. The mole stoichiometry (CNT and ligand) and chemical environment of the carbon nanotubes played main role in term of the magnetic behaviors. The magnetic complex molecular Gd-DTPA could also be change to Gd-EDTA or magnetic polyaromatic molecule to investigate the magnetic behaviors of the pure graphene and/or carbon nanotubes. Raman temperature dependence could be the key of the future investigation of these materials. It can bring more information to support electronic transport and magnetic properties of the materials.

References

[1] J. Yamauchi., Fundamentals of Magnetism. In Nitroxides: Applications in Chemistry, Biomedicine and Materials Science., Wiley, 2008.

[2] T. Shinjo. Nanomagnetism and spintronics, *Elsevier, Second Edition,* 2014.

[3] A. Hoffmann and S. D. Bader, *Phys.Rev. Applied* 4, 047001, 2015.

[4] B. Park, Current and future of nanotechnology. issue in Environmental Science and Technology, vol. 24(1), pp. 1-18, 2007.

[5] T.L. Doane, and C. Burda, *Chemical Society Reviews,* vol. 41(7), pp. 2885-2911, 2012.

[6] S.M. Moghimi, A. C Hunter, and J.C. Murray, *Pharmacological reviews,* vol. 53(2), pp. 283-318, 2001.

[7] K. Maruyama, *Advanced Drug Delivery Reviews,* vol. 63(3), pp. 161-169, 2011.

[8] H. C. Huang, et al., *Journal of Controlled Release,* vol. 155(3), pp. 344-357, 2011.

[9] E. Goldberg, et al., *Journal of Pharmacy and Pharmacology,* vol. 54(2), pp. 159-180, 2002.

[10] K. Y. Choi, et al., *Nanoscale,* vol. 4(2), pp. 330-342, 2012.

[11] N. Erathodiyil and J.Y. Ying, *Accounts of Chemical Research,* vol. 44(10), pp. 925-935, 2011.

[12] L. Wang, et al., *International Journal of Nanomedicine,* vol. 6, pp. 2641-2652, 2011.

[13] S.M. Ametamey, M. Honer, and P. A. Schubiger, *Chemical Reviews*, vol. 2008. 108(5), pp. 1501-1516, 2008.

[14] S. Ncube., *Ph.D. Thesis*, Wits University, 2018

[15] Z. Yao, C. Dekker, P. Avouris,, *Topics in Applied Physics*, vol. 80, pp. 147-171, 2001.

[16] Saito R. and Kataura H., *Topics in Applied Physics*, vol. 80, pp. 213-247, 2001.

[17] J. Hone, *Topics in Applied Physics*, vol. 80, pp. 273-286, 2001.

[18] S.J. Tans, A.R.M. Verschueren, and C. Dekker, *Nature*, vol. 393, p. 49, 1998.

[19] X. Wang, et al., *Nano Letters*, vol. 9(9), pp. 3137-3141, 2009.

[20] M.F. Yu, et al., *Science*, vol. 287(5453), pp. 637-640, 2000.

[21] D. V. Kosynkin, A. L. Higginbotham, A. Sinitskii, J. R. Lomeda,A. Dimiev, B. K. Price, and J. M. Tour, *Nature*, vol. 458, pp. 872-876, 2009.

[22] Z. Yao, C.L. Kane, and C. Dekker, *Phys. Rev. Lett*, vol. 84, p. 2941, 2000.

[23] K. Liu, W. Wang, Z. Xu, X. Bai, E. Wang, Y. Yao, J. Zhang, Z. Liu, *Journal of American Chemical Society*, vol. 131, pp. 62-63, 2008.

[24] Y. Tison, C. E. Giusca, V. Stolojan, Y. Hayash, S. R. P. Silva, *Advanced Materials*, vol. 20, pp. 189-194, 2008.

[25] J. Kong, et al., *Science*, vol. 5453, pp. 622-625, 2000.

[26] J. Suehiro, G. Zhou, and M. Hara, *J. Phys. D: Appl. Phys*, vol. 36(21), pp. 109-114, 2003.

[27] C. Schonenber, A. Bachtold, C. Strunk, J. P. Salvetat, and L. Forro, *Appl. Phys,* vol. A 69, p. 283, 1999.

[28] J. D. Prades, et al., *Appl. Phys. Lett,* vol. 97, pp. 243105-243107, 2010.

[29] F. Hernández-Ramirez, et al., *Phys. Rev. B,* vol. 76, p. 085429, 2007.

[30] M. Donarelli, R. Milan, M. Ferroni, G. Faglia, E. Comoni, and G. Sberveglieri, in *AISEM, Annual conference,* 2015.

[31] Q. Kuang, C. Lao, Z.L. Wang, Z. Xie, and L. Zheng, *J. Am. Chem. Soc,* vol.129, pp. 6070-6071, 2007.

[32] S. Sarkar, A. Mondal, N. Giri and R. Ray, *Royal Society of Chem,* vol. 21, pp. 260-267, 2019.

[33] T. Ramanathan, A. A. Abdala, S. Stankovich, D. A. Dikin,M. Herrera-Alonso, R. D. Piner, D. H. Adamson, H. C.Schniepp, X. Chen, R. S. Ruoff, S. T. Nguyen, I. A. Aksay,R. K. Prud'Homme and L. C. Brinson, *Nat. Nano technol.,* vol. 3, pp. 327-331, 2008.

[34] X. Wang, S. Tabakman and H. Dai, *J. Am. Chem. Soc.,* vol. 130, pp. 8152–8153, 2008.

[35] R. Skomoski, *Europhys. Lett,* vol. 48, pp. 455–460, 1999.

[36] K. Jasuja, J. Linn, S. Melton and V. Berry, *J. Phys. Chem. Lett,* vol. 1, p. 1853, 2010.

[37] L. V. Radushkevich and V. M. Lukyanovich, *Zurn Fisic Chim,* vol. 26, pp. 88-95, 1952.

[38] A. Oberlin, M. Endo, and T. Koyama, *J. Cryst. Growth,* vol. 32, pp. 335-349, 1976.

[39] K. S. Novoselov, *Rev. Mod. Phys,* vol. 83, p. 837, 2011.

[40] S. Ncube., *Msc Dissert.,* Wits University, 2014.

[41] M. S. Dresselhaus, G. Dresselhaus, and P. Avouris, *Springer-Verglag,* p. 80, 2001.

[42] L. Jiao, L. Zhang, X. Wang, G. Diankov, and H. Dai, *Nature,* vol. 458, pp. 877-880, 2009.

[43] X. Zhou, *PhD thesis*, Cornell University, 2008.

[44] T. W. Ebbesen, H. J. Lezec, H. Hiura, J. W. Bennett, H. F. Ghaemi, T. Thio, *Nature,* vol. 382, pp. 54-56, 1996.

[45] B. Q. Wei, R. Vajtai, and P. M. Ajayan, *Appl. Phys. Lett,* vol. 79, p. 1172, 2001.

[46] S. Salahuddin, M. Lundstrom, and S. Datta, *IEEE Trans, Electron Devices,* p. 52, 1734.

[47] Y. Ma, P. O. Lehtinen, A.S. Foster and R. M. Niemine, *New J. Phys*, vol. 6, p. 68, 2004.

[48] S. Iijima and T. Ichihashi, *Nature,* vol. 363(6430), pp. 603-605, 1993.

[49] D. S. Bethune, et al, *Nature,* vols. 363(6430), pp. 605-607, 1993.

[50] R. Smalley, T. Guo, P. Nikolaev, A. Thess, and D. Colbert, *Chem. Phys. Lett,* vol. 243, p. 49, 1995.

[51] A. Thess, et al., *Science,* vol. 273(5274), pp. 483-487, 1996.

[52] F. Obelenis and A. Champi, *Brazilian Journal of phys,* vol. 44, no. 6, pp. 682-686, 2014.

[53] S. Iijima, *Nature,* vol. 354(6348), pp. 56-58, 1991.

[54] J. Kong, et al., *Nature,* vol. 395(6705), pp. 878-881, 1998.

[55] H. Wu, X. Chang, L. Liu, F. Zhaoa, Y. Zhao, *Journal of Materials Chemistry*, vol. 20, p. 1036-1052, 2010.

[56] A. Servant, et al., *Elservier, carbon*, vol. 97, pp. 126-133, 2016.

[57] J. Pedr´ os, A. Bosc´a, J. Mart´ınez, S. Ruiz-G´ omez, L. P´erez, V. Barranco and F. Calle, *J. Power Sources*, vol. 317, pp. 35-42, 2016.

[58] M. S. Dresselhaus, A. Jorio and R. Saito, *Annual Rev. Condens. Matter Phys*, vol. 1, pp. 89-108, 2010.

[59] K. S. Novoselov, A. K. Geim, S. V. Morozov, D. Jiang, Y. Zhang, S. V. Dubonos, I. V. Grigorieva and A. A. Firsov, *Science*, vol. 306, pp. 666-669, 2004.

[60] J. Wintterlin and M. L. Bocquet, *Surf. Sci.*, vol. 603, pp. 1841-1852, 2009.

[61] C. Berger, Z. Song, X. Li, X. Wu, N. Brown, C. Naud, D. Mayou, T. Li, J. Hass, A. N. Marchenkov, E. H. Conrad, P. N. First and W. A. de Heer, *Science*, vol. 312, pp. 1191-1196, 2006.

[62] T. A. Land, T. Michely, R. J. Behm, J. C. Hemminger and G. Comsa, *Surf. Sci*, vol. 264, pp. 261-270, 1992.

[63] K. S. Kim, Y. Zhao, H. Jang, S. Y. Lee, J. M. Kim, K. S. Kim, J. H. Ahn, P. Kim, J. Y. Choi and B. H. Hong, *Nature*, vol. 457, pp. 706-710, 2009.

[64] M. Eizenberg and J. M. Blakely, *Surf. Sci*, vol. 82, pp. 228-236, 1979.

[65] W. Choi and J. Lee, *Taylor & Francis Group, Boca Raton*, 2012.

[66] H Yu, B. Zhang, B. Bulin, R. Li, R. Xing, *Sci. Report*, vol. 6, p. 36143, 2016.

[67] H. Lodish, *Macmillan, London,* vol. 6, pp. 978-0-7167-7601-7, 2008.

[68] M.S. Usman, M.Z. Hussein, S. Fakurazi and F.A. Saad, *Che. Central Journal,* vol. 11, p. 47, 2017.

[69] S.A. Wolf, A. Y. Chtchelkanova, and D.M. Treger, *IBM J. Res. & Dev.,* vol. 50, pp. 101-110, 2006.

[70] http://nobelprize.org/nobel_prizes/physics/laureates/2007/info.html

[71] Tsymbal, E.Y. and D. Pettifor, *Solid State Physics,* vol. 56, pp. 113 – 237, 2001.

[72] M. Julliere, *Phys. Lett,* vol. 54A, pp. 225-226, 1975.

[73] S. Maekawa and U. Gäfvert, *IEEE Trans. Magn,* vol. 18, p. 707, 1982.

[74] J. G. Simmons, *J. Apl Phys,* vol. 34, p. 1793, 1963.

[75] E.Y. Tsymbal and I. Zutic, "Handbook of spin transport and magnetism," *Chapman Hall/CRC,* 2011.

[76] D. Wang, C. Nordman, J.M. Daughton, Z. Qian and J. Fink, *IEEE Trans. Magn,* vol. 40, p. 2269, 2004.

[77] S. Parkin, X. Jiang, C. Kaiser, A. Panchula, K. Roche, and M. Samant, *Proc. Of the IEEE,* vol. 91, p. 661 , 2003.

[78] L. Berger, *Phys. Rev. B,* vol. 54, p. 9353, 1996.

[79] M. Tsoi, et al, *Phys. Rev. Lett,* vol. 80, p. 2181, 1998.

[80] Z. Wwnkai, Z. Dongqing, Y. Chuan-Lu and S. Zhaopeng, *J. Mat. Chem. C,* vol. 5, p. 8862, 2017.

[81] P. Damle, T. Rakshit, M. Paulsson and S. Datta, *IEEE Trans Nano Technol.,* vol. 1, pp. 145-153, 2002.

[82] P. Qi, A. Javey, M. Rolandi, Q. Wang, E. Yenilmez and H. Dai, *J. am. Chem. Soc.*, vol. 126, pp. 11774-11775, 2004.

[83] C. Sudipto and J. Pal Amlan, *J. App. Phys. Letter,* vol. 104, p. 013305, 2014.

[84] V. Igor, et al., *J. ACS Nano,* vol. 11, pp. 6868-6880, 2017.

[85] M. Urdampilleta, S. Klayatskaya, M. Ruben and W. Wernsdorfer, *J. ACS Nano,* vol. 9(4), pp. 4458-4464, 2015.

[86] M. Urdampilleta, J-P. Cleuziou, S. Klyatskaya, M. Ruben, and W. Wernsdorfer, *J. Nature Mat*, vol. 10, pp. 502-506, 2011.

[87] M. Ganzhorn, S. Klyatskaya, M. Ruben, and W. Wernsdorfer, *J. Nano tech*, vol. 8, pp. 165-169, 2013.

[88] A. Palyi, P. R. Struck, M. Rudner, K. Flensberg, and G. Burkard, *J. Phys. Rev. Letter*, vol. 108, p. 206811, 2012.

[89] B. Lassagne, D. Ugnati and M. Respaud, *J. Phys. Rev. Lett,* vol. 107, p. 130801, 2011.

[90] McCreary, K. M., Swartz, A. G., Han, W., Fabian, J. & Kawakami, R. K, *Phys.Rev. Lett*, vol. 109, p. 186604, 2012.

[91] C. Józsa et al, *Phys. Rev.*, vol. B 80, p. 241403(R), 2009.

[92] W. Han, et al., *Nano Lett.*, vol. 12, pp. 3443-3447, 2012.

[93] A. Candini, S. Klyatskaya, M. Ruben, and W. Wernsdorfer, and M. Affronte, *J. Nano Lett*, vol. 11, pp. 2634-2639, 2011.

[94] W. Shi, Z. Wang, Q. Zhang, Y. Zheng, C. Leong, et al., *Sc. Report*, 2012.

[95] R. Martel, T. Schmidt, H. R. Shea, T. Hertel and Ph. Avouris, *Applied Phys*, vol. 73, p. 17, 1998.

[96] G. H. Florian, J. Nastalczyk, Z. Roslaniec, K. Schulte, *Chemical physics letters*, vol. 370, pp. 820-824, 2003.

[97] C.A. Cooper, S.R. Cohen, A.H. Barber, H.D. Wagner, *Appl. Phys. Lett*, vol. 81, p. 3873, 2002.

[98] M. Bottini, S. Bruckner, K. Nika, N. Bottini, S. Bellucci, A. Magrini, A. Bergamaschi, and T. Mustelin, *Toxicology letters* , vol. 160, pp. 121-126, 2006.

[99] Yi Zhang, Yuhong Bai, and Bring Yan, *Drug discovery today*, vol. 15, pp. 11-12, 2010.

[100] J. Chen, B. Yao, C. Li and G. Shi, *Elservier*, vol. 64, pp. 225-229, 2013.

[101] Z. Zhang, H. Yang, G. Shen, P. Cheng, Z. Jingyan, and S. Guo, *Chem. Com*, vol. 46, pp. 1112-1114, 2009.

[102] M.J. Fernández-Merino, L. Guardia, J.L. Paredes, S. Villar-Rolis, P. Solis- Fernández, A. Martinez-Alonso, and J.M.D. Tascón, *Phys. Chem.*, vol. 114, pp. 6426-6432, 2010.

[103] M. A. Kabir, T. Nandy, M.A. Haque, A. Dutta, Z.H Mahmoud, *Intern. J. of Advance in mat. Sc. and Engineering*, vol. 3, pp. 3-4, 2014.

[104] C.J. Barnett, C.E. Gowenlock, K. Welsby, A.O. White and A.R. Barron, *Nano letters*, vol. 18, pp. 695-700, 2018.

[105] F. Seichepine, S. Salomon, M. Collet, S. Guillon, L. Nicu, G. Larrieu, E. Flahaut, and C. Vieu, *Nanotechnology,* vol. 23, p. 1, 2012.

[106] S. Raychaudhuri, S.A. Dayeh, D. Wang and E.T. Yu, *Nano letters*, vol. 9, pp. 2260-2266, 2009.

[107] M. Duchamp, K. Lee, B. Dwir, J. W. Seo, E. Kapon, L. Forro and A. Magrez, *ACS Nano*, vol. 4, p. 279, 2010.

[108] P. Li, C.M. Martin, K.K. Yeung and W. Xue, *Biosensors*, vol. 1, pp. 23-35, 2011.

[109] "https://nanoheat.stanford.edu/tools/electrothermal-nanobridges-nanowires," Retrieved, 10 July 2018.

[110] A. Han, D. Vlassarev, J. Wang, J.A. Golovchenko, and D. Branton, *Nano letter*, vol. 10(12), pp. 5056-5059, 2010.

[111] A. Furst, R. C. Berlo and S. Hooton, *Chem. Rev*, vol. 65, pp. 51–68, 1965.

[112] Y. Si and E. T. Samulski, *Nano Lett.*, vol. 8, pp. 1679–1682, 2008.

[113] G. Wang, J. Yang, J. Park, X. Gou, B. Wang, H. Liu and J. Yao, *J. Phys. Chem. C.*, vol. 112, pp. 8192-8195, 2008.

[114] P. Karrer, *Chem. Rev*, vol. 14, pp. 17–30, 1934.

[115] M. B. Davies, J. Austin and D. A. Partridge, *J. Royal Soc. of Chem*, vol. UK, 1991.

[116] M. Ambrosi, E. Fratini, V. Alfredsson, B. W. Ninham, R. Giorgi, P. L. Nostro and P. Baglioni, *J. Am. Chem. Soc.*, Vols. 128, pp. 7209-7214, 2006.

[117] Y. Wang, P. H. C. Camargo, S. E. Skrabalak, H. Gu and Y. Xia, *Langmuir,* vol. 24, pp. 12042-12046, 2008.

[118] D. Bikiaris, A. Vassiliou, K. Chrissafis, K.M. Paraskevopoulos, A. Jannakoudakis, A. Docoslis, *Elsevier Polym. deg. and Stabil.,* vol. 93, pp. 952-967, 2008.

[119] Tuinstra and J. L. Koenig, *J. Phys. Chem.,* vol. 53, p. 1126, 1970.

[120] C. Castiglioni, C. Mapelli, F. Negri and G. Zerbi, *J. Chem. Phys*, vol. 114, pp. 963–974, 2001.

[121] A. C. Ferrari, *Solid State Commun*, vol. 143, pp. 47–57, 2007.

[122] Susana L.H, Robelo, Alexandra guedes, Monika E., Szefczyk, André M., Pereira, Joâo P., Araûjo, and Cristina Freire, *J. Royal Chem.,* vol. 18, p. 12784, 2016.

[123] Sadezky, H. Muckenhuber, H. Grothe, R. Niessner and U. Po¨schl, *Carbon,* vol. 43, pp. 1731–1742, 2005.

[124] Z. Syrgiannis, A. Bonasera, E. Tenori, V. La Parola, C. Hadad, M. Gruttadauria, F. Giacalone and M. Prato, *Nanoscale,* vol. 7, pp. 6007–6013, 2015.

[125] K. Li, J. I. Hayashi and C. Z. Li, *Fuel,* vol. 85, pp. 1700-1707, 2006.

[126] H. Shirakava, T. Ito and S. Ikeda, *J. Polym.,* vol. 4, pp. 460-462, 1973.

[127] A. C. Ferrari and J. Robertson, *Phys. Rev. B: Condens. Matter Mater. Phys.*, vol. 61, pp. 14095–14107, 2000.

[128] D. Hines, M. H. Rummeli, D. Adebimpe and D. L. Akins, *Chem. Commun,* vol. 50, pp. 11568–11571, 2014.

[129] W. Zhou, S. Sasaki and A. Kawasaki, *Carbon,* vol. 78, pp. 121–129, 2014.

[130] T. P. Chua, M. Mariatti, A. Azizan and A. A. Rashid, *J. Alloys Comp.,* vol. 480, pp. 534–536, 2009.

[131] T. Peci, T.J.S. Dennis, and M. Baxendale, *Carbon,* vol. 87, pp. 226-232, 2015.

[132] Sarkar, S. and Haddon, R.C, *Condensed Matter, Mat. Sc,* arXiv preprint arXiv:1409.5194. pp. 1-32, 2014.

[133] P. Grodzinski, M. Silver, and L. K. Molnar, *Expert review of molecular diagnostics,* vol. 6(3), pp. 307-318, 2006.

[134] B. Sitharaman, and L. J. Wilson, *J. Biomedical Nanotechnology*, vol. 3(4), pp. 342-352, 2007.

[135] Yan, C., Chen, C., Hou, L., Zhang, H., Che, Y., Qi, Y., Zhang, X., Cheng, J. and Zhang, Z., *Journal of drug targeting*, vol. 25(2), pp. 163-171, 2017.

[136] E. Duman, M. Acet, I. Dincer, A. Elmali, and Y. Elerman, *J. magnetism and magnetic materials,* vol. 309(1), pp. 40-53, 2007.

[137] J. Nogués, and I. K. Schuller, *J. Exchange bias Magnetism and Magnetic Materials*, vol. 192(2), pp. 203-232, 1999.

[138] J. Klinovaja, and D. Loss, *Physical Review B,* vol. 87(4), p. 045422, 2013.

[139] L. Corbellini, J. Plathier, C. Lacroix, C. Harnagea, D. Ménard, and A. Pignolet, *J. Applied Physics*, vol. 120(12), p. 124101, 2016.

[140] A. S. Kotosonov, and S. V. Kuvshinnikov, *Physics Letters A,* Vols. 230(5-6), pp. 377-380, 1997.

[141] S.K. Sarkar, K.K. Raul, S.S. Pradhan, S. Basu, A. Nayak, *Elsevier*, vol. (64), pp. 78-82, 2014.

[142] S. Stankovich, D. A. Dikin, R. D. Piner, K. A. Kohlhaas, A. Kleinhammes, Y. Jia, Y. Wu, S. T. Nguyen and R. S. Ruoff, *Carbon*, vol. 45, pp. 1558–1565, 2007.

[143] L. Gauraw, et al, *BioMacromolec*, vol. 14, p. 3, 2013.

[144] Jiali Z, Haijun Y, Guangxia S, Ping C. Jingyan Z. and Shouwu G, *Chem. Commun*, vol. 46, pp. 1112-1114, 2010.

[145] D. Lee, J. Seo, X. Zhu, J. M. Cole, & H. Su, *Appl. Phys. Lett.*, vol. 106, p. 172402, 2015.

[146] T. Tang, et al., *Appl. Phys. Lett. ,* vol. 104, p. 123104(41), 2014.

Appendix

Comparison of transmittance FT-IR Spectra of Potassium bromide, Gadolinium oxide, DTPA, and Gd-DTPA materials. The characteristic peak can be observe in the FT-IR spectra.

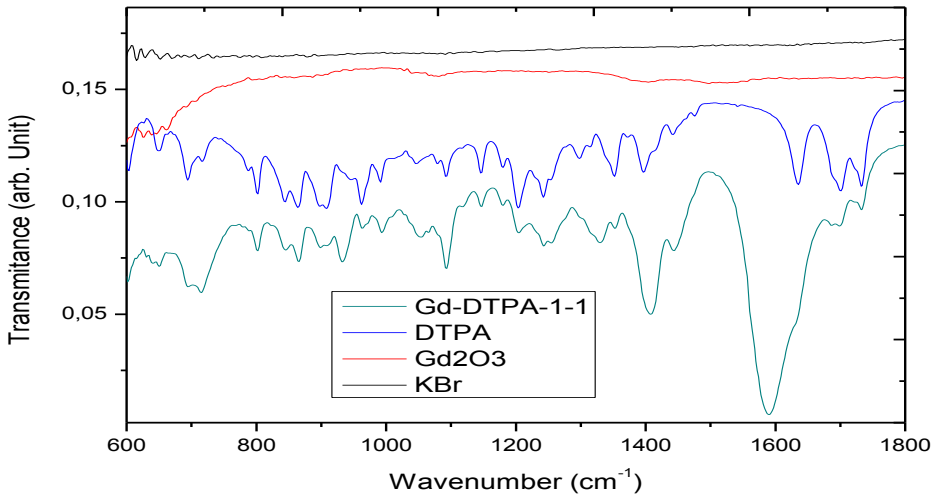

FT-IR spectrum of the functionalized multi-walled carbon nanotubes after 24 hours of refluxing reaction time at the temperature of 100 degree celcius. A large hydroxyl (OH) band being formed between the values of 3100 - 3600 cm^{-1} wavenumber.

Transmittance FT-IR from f-MWCNT 100 °C (24hrs) liquid

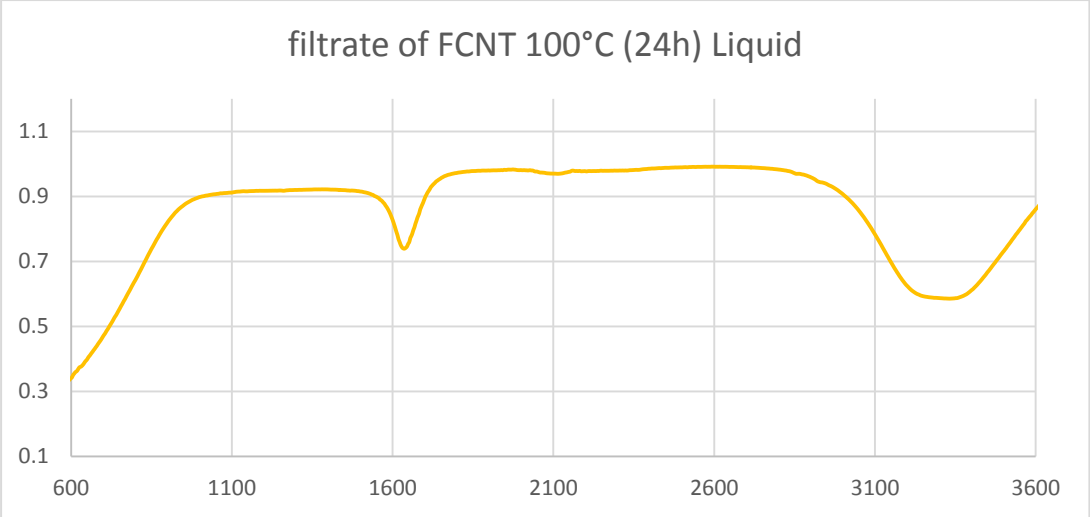

Calculation of Functionalized MWCNTs 55 °C

Mm of Gd DTPA = 583.60 mg/mmol

Mm of COOH = 45 mg/mmol

Concentration in Mass = 0.21252 mg COOH per mg of FMWCNTs

Now take,

100 mg of FMWCNTs x 0.21252 mg COOH per mg of FMWCNTs = **21.252** mg COOH

Number of mols = **21.252 mg COOH / 45 mg per mmol COOH**

= 0.47227 mmols of COOH

As the ratio is 1:1

Mass of Gd DTPA = **0.47227 mmol *x*** 583.60 mg/mmol

= **275.6177 mg**

Therefore;

100 mg of functionalized multi walled carbon nanotubes will be reacting with 275.6177 mg of Gd-DTPA.

Concerns Reaction with access of Gd-DPTA

Mass ratio: 1:1.2

Mass of Gd DTPA = **0.47227 mmol *x*** 583.60 mg/mmol x 1.2

= **330.74 mg**

Therefore;

100 mg of functionalized multi walled carbon nanotubes will be reacting with **330.74 mg** of Gd-DTPA.

Synthesis of complex molecular gadolinium chelate in Functionalized CNTs

Mixed multi-walled carbon nanotubes with Gd-DTPA chelates added a volume of DI water. Sonicated at 30 °C for a short period to allow good dispersion of CNTs. Stirred the suspension at the temperature at 30 °C for 24 hours. Residue wash with de-ionized water to remove impurities. This washing process will be done using filtration vacuum pump. Dry the residue under vacuum in Nitrogen gas environment. Similar method will be applied to react pristine CNTs sample with Gd-DTPA chelates. It can also be applied to link graphene oxide to gadolinium chelates.

Weighted 100 mg of CNTs and 275.62 mg of Gd-DTPA mixed with 50 ml (20ml) of DI water. Sonicated at 30 °C for 5 min. Suspension stirred at the temperature of 30 °C for 24 hours in a closed system. Filtrate or evaporate the solvent. Washed the residue with a volume of 200 ml deionized water.

Graphene oxide loaded Gd-DTPA.

Overall image and EDX for reaction 1. From EDX results. It is noticeable that Carbon, oxygen and Gadolinium are dominated elements in the overall sample.

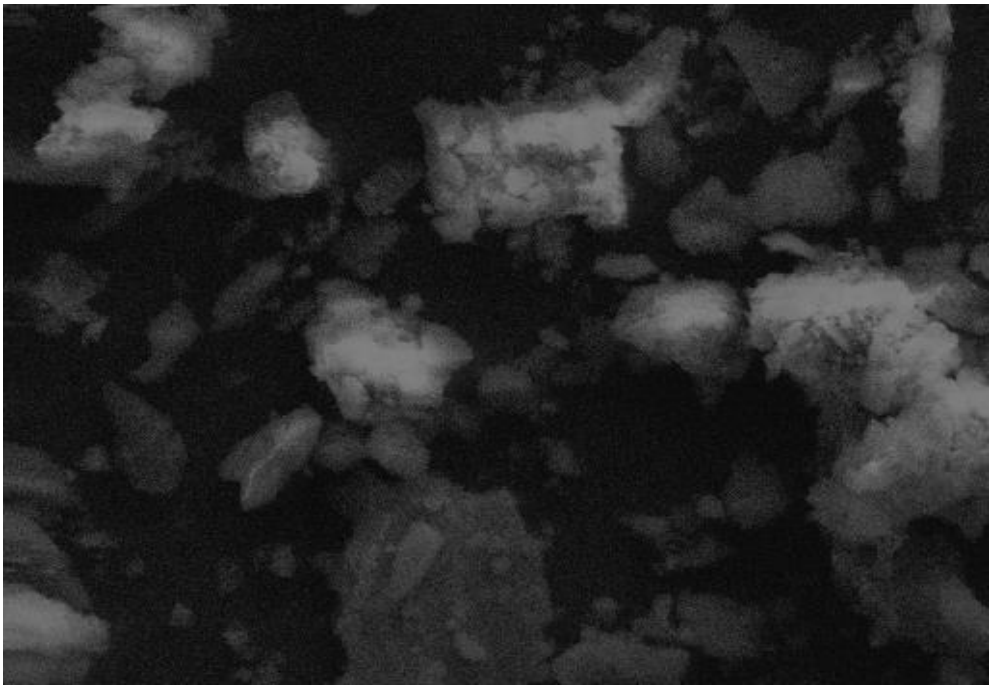

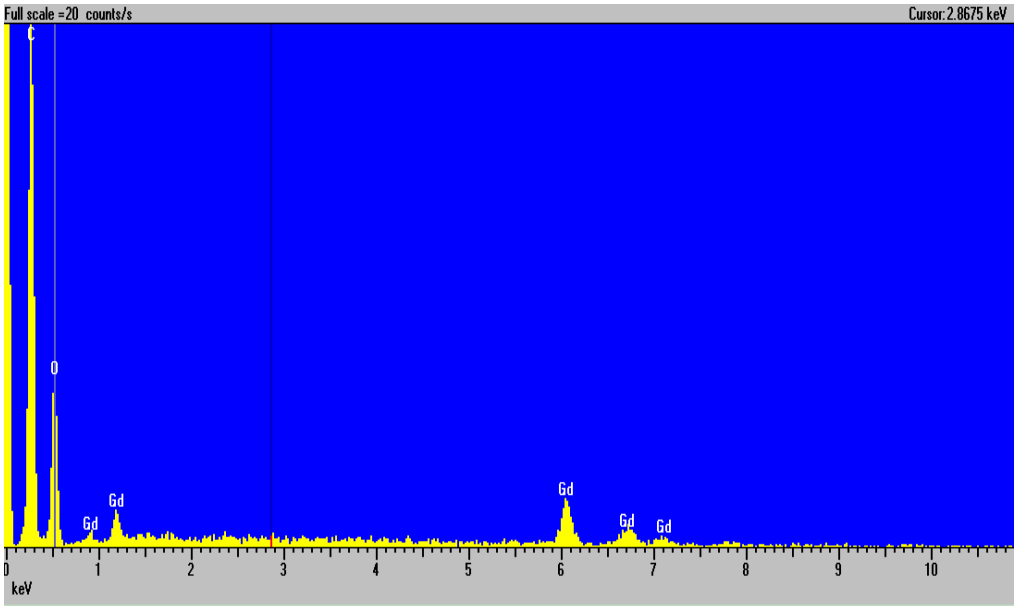

EDX Taken on the grey area.

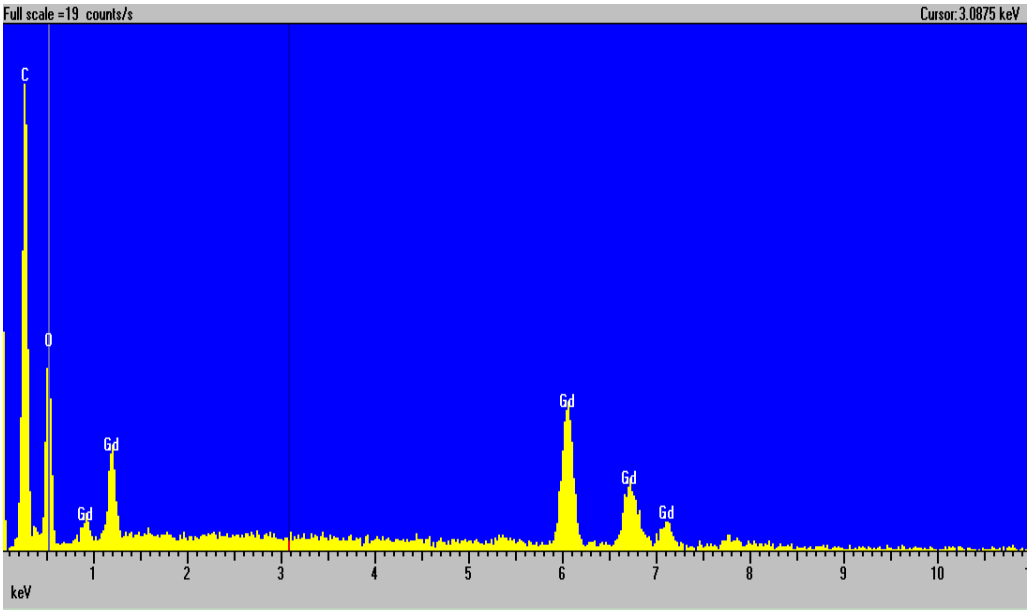

EDX Taken on the White area.

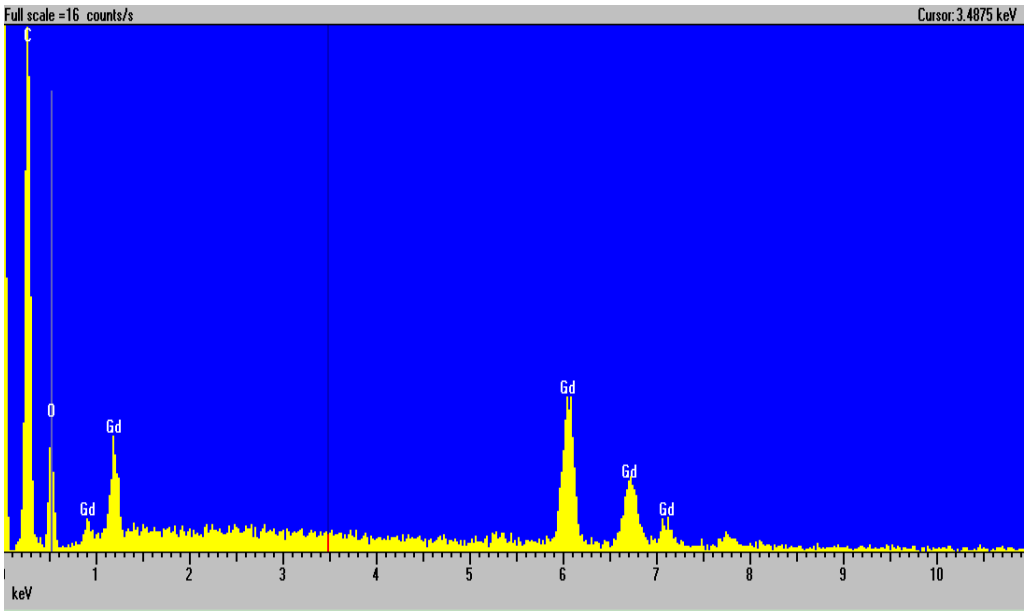

Zeta potential RESULTS

Few amount of sample was dispersed in 3 ml of distilled water. Shake and place into cell for measurement. The Zeta potential and conductivity recorded of carbon nanotubes and graphene oxide (GO) are summarized below:

Sample Name:	1 (pristine) average		
SOP Name:	mansettings.nano		
File Name:	pristine.dts	**Dispersant Name:**	Water
Record Number:	13	**Dispersant RI:**	1.330
Date and Time:	11 February 2019 11:45:34 AM	**Viscosity (cP):**	0.8872
		Dispersant Dielectric Constant:	78.5

Temperature (°C):	25.0	**Zeta Runs:**	18
Count Rate (kcps):	3.5	**Measurement Position (mm):**	2.00
Cell Description:	Clear disposable zeta cell	**Attenuator:**	11

		Mean (mV)	**Area (%)**	**St Dev (mV)**
Zeta Potential (mV):	-13.8	**Peak 1:** -13.7	100.0	5.50
Zeta Deviation (mV):	4.96	**Peak 2:** 0.00	0.0	0.00
Conductivity (mS/cm):	0.00910	**Peak 3:** 0.00	0.0	0.00

Result quality : Good

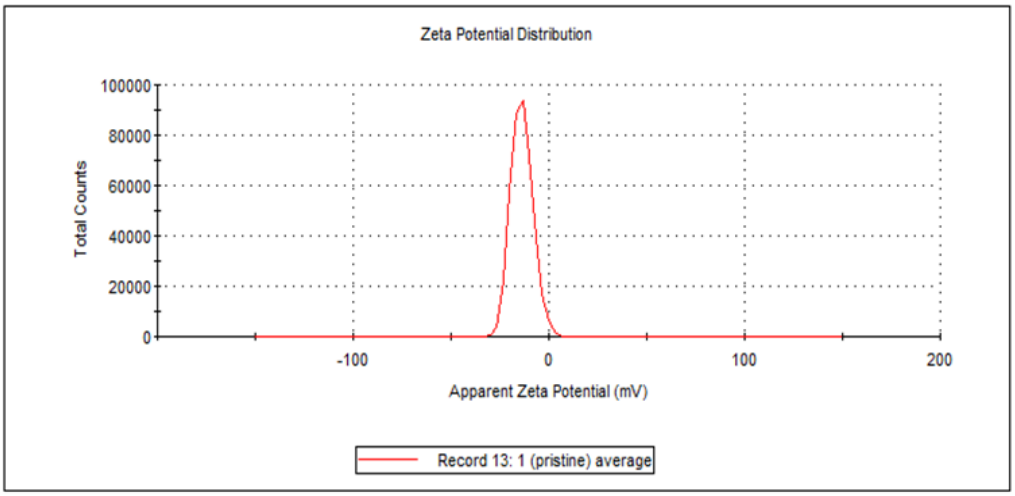

Sample Name:	FCNT 55C Average		
SOP Name:	mansettings.nano		
File Name:	pristine.dts	**Dispersant Name:**	Water
Record Number:	21	**Dispersant RI:**	1.330
Date and Time:	11 February 2019 12:20:40 PM	**Viscosity (cP):**	0.8872
		Dispersant Dielectric Constant:	78.5

Temperature (°C):	25.0	**Zeta Runs:**	12
Count Rate (kcps):	119.2	**Measurement Position (mm):**	2.00
Cell Description:	Clear disposable zeta cell	**Attenuator:**	11

			Mean (mV)	Area (%)	St Dev (mV)
Zeta Potential (mV):	-44.8	**Peak 1:**	-44.7	100.0	4.44
Zeta Deviation (mV):	4.29	**Peak 2:**	0.00	0.0	0.00
Conductivity (mS/cm):	0.0221	**Peak 3:**	0.00	0.0	0.00

Result quality : Good

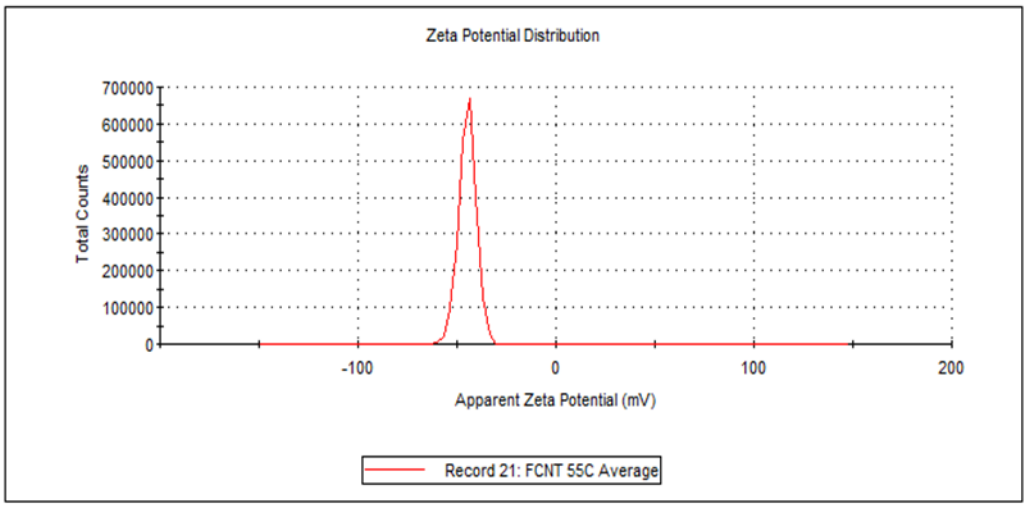

Sample Name:	FCNT 60C average		
SOP Name:	mansettings.nano		
File Name:	pristine.dts	**Dispersant Name:**	Water
Record Number:	25	**Dispersant RI:**	1.330
Date and Time:	11 February 2019 12:37:20 PM	**Viscosity (cP):**	0.8872
		Dispersant Dielectric Constant:	78.5

Temperature (°C):	25.0	**Zeta Runs:**	12
Count Rate (kcps):	92.0	**Measurement Position (mm):**	2.00
Cell Description:	Clear disposable zeta cell	**Attenuator:**	11

			Mean (mV)	**Area (%)**	**St Dev (mV)**
Zeta Potential (mV):	-31.8	**Peak 1:**	-31.8	100.0	5.35
Zeta Deviation (mV):	4.95	**Peak 2:**	0.00	0.0	0.00
Conductivity (mS/cm):	0.0118	**Peak 3:**	0.00	0.0	0.00

Result quality : Good

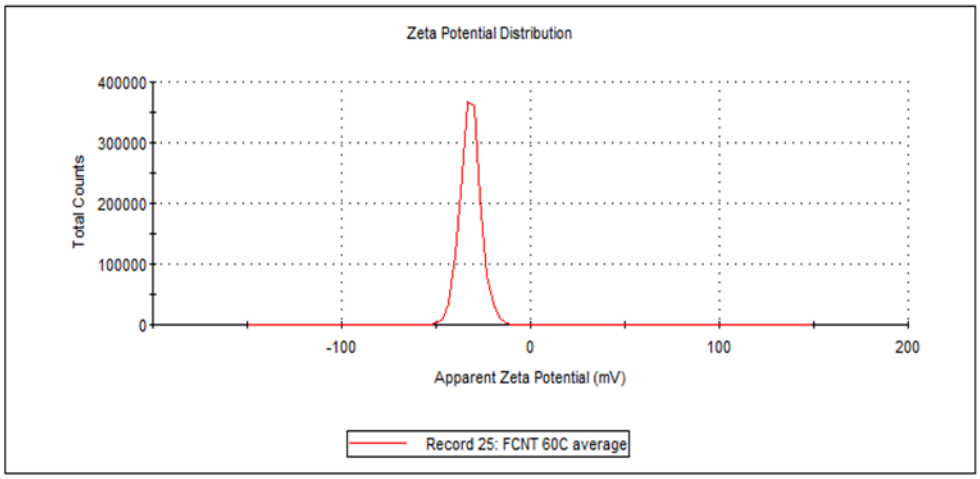

Sample Name:	FCNT 70C Average		
SOP Name:	mansettings.nano		
File Name:	pristine.dts	**Dispersant Name:**	Water
Record Number:	29	**Dispersant RI:**	1.330
Date and Time:	11 February 2019 12:54:49 PM	**Viscosity (cP):**	0.8872
		Dispersant Dielectric Constant:	78.5

Temperature (°C):	25.0	**Zeta Runs:**	15
Count Rate (kcps):	5.8	**Measurement Position (mm):**	2.00
Cell Description:	Clear disposable zeta cell	**Attenuator:**	7

			Mean (mV)	**Area (%)**	**St Dev (mV)**
Zeta Potential (mV):	-29.6	**Peak 1:**	-29.7	100.0	4.71
Zeta Deviation (mV):	4.42	**Peak 2:**	0.00	0.0	0.00
Conductivity (mS/cm):	0.00912	**Peak 3:**	0.00	0.0	0.00

Result quality : Good

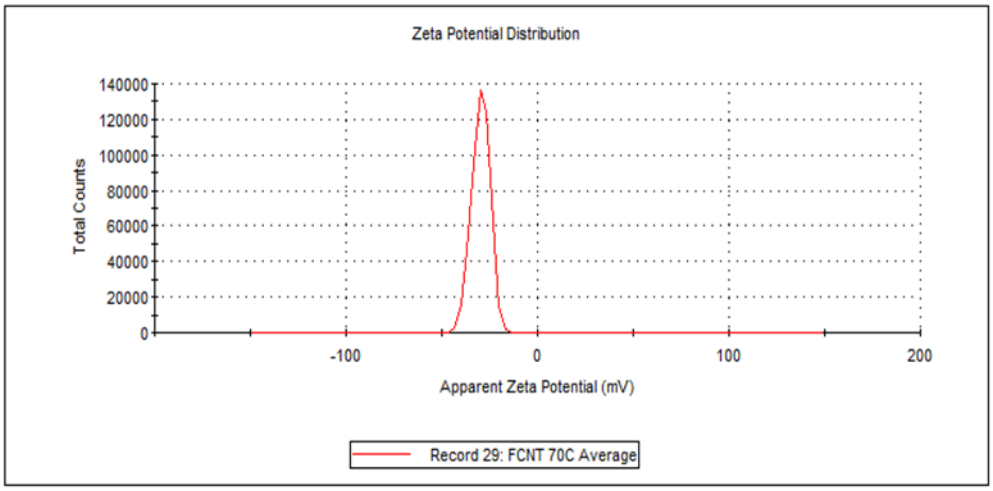

Sample Name:	FCNT 100C Average		
SOP Name:	mansettings.nano		
File Name:	pristine.dts	**Dispersant Name:**	Water
Record Number:	33	**Dispersant RI:**	1.330
Date and Time:	11 February 2019 01:08:01 PM	**Viscosity (cP):**	0.8872
		Dispersant Dielectric Constant:	78.5

Temperature (°C):	25.0	**Zeta Runs:**	12
Count Rate (kcps):	231.8	**Measurement Position (mm):**	2.00
Cell Description:	Clear disposable zeta cell	**Attenuator:**	9

			Mean (mV)	**Area (%)**	**St Dev (mV)**
Zeta Potential (mV):	-38.9	**Peak 1:**	-39.0	100.0	4.80
Zeta Deviation (mV):	4.62	**Peak 2:**	0.00	0.0	0.00
Conductivity (mS/cm):	0.0148	**Peak 3:**	0.00	0.0	0.00

Result quality : Good

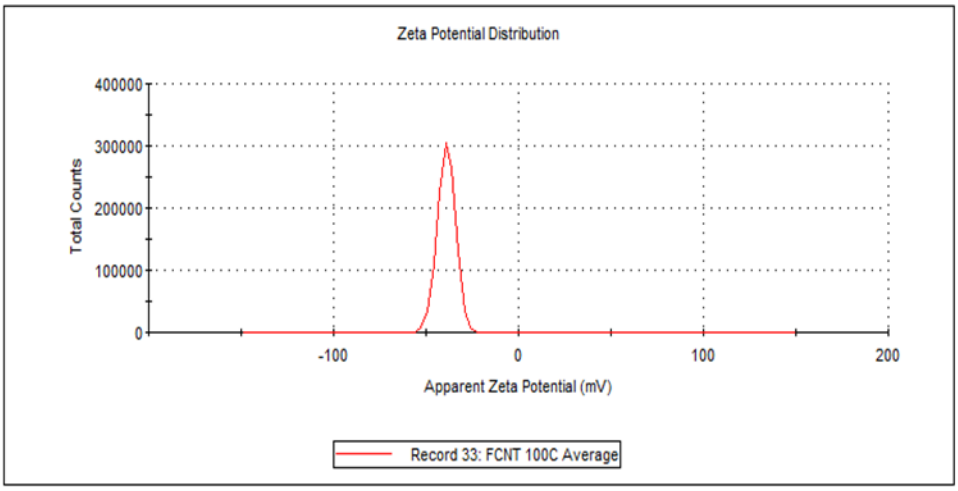

Sample Name:	GO in water Average		
SOP Name:	mansettings.nano		
File Name:	pristine.dts	**Dispersant Name:**	Water
Record Number:	37	**Dispersant RI:**	1.330
Date and Time:	11 February 2019 01:19:23 PM	**Viscosity (cP):**	0.8872
		Dispersant Dielectric Constant:	78.5

Temperature (°C):	25.0	**Zeta Runs:**	12
Count Rate (kcps):	190.9	**Measurement Position (mm):**	2.00
Cell Description:	Clear disposable zeta cell	**Attenuator:**	6

			Mean (mV)	**Area (%)**	**St Dev (mV)**
Zeta Potential (mV):	-42.8	**Peak 1:**	-42.7	100.0	6.68
Zeta Deviation (mV):	6.50	**Peak 2:**	0.00	0.0	0.00
Conductivity (mS/cm):	0.0214	**Peak 3:**	0.00	0.0	0.00

Result quality : Good

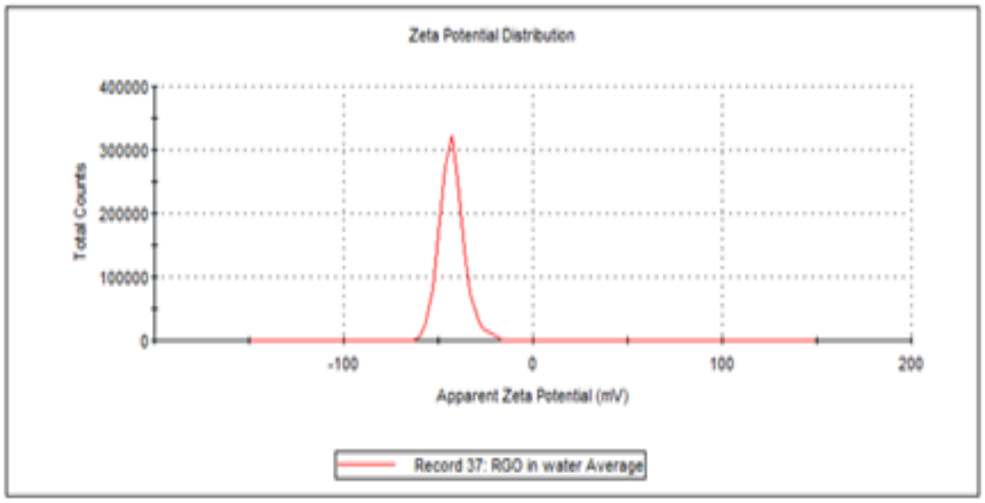

Publications

1. I.S. Mosse, A. de Sousa, S. Ncube, C. Coleman, S. Bhattacharyya, S. Gratowski and V. Koledov. Bottom-up Nano-integration Route for modified Carbon nanotube Spintronic Device Fabrication. *J. Phys: Conf. Series* 1461 012015, 2020.
   https://ieeexplore.ieee.org/abstract/document/8552242

2. C. Coleman, S. Ncube, I.S. Mosse, A. Irzhak, V. Koledov, S. Gratowski, A. de Sousa, S. Bhattacharyya. Bottom-up Nanointegration Technique for Novel Functionalized Carbon Nanotube and Multi-layer Graphene Device Fabrication. *IEEE, (3M-NANO)*, 2018.
   https://scholar.google.com/scholar?hl=en&as_sdt=0%2C5&q=DOI%3A+10.1088%2F1742-6596%2F1461%2F1%2F012015&btnG=